



OPEN

An innovative cellular medicine approach via the utilization of novel nanotechnology-based biomechatronic platforms as a label-free biomarker for early melanoma diagnosis

Jassim A. Alqabandi^{1,2,3✉}, Rhiannon David⁴, Ussama M. Abdel-Motal⁵, Rawan O. ElAbd^{6✉} & Kamal Youcef-Toumi¹

Innovative cellular medicine (ICM) is an exponentially emerging field with a promising approach to combating complex and ubiquitous life-threatening diseases such as multiple sclerosis (MS), arthritis, Parkinson's disease, Alzheimer's, heart disease, and cancer. Together with the advancement of nanotechnology and bio-mechatronics, ICM revolutionizes cellular therapy in understanding the essence and nature of the disease initiated at a single-cell level. This paper focuses on the intricate nature of cancer that requires multi-disciplinary efforts to characterize it well in order to achieve the objectives of modern world contemporary medicine in the early detection of the disease at a cellular level and potentially arrest its proliferation mechanism. This justifies the multidisciplinary research backgrounds of the authors of this paper in advancing cellular medicine by bridging the gap between experimental biology and the engineering field. Thus, in pursuing this approach, two novel miniaturized and highly versatile biomechatronic platforms with dedicated operating software and microelectronics are designed, modeled, nanofabricated, and tested in numerous *in vitro* experiments to investigate a hypothesis and arrive at a proven theorem in carcinogenesis by interrelating cellular contractile force, membrane potential, and cellular morphology for early detection and characterization of melanoma cancer cells. The novelties that flourished within this work are manifested in sixfold: (1) developing a mathematical model that utilizes a Heaviside step function, as well as a pin-force model to compute the contractile force of a living cell, (2) deriving an expression of cell-membrane potential based on Laplace and Fourier Transform and their Inverse Transform functions by encountering Warburg diffusion impedance factor, (3) nano-fabricating novel biomechatronic platforms with associated microelectronics and customized software that extract cellular physics and mechanics, (4) developing a label-free biomarker, (5) arrive at a proved theorem in developing a mathematical expression in relating cancer cell mechanobiology to its biophysics in connection to the stage of the disease, and (6) to the first time in literature, and to the best of the authors' knowledge, discriminating different stages and morphology of cancer cell melanoma based on their cell-membrane potentials, and associated contractile forces that could introduce a new venue of cellular therapeutic modalities, preclinical early cancer diagnosis, and a novel approach in immunotherapy drug development. The proposed innovative technology-based versatile bio-mechatronic platforms shall be extended for future studies, investigating the role of electrochemical signaling of the nervous system in cancer formation that will significantly impact modern oncology by pursuing a targeted immunotherapy approach. This work also provides a robust platform for immunotherapy practitioners in extending the study of cellular biophysics in stalling neural-cancer interactions, of which the FDA-approved chimeric antigen receptor (CAR)-T cell therapies can be enhanced (genetically engineered) in a lab by improving its receptors to capture cancer antigens. This work amplifies the importance of studying neurotransmitters and electrochemical signaling molecules in shaping the immune T-cell function and its effectiveness in arresting cancer proliferation rate (mechanobiology mechanism).

¹Mechatronics Research Laboratory, Massachusetts Institute of Technology (MIT), Cambridge, MA, USA.
²Mechatronics in Medicine Laboratory, Imperial College London, London, UK. ³Department of Manufacturing Engineering Technology (Bio-Mechatronics) Department, PAAET, Kuwait, State of Kuwait. ⁴Division of Computational and Systems Medicine (CSM), Department of Surgery and Cancer, Faculty of Medicine, Imperial College London, Sir Alexander Fleming Building, London, UK. ⁵Department of Cancer Immunology and AIDS, Dana-Farber Cancer Institute, Harvard Medical School, Boston, MA, USA. ⁶McGill University Health Center, Montreal, QC, Canada. ✉ email: jassim@mit.edu;

In combating cancer, early detection is central to the prevention of cancer metastasis, not only giving patients a better prognosis but also allowing more cost-effective and minimally invasive treatments to be applied. This has initiated the need for the cellular medicine field, where its applications to the early detection and treatment of cancer play a dominant role in characterizing the mechanobiology and electrophysiology of cancer cells.

Early recognition of cancer at a cellular level could potentially impact combating the disease since it could prevent cancer metastasis^{1–5}. Unfortunately, conventional methods used in cancer diagnosis are costly, hospital-based, and suffer from significant limitations depending on the type of cancer being targeted. Imaging-based approaches such as positron emission tomography (PET), computed tomography (CT), magnetic resonance imaging (MRI), X-rays, bone scintigraphy, and ultrasound scans generally suffer from low to moderate sensitivity in the detection of certain kinds of cancers, which means early diagnosis is often not possible^{6–17}. For example, PET scans are not satisfactorily reliable for the early detection of gastric carcinoma⁶, hepatocellular carcinoma (HCC)⁷, or endometrial cancer (lymph node metastasis)⁸. Similarly, CT scans are not sufficiently sensitive to identify lymph-node-invasive metastases⁹, nor does MRI detect lymph-node staging¹⁰. Furthermore, X-ray scans fail to detect breast cancer¹¹ reliably; similarly, bone scans are not adequate to detect the formation of micrometastatic prostate cancer cells within bone marrow¹²; moreover, ultrasounds have poor sensitivity as well as specificity for prostate cancer detection¹³.

An alternative to non-invasive imaging-based methods involves the cytological analysis of biopsied tissue samples. However, these are invasive, time-consuming, and suffer from poor sensitivity for low-grade/stage tumors, which would require second-stage clinical analyses¹⁸. From an implementation perspective, some of these approaches can only be applied to some patients. For example, using techniques involving high radiation levels, such as bone scans¹⁴, can be controversial in children¹⁵. MRI is arguably not to be utilized unless it's optimally performed for cancer patients who have implanted defibrillators¹⁶ and those with ear implants (cochlear)¹⁷, upon which these implanted devices contribute to artifact (distortion) on the developed image of a suspicious lesion and shouldn't be performed.

Cancer biology overview

Prior to invoking the design synthesis, analysis, microfabrication, and testing of the proposed miniaturized-versatile bio-mechatronic platforms in examining the hypothesis proposed in this paper, it is essentially vital to first understand the formation of cancer, which is summarized in multiple stages. First, cancer is initiated in a single cell by a disruption of gene expression due to a number of factors associated with the environment and eating habits¹⁹; cancer is attributable to damage or loss of critical gene targets. This is followed by a rearrangement or amplification of genes¹⁹, where gene mutation or dysregulation leads to the transformation of a proto-oncogene (normal gene) into an oncogene (mutated gene), which promotes the malignant phenotype. The damage or loss of tumor suppressor genes (TSGs) or anti-oncogenes, which are genes encoding proteins required for regulating normal cell growth and differentiation, contributes to preserving the status of tumorigenesis. At the same time, it prevents a cancerous cell from invoking the apoptosis process (programmed cell death)^{19–21}. The damage of TSG is generally in both alleles, where one exception is p53, a protein responsible for the apoptosis process of cells, in which single allele damage is sufficient^{19,21}; p53 performance would be drastically abridged in cancer cells^{19,21}. The deletion or inactivation of TSp53 promotes the neoplastic phenotype and dysregulation of apoptosis, which eventually contributes to cancer development. Cancer then invokes the cell proliferation mechanism (mitosis)^{19–21}.

It is worth stating that healthy cells can differ from cancerous cells in terms of the number of chromosomes. The former exhibits 46 chromosomes (diploid cells), while the latter exhibits irregular structure and an irregular number of chromosomes (aneuploid): a state where a cell either exhibits an excess or loss of the normal number of chromosomes²². Also, cancer cells experience a reduction in the number of gap junctions responsible for cell-cell communication among nearby cells²³.

From the mechanical aspect of cells, a living cell exhibits a mass on the order of 3–4 ng²⁴, with a volume on the order of 1 pL²⁵. The cell's typical diameter is in the range of 8–30 μm, such as that illustrated in Fig. 1^{2,26–28}—for the general reader to appreciate the size of a living cell and for better visualization, consider the diameter of a human hair as a scaling factor tool, which is on the order of 80 μm²⁹. As illustrated in Alqabandi et al.², the microscopic image of the B16-F10 cell (Fig. 1) is obtained via an atomic force microscope (AFM) (National Instrument, Austin, TX, USA), with a V-shaped probe tip radius (Hydra Probes, nanoscience Instruments, Phoenix, AZ, USA). The applied bending force of the cantilever tip within a liquid medium under a semi-contact mode is captured by a quadrant photodiode of the AFM recording module. Thus, the B16-F10 cell diameter was found to be 8.496 μm (Fig. 1a and b). The measurements were obtained over a 40 Hz–3 MHz frequency over 250 recording points. Recordings were taken under clean room conditions at a room temperature of 27 °C. However, Nakamura et al.²⁷ demonstrated that the size of the B16-F10 is 15.4 ± 1.4 μm, using an inverted microscope (IX-71, Olympus, Tokyo, Japan) and a high-speed camera (FASTCAM Mini AX200, Photron, Tokyo, Japan). Throughout a time series of 20 μs between two consecutive microscopic snapshots of a cell leaving the microfluidic channel, the cellular diameter ranged from 12 to 14.2 μm. Their obtained size of the B16-F10 is

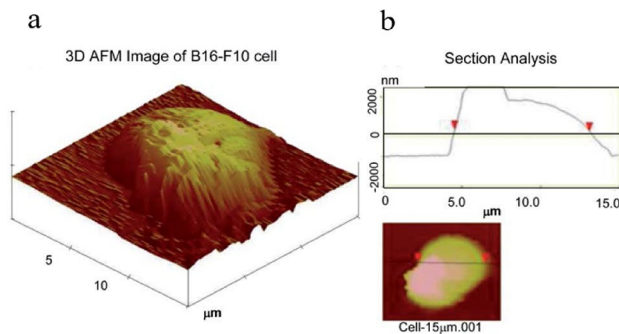


Fig. 1. Atomic force microscopy Image of B16-F10 melanoma model. **(a)** 3-D image of a B16-F10 mouse melanoma cancer cell. **(b)** Cross-sectional analysis of the B16-F10 cell obtained by AFM.

debatable, as is whether the measurements faithfully depicted the actual size of the cell considering the image distortion of the microscopic light beam penetrated through the microfluidic channels made from PDMS polymer molded to a glass substrate accommodating the living cell. Thus, discrepancies in measured cellular diameter in the literature vary and are attributable to several factors, e.g., the type of growth surface, the viability of the measured cell, and the techniques exerted in the measuring mechanism. In all cases, comprehending the range of cellular mechanophenotyping and physical characteristics of the cells shall serve as guidance for a microfabricator to set the design parameters and investigate microfabrication acceptable tolerances that would allow accommodation of the living cell, avoid system clogging, and enable reusability via constant washing of the integrated microfluidic system that shall be introduced in Section “*In vitro experiments*” of this paper.

A distinction between malignant and benign cancer has been described in^[19,30]. The former goes solely into the mitosis stage, attacking neighboring cells and tissues through blood vessels and incurring lymph nodes (invasive). In contrast, the latter doesn't leave the site of its formation. It is of great interest in this study to analyze the metastasis aspect of cancer cells (cell motility) in which the cells proliferate and migrate into other distanced tissues and organs through lymphatic vessels (lymphatic), blood vessels (hematogenous), and serosal surfaces (transcoelomic)^[31]. The proliferation of carcinomas (epithelial malignancy) initiates through the lymphatic path, then through blood vessels, whereas bone and soft tissue tumors (sarcomas) preferably proliferate initially through blood vessels^[31].

The cancer proliferation mechanism heavily depends on the participation of blood vessels that provide oxygen, nutrients, and the removal of wastes and carbon dioxide^[32]. This stimulates metastasis, enabling malignant cells to invade other tissues and organs via the blood circulatory system. Cells, in general, are allocated in a very salty, rich medium of nutrients with other molecules, vitamins, and growth factors, e.g., platelet-derived growth factor (PDGF)^[33], MAP kinase coupled growth factors^[25], or epidermal growth factor (EGF)^[34]. For example, Deoxyribonucleic (DNA) synthesis (replication) is a sign of cell growth^[35]. Remarkably, some cancer cells have the mechanism to produce their growth factor, and some undergo rapid division without the presence of growth factor due to a malfunction of their receptors^[35]. For cancer cells to proliferate, some must adhere to a surface-performing extracellular matrix (ECM) protein mesh communication with neighboring cells (anchorage-dependent). In contrast, others must be free from adhesion (anchorage-independent)^[36].

On a genetic level, the deactivated performance of TSGs, normal genes, or the presence/activation of oncogenes (abnormal genes) leads to cancer formation^[37,38]. A specific protein can act as a biomarker (a biological marker) for the presence of cancer; however, due to the complexity of cancer oncogenes’ formation and heterogeneity, detection is quite difficult using a sole biomarker with sufficient sensitivity and specificity^[38]. The uncontrolled proliferation process is attributable to irregular cell signaling, triggering the growth factor protein of other cells to initiate the rapid-division process, attacking neighboring cell tissues, and invading other organs^[2,19,39]. Thus, cell electrochemical signaling is a label-free biomarker that can differentiate oncogenesis.

Cancer electrophysiology

The electrochemical characteristics of a living cell are a manifestation of cell mitosis status, DNA synthesis, and cell mutation cycle^[19,39]. Even proteins and their building components (amino acids) possess distinctive electrophysiology characteristics^[40]. Remarkably, an enormous electric field is created within the vicinity of a living cell^[41,42]. Marino et al.^[43] have obtained the electrochemical potential of a breast cancer cell collected from 110 female patients of different ages, races, and of different infected breast sides (right or left). Their analyses have considered 81 benign cases, among which fibrosis and fibroadenoma are analyzed, and 29 malignant, of which ductal carcinoma is investigated^[43]. They have exploited two cases in terms of cell potential: Contralateral and Ipsilateral. The former is defined in medical terms as the reoccurrence of cancer in “the opposite breast side,” whereas the latter is defined as the redevelopment of cancer “on the same breast side”^[44]. Their findings on the magnitude of electrochemical potentials of cancer and benign for the contralateral case are, respectively, 16.8 ± 15.3 mV and 18.5 ± 11.1 mV (Mean \pm SD), where SD is the standard deviation^[43]. On the other hand, the magnitude of electrochemical potentials of cancer and benign for Ipsilateral cases are 17.4 ± 12.8 mV and 16.9 ± 8.9 mV, respectively^[43]. In their study, they have reached no conclusion in relating the age of the patient to

the associated electrical potential; furthermore, they have noticed an alteration in K^+ cation concentration that manifests the activity of K^+ ion channel within the infected area⁴³.

In a publication by Cone and Tongier⁴⁵, it has been found that for Chinese hamster cells, the normal cells experience a membrane potential of -70 mV. In comparison, cancerous cells exhibit a potential of -10 mV, where DNA synthesis is imposed. This is attributable to the permeability (fusion pore size) of a living cell and its hyperpolarization and depolarization activities, which shall be extensively discussed in the analytical, empirical, and discussion of the results of the in vitro experiments carried out in Sects. “Development of the mathematical model of cellular electrophysiology”, “Empirical solution of the mathematical model of cellular electrophysiology”, and “Results and discussion of the electrophysiology in vitro experiments”, respectively. Accordingly, Schaefer et al.⁴⁶ have measured the membrane potential of a rat Shay chloroleukemic tumor cell (leukemic cell), which was found to be -9.02 ± 0.4 mV (inside relative to the outside ground potential), by using a microelectrode of $10\text{--}30$ M Ω tip resistance, and tip potential of -1 to -3 mV. Furthermore, they have measured the ion concentration of cells for K^+ ion, Na^+ ion, Cl^- ion, and water, which were 122 ± 9 mEq/l of cell water, 48 ± 4 mEq/l, 72 ± 7 mEq/l, and $77.5\% \pm 0.5\%$ of cell wet weight, respectively. On the other hand, the external potassium concentration was increased from 7 to 120 mEq/l, where diffusion of the external Na^+ ion into the cell via ion channels didn't significantly change the internal concentration of K^+ .

Marino et al.⁴⁷ have investigated the relationship between cell-membrane potentials of breast tissue together with breast epithelial cells and oncogenesis (progression toward malignancy and tumor formation) from one side, as well as the electrical potentials of the surface of the breast from another perspective. They have recognized that the presence of distinctive electrochemical potential of a cell is mainly attributable to diffusion (nutrient ionic concentration moving from high concentration to low); hence, the depolarization feature of cancer cells, as opposed to healthy ones, is mainly due to a reduction or a loss of intracellular potassium concentration (K^+) to the extracellular region⁴⁷; on a lesser account, it is also attributable to a built-up concentration of sodium (Na^+) within the intracellular regime⁴⁷. They conducted their experiments on a criterion base of having a minimum of 20 cells for each studied case, where female human subjects of different ages and races and laboratory animals were investigated. In general, it is found that cancer cell membrane potential is less in magnitude than that of a healthy cell⁴⁷. For instance, for 28 samples of MCF 10A cell (healthy epithelial cell line), the cell-membrane potential is -58.1 ± 5.8 mV; for 45 samples of MDA 435 L2 (Human breast carcinoma), the cell-membrane potential is -51.8 ± 8 mV; and for 33 samples of MCF7 (human breast adenocarcinoma cell line), the cell-membrane potential is -42.1 ± 5.3 mV⁴⁷. Furthermore, they have concluded that cell-membrane potential is an indication of cell-mutation progression (stage of the cell), and it's irrelevant to the patient's age⁴⁷.

On a liver-tissue scale, Sun et al.⁴⁸ have investigated the cell-membrane potential of four human malignant hepatocyte cell lines (Chang, HepG2, HuH-7, and PLC/PRF/5) and further studied the GAB A_A receptor mRNA expression within the same cell lines; interestingly, they have analyzed the consequences of restoring the cell-membrane potential of such malignant cell lines to the vicinity of the resting potential of non-malignant hepatocytes. Their potential measurements were carried out by optical fluorescent voltage-sensitive dye and GAB A_A receptor expressions were monitored by RT-PCR screening, and western blot analyses were performed. Their study has proven that malignant cell lines, as opposed to non-malignant ones, are substantially depolarized, elevating the trans-membrane potential, and GABAergic activity arrests malignant hepatocyte growth. They have concluded their analyses by showing that the studied four malignant hepatocyte cell lines are clearly depolarized (Chang: -7.5 ± 1.0 mV, Hep G₂: -9.8 ± 0.5 mV, HuH-7: -42 ± 0.3 mV, and PLC/PRF/5: -3.2 ± 0.4 mV), as opposed to the resting and proliferating cell-membrane potentials of non-malignant hepatocytes, which were found respectively to be -25.1 ± 1.5 mV, and -20.1 ± 1.6 mV⁴⁸.

Pancrazio et al.⁴⁹ have allocated the presence of voltage-gated currents in the ionic channels of K^+ , Na^+ , and Ca^{+2} in 3 lung-cancer-cell lines using a patch-clamp technique: NCI-H128, NCI-H69, and NCI-H146. The current-peak amplitude of Na^+ , K^+ , and Ca^{+2} are found to be 46 ± 14 pA for 5 cultured cells, 58 ± 6 pA for 11 cultured cells, and 93 ± 16 pA for 26 cultured cells, respectively. In their analyses, the voltage clamp approach is described as fixing (clamping) the membrane potential at a fixed value, where a pipette and electrodes are used, which leads to the elimination of the capacitive current of the cell membrane and thus the total membrane current equals the ionic current^{49,50}.

Nordenstrom⁵¹ and Pekar⁵² have extensively worked on electrophysiology treatment by invasively inserting two platinum needles (two electrodes) into a tumor by DC means: anode into a cancer cell and cathode within a medium. The injection of direct current into cancer cells has shown a reduction in DNA production, activation of the immune system, generation of electrolysis (breakage of chemical bonds via current), electrophoresis (movement of particles within a medium due to the electric field), electroosmosis (movement of polar fluid within cell membrane), and electroporation (increase in conductivity and dielectric property of cell membrane due to applied electric field)⁵³⁻⁵⁵.

Hope and Iles⁵⁶ have highlighted the importance of impedance measurements and reviewed major electrophysiological characteristics of breast cancer using an impedance analyzer. They have indicated that measurements taken at frequencies less than 1 kHz depict the ionic extracellular properties, where frequencies ranging from 30 kHz to 30 MHz are sufficient to characterize cellular biophysics. They have drawn a distinction between the impedance of dead and living tissues on the basis that impedance is a dependent variable on the time at which the permeability of cell membrane changes after a number of hours of cell death. Thus, to extract reliable information about the biological system within an in vitro experiment, measurements should be taken during the cell viability period and constant cell growth commencement, illustrated in the division and cytoplasmic formation within the exponential phase of a cell growth versus time (Phase II) of the S-shaped curve (Fig. 2).

Han et al.⁵⁷ have also categorized different stages of breast cancer cell lines through impedance analyses: MCF-10A (healthy cell), MCF7 (early-stage cancer), MDA-MB-231 (invasive-cell line), and MDA-MB-435 (late metastasized). They took the impedance measurements of these cells over a frequency range of 100 Hz– 3 MHz.

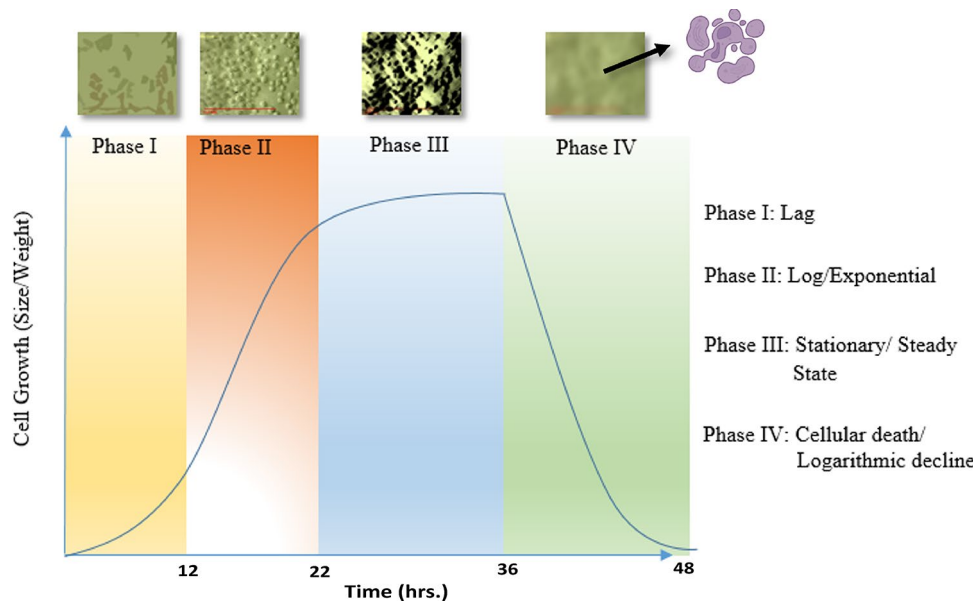


Fig. 2. The S-shaped curve (Phase I–III) and logarithmic decline curve (Phase IV) illustrate the different phases of cell growth versus time. A microscopic image of an A-375 melanoma cell is taken during the exponentially growing logarithmic Phase II (cells are adherent). Per the microscopic observations, Phase III, attributable to lack of nutrients, depicts the commencement of the death process of cells, indicating the stoppage of their metabolic functions, where cells start to detach from the surface. Other images are just illustrative (non-real) of the different statuses of cell growth: initial cell growth (Phase I) and cellular death due to diminishing of cell viability requirements (Phase IV), where cellular death illustration is created with BioRender.com.

They have shown that cell membrane-specific capacitance for MCF-10A is $1.94 \pm 0.14 \mu\text{F}/\text{cm}^2$, MCF-7 is $1.86 \pm 0.11 \mu\text{F}/\text{cm}^2$, MDA-MB-231 is $1.63 \pm 0.17 \mu\text{F}/\text{cm}^2$, and MDA-MB-435 is $1.57 \pm 0.12 \mu\text{F}/\text{cm}^2$. Similarly, the resistance values for the preceding cell lines are $24.8 \pm 1.05 \text{ M}\Omega$, $24.8 \pm 0.93 \text{ M}\Omega$, $24.9 \pm 1.12 \text{ M}\Omega$, and $26.2 \pm 1.07 \text{ M}\Omega$, respectively.

Yun et al.⁵⁸ have taken electrochemical impedance measurements of human prostate cancer cells (LNCaP) via the utilization of a nanotube within a microfluidic channel. The unique aspect of their experiment is measuring the electrochemical impedance in various buffer media at different incubation times: milli-Q water, di-ionized (DI) water, and electrical contacting electrodes. They have shown that phase angle increases with the increase of incubation time. It has been illustrated that a specific cell-membrane capacitance is equivalent to $20 \text{ pF}/\text{cm}^2$ ⁵⁹.

Suwowiec et al.⁶⁰ have indicated that the permittivity and conductivity of different stages of breast cancer cells within in vitro environments are discriminated against frequency measurements between 20 KHz and 100 MHz⁵¹. On the other hand, Morimoto et al.⁶¹ have arrived at a conclusion on the variation of impedance characteristics between healthy and breast cancer cells within an in vivo environment in a frequency range between 0 and 200 KHz as opposed to an ex vivo regime. In addition, Chauveau et al.⁶² have measured impedance in a frequency range of 10 KHz to 10 MHz; accordingly, their results also show a distinction between normal and cancerous cells.

Alqabandi et al.² have designed and microfabricated a device that measures the specific capacitance and resistance of a B16-F10 mouse melanoma in conjunction with a high-impedance analyzer. A single extracted cell is trapped between two electrodes (stimulating and recording electrode) in a phosphate-buffered saline (PBS) medium. It is concluded that a living cell acts as a low-pass filter and that the electrical parameters of the cell membrane are frequency-dependent. The B16-F10 melanoma cancer cell does exhibit a very low specific capacitance ($1.154 \pm 0.29 \mu\text{F}/\text{cm}^2$), and a specific resistance of $3.9 \pm 1.15 \text{ K}\Omega \text{ cm}^2$, (mean \pm SEM, n = 14 Cells).

Cancer mechanobiology

Living cells are life's building blocks; they come in different forms, perform different tasks, and experience different motility (movement) mechanisms^{63–69}. Most sperm cells swim⁶⁵, whereas cancer cells generally crawl⁶⁶. Furthermore, some bacteria exhibit unique motility by rotating flagellar motors, in which a generated torque within the flagellum-ion-driven motor is passed to helical-propelled flagellar filaments via a hook-shaped joint⁶⁷. A fourth motility mechanism, experienced mainly through parasites, is known as gliding, which is driven by overlaying transmembrane proteins on a given substrate⁷⁰; it differs from crawling motility, in which the morphology of a cell is unaltered during cell migration⁷⁰. For a better understanding of the importance of cell mechanism and cellular motility, Table 1 is provided to demonstrate to the general reader the importance of cells as the structural and functional units of our existence, as well as to analyze various cellular motility phenomena via different movie presentations.

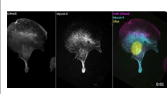
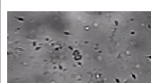
No	Sneak preview	QR code to the movie presentation	Brief description	Source/accredited to
a			This animated movie presentation amplifies to the general reader the importance of understanding cells as the building blocks of life	Produced for the first author of this paper by Gregorio Educational Productions
b			Microscopic video images illustrating the motility of a crawling melanoma cancer cell	Assoc. Prof. Dylan T. Burnette, School of Medicine, Dept. of Cell and Developmental Biology, Vanderbilt University
c			A Microscopic video presentation demonstrates the gliding motility of pear-shaped cells (Mycoplasma mobile r2 (Gli521[P476R])) moving directionally with the tapered end leading after adding an inhibitory antibody that dissociated the cells from the substrate. (For more details, please refer to Seto et al., J. Bacteriol. 187:3502–10, 2005)	Courtesy of Prof. Makoto Miyata, Department of Biology, Graduate School of Science, Osaka City University, Japan
d			Various microscopic videos at different magnifications and differential interference contrast lighting depicting numerous Ciliated Protista (single-cell microorganisms) motility by showing cilia, short hairlike organelles, utilized for motility locomotion and nutrient harvesting (For more details, please refer to Li et al., J. Microbiol) https://doi.org/10.3389/fmicb.2022.785502	Produced and sublicensed for the first author of this paper by Craig Smith, Insight Photography Inc
e			Sperm cells' motility was observed under a microscope	Courtesy of Dr. Tara Mahendran, Scientific Director at Andrology Center, Coimbatore, Tamil Nadu, India

Table 1. Movie presentations illustrate the importance of a cell as the building block of life and demonstrate different cellular motility mechanisms to general readers.

Cellular motility is responsible for numerous biological events. It plays a dominant role in constructing tissues and organs through dividing cells, denoted as morphogenesis⁶³. Moreover, wound healing is a remarkable process that involves three biological phenomena: cell migration (movement), diversified assigned cellular physiological tasks, and unique morphological shapes of each cell type, all of which collaborate in tissue reconstruction^{71,72}. In wound healing, distinctive electrochemical/mechanical signaling, received by the gene receptors of specific cells, would initiate the cellular movements and orchestrate the motilities of white blood cells, neutrophils, and digesting-bacterium defensive cells, known as macrophages, to terminate microorganisms responsible for the infection, and at the same time connective tissue cells, fibroblasts, engineer and reconstruct damaged tissues^{71,72}. Furthermore, the importance of cellular force lies within the nature of a disease; for instance, some bone diseases are attributable to a change of bone and endothelium cellular forces within their normal physiological environment⁶⁴. Similarly, heart failure is due to a loss of contractile force of the heart cells^{73–75}.

Parasites, with their unique gliding motility, yield human malaria through *plasmodium* parasite and human-related immunocompromised via *toxoplasma* and *cryptosporidium*⁷⁰. Tumorigenesis is a manifestation of cellular motility through the formation of a secondary tumor due to the development of cancer cells in a metastasized distant tissue/organ^{76–78}.

In this paper, the crawling motility of melanoma cancer cells is thoroughly investigated, together with the morphological changes of these cell lines based on their level of metastases. The cellular crawling migration goes into four segments: cellular leading-edge protrusion (pseudopodia anchorage), cellular leading-edge adhesion (preventing backward motion), cellular body/rear de-adhesion, and finally, cellular cytoskeleton contraction (pulling cell in one direction forward)^{63,68,70}; this process is depicted in Fig. 3. As shown, a cell consists of a nucleus, cell membrane, microtubules (MT), myosin motors, intermediate filaments (IF), focal adhesion, extracellular matrix substrate, and actin filaments (AFs) within the intracellular domain^{2,63,68}.

As shown in Fig. 3a, the cell is bounded by a membrane segregating the intracellular cytoskeleton region from the extracellular one^{2,63,68}. The cytoskeleton is a scaffolding network consisting of three-main-filament types based on their rigidity: actin filament (semi-flexible distinctive pairs of monomers), microtubules (stiffest rod-shaped polymer with functionalized treadmill motion), and intermediate filaments (most flexible, non-polarized ((static)))^{63,68}. At the cellular periphery, the radial extensions of microtubules (Fig. 3a), from the center to the AF network where the positive ends are in the direction of the cellular edge, assist in selecting the direction of the cell's movements^{68,79}.

The two distinctive (+/-) ends of an actin filament play a dominant role in the cell's motility, where the (−) actin monomer concentration is higher than that of a (+) end, and if the end of the AF is exposed to a higher monomeric concentration, polymerization takes place, where monomers grow, and bind^{63,68}. Alternatively, if the concentration is lower, de-attachment and shrinkage (de-polymerization) take place, where AFs extend asymmetrically^{63,68}. Therefore, polymerization, a higher rate extension process of the positive end than the negative end based on actin monomer concentration, is a critical factor in understanding cells' motility (forward momentum/treadmilling)^{63,68}. In addition to polymerization, cellular motility can be generated through the

interactions between AFs and myosin motors—a molecular motor converting chemical energy (ATP → ADP) to a mechanical work exerted on AFs, yielding a contractile force pushing a cell forward^{63,74}.

Significance of the melanoma model

This work adopts melanoma, a skin cancer, as a legitimate prime model in the proposed analysis of designing and characterizing versatile bio-mechatronic devices to examine the proposed hypothesis. Melanoma is initiated by melanocytes (pigment-melanin skin cells), hence gaining the name “melanoma.” Melanoma cells actively generate melanin that causes dark coloring and asymmetric patterns on the skin; they can be generated in any part of the human body^{80,81}. According to⁷⁶, it has been reported that melanoma cells have the highest occurrence in developing brain metastasis as opposed to other cancer cell types, where they migrate through the brain capillary endothelial cell layer, forming a morphological blood-brain barrier. A unique characteristic of melanoma is that it highly advocates mitosis, as it forms on skin tissue and other internal organs if injected intravenously. Accordingly, cutaneous melanoma is the one that is generated on the skin surface, whereas ocular malignant melanoma is an example of metastatic cancer⁸¹. Figure 4 illustrates ocular melanoma. Furthermore, melanoma possesses a high heterogeneity, rapid development, and experiences resistance to treatment, which makes it a remarkably difficult form of cancer to diagnose and treat at a very late stage.

In line with melanoma’s unique characteristic in advocating mitosis, Wilhelm et al.⁷⁶ have shed light on the pivotal role that malignant melanoma cells play in brain metastases at a very high frequency as opposed to other metastatic cells of other cancer diseases. This manifests the importance of melanoma cells’ motility (migration) to other organs via, e.g., capillaries in forming other metastatic colonies.

As aforementioned in Section “Cancer biology overview” of this paper, the main routes of cells are through the leading networks of blood vessels: arteries (bloodstream from the heart towards other parts of the mammalian body), veins (backward bloodstream from the body towards the heart), and minuscule (comparable to the size of a cell) interconnecting capillaries between veins and arteries. This justifies the fact that tumor cells are highly stimulated in the presence of rich blood vessels, e.g., as in a retina (Fig. 4). This is performed in a process denoted as tumor angiogenesis (a formation of new blood vessels)^{82–84}, which is associated with metastatic cancer. The cancer cells encourage the formation of new blood vessels into the tumor; this occurs by having cancer cells stimulating blood vessel cell proliferation by releasing endothelial cell growth-stimulating chemicals and proteins^{82–84}.

Malignant melanoma is generally categorized as a deadly disease, especially if discovered at an advanced stage. As per the American Cancer Society (ACS) 2023⁸⁵: Cancer Facts and Figures, the estimated number of new melanoma cancer cases and deaths for both genders are respectively 97,610 and 7,990 within the United States of America as of June 2023—not considering basal and squamous cell skin cancers. The ACS’s 2023 probability (%) analyses of invasive melanoma on Americans for the six age clusters of males (M) and females (F) are birth to 49 (M 1 in 246, F 1 in 162), 50–59 (M 1 in 205, F 1 in 247), 60–69 (M 1 in 114, F 1 in 191), 70 and older (M 1 in 38, F 1 in 88), and birth to death (M 1 in 28, F 1 in 41). Caucasians have the highest frequency of developing the disease⁸⁵.

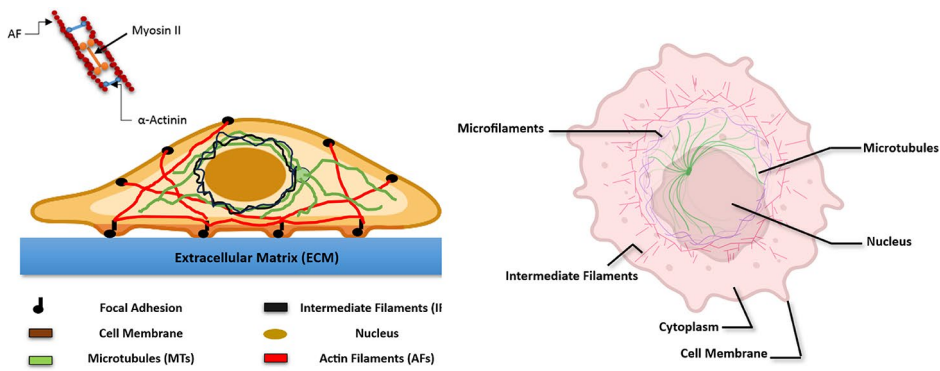
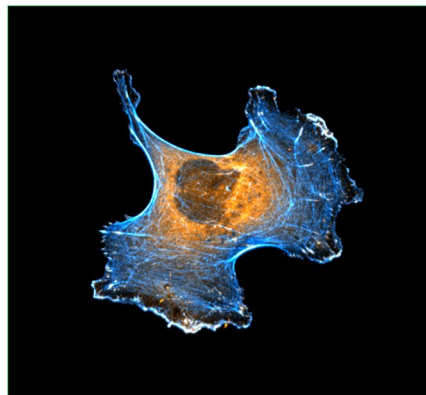
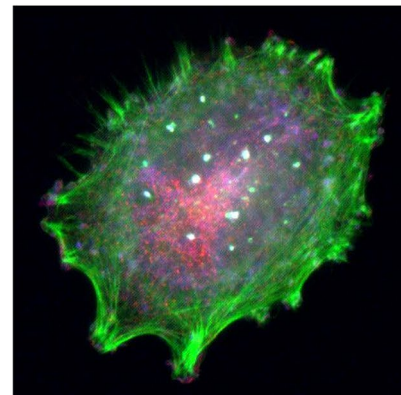
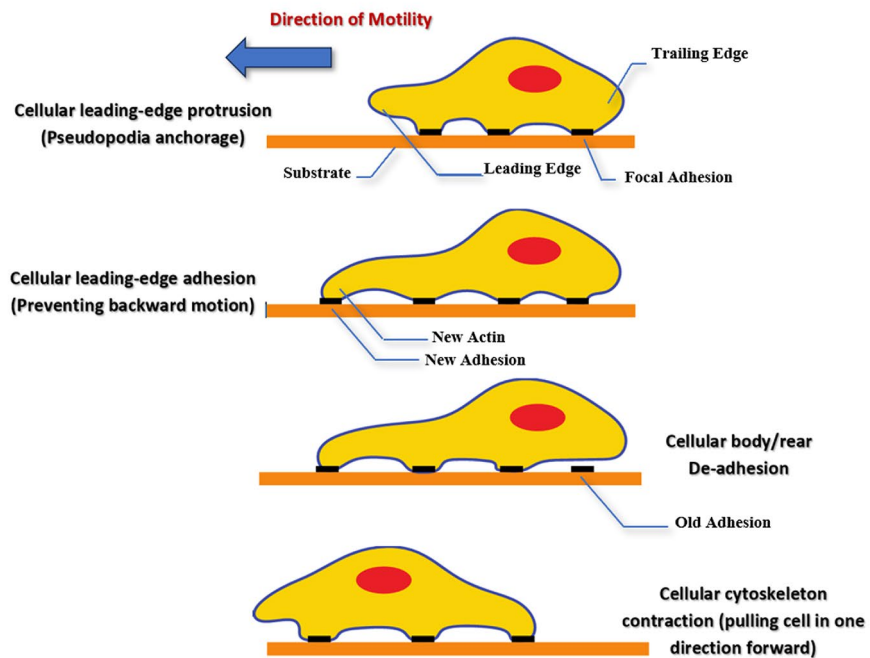
Melanoma exhibits four stages based on its thickness and cancer progression status within other tissues, organs, and lymph nodes⁸⁰: Stage 0 (in situ melanoma), Stage I (thickness dependency without skin pattern breakage), Stage II (thickness variations with/without skin pattern breakage), Stage III (invading lymph system), and Stage IV (invading other organs and tissues). Most skin cancers result from exposure to various forms of radiation; mortality is attributed to melanoma (highly invasive) as opposed to squamous and basal cell carcinomas⁸⁰.

A unique feature of melanoma is its ability to be self-immune from natural killer (NK) cells, in which the cancerous cell develops a self-defense system against immune response, as well as chemotherapy through molecules denoted as antigens, e.g., melanoma tumor-specific/associated antigens^{86,87}. In line with this unique feature, an example of the type of research work that is found to be most interesting is that by Tobias Schatton and colleagues⁸⁷, which proposed a novel therapeutic approach by targeting ABCB5+, a melanoma chemoresistance mediator and a newly defined marker of malignant-melanoma-initiating cells (MMIC); this ABC transporter, which is beyond the scope of this work, arbitrates chemoresistance within human malignant melanoma, by transporting ions (charges) of the cell membrane, and hence determines the cell-membrane potential of the cancer cell⁸⁷. This manifests the importance of the electrophysiology of cells, which will be presented mathematically in Section “Mathematical modeling of the electrophysiology of a living cell: analytical approach” for better comprehension of the research subject presented in this work.

A review of different approaches to the early recognition of melanoma

The survival rate of patients with advanced-stage melanoma is heavily dependent on early detection of the disease. Naik⁸⁸ defines the five stages of a tumor initiated by melanocytes known as cutaneous melanoma (CM)—a very aggressive, deadly skin malignancy. In his study, the early stages of the disease, stage 0 “in situ” to stage IIC, are defined as the states of having the tumor localized in a constrained skin tissue. This is followed by stage III, when cancer melanoma migrates from its original disease site to one or more lymph nodes (LN)s or locoregional territories (lymph vessel areas). Finally, metastatic stage IV is invoked when malignant melanoma invades other organs, such as the liver, pleura, lungs, and brain. Patients may suffer from clinical characteristics such as bleeding, persistent scratching, or crusting of a pigmented lesion; however, the majority of melanomas don’t show any symptoms, and local inflammatory symptoms are only experienced once malignancy development has commenced^{89,90}.

The first intuitive stage of clinical diagnosis involves a visual analysis based on morphological criteria carried out by a dermatologist aided by a lesion dermoscopy⁸⁸. The dermatoscope is a device empowered with polarized/

**a****b****c****d****e**

nonpolarized light source magnification of $\times 10$ to $\times 20$, enabling the examination of pigmented and unpigmented skin structures regardless of skin surface reflection⁹¹. Dermatologists visually examine melanocytic lesions using the essential ABCDE criteria (asymmetric shape, border, color, diameter, evolution); however, such criteria have been further improved specifically for melanocytic lesions within the foot and nail areas and abbreviated as

Fig. 3. Cellular motility. (a) Illustration of cell's cytoskeleton (cross-sectional view). (b) Illustration of cell's cytoskeleton (top view). (c) A human breast cancer cell imaged with Turku Bioscience Centre's SDC-microscope demonstrating the essential cellular components for a cell's motility: the cytoskeleton and adhesions are shown in blue and orange, respectively. The proteins depicted in the image are (F-) actin and vinculin (i.e., the adhesions are integrin-mediated adhesions). [Courtesy of Aleksi Isomursu, Cell Adhesion & Cancer Laboratory, Turku Bioscience Centre—University of Turku, Finland]. (d) An immunofluorescence microscopic image of a melanoma cell stained with antibodies against the cytoskeleton components, indicating their invasion/migration into the surrounding matrix—Melanoma (WM-793) is stained with phalloidin (F-actin, green), Cortactin (blue), and MT1-MMP (red). WM-793 cells grew on 0.2% gelatin matrix (not fluorescently labeled), where experimental details can be found in (PMID: 19535457, “Fluorescent Gelatin Degradation Assay”) [Credit Source: Courtesy of Yueyao Zhu and Wei Guo – Department of Biology, University of Pennsylvania, Philadelphia, Pennsylvania 19104, USA.]. (e) Four stages of cellular motility. Illustrative images are created with BioRender.com.

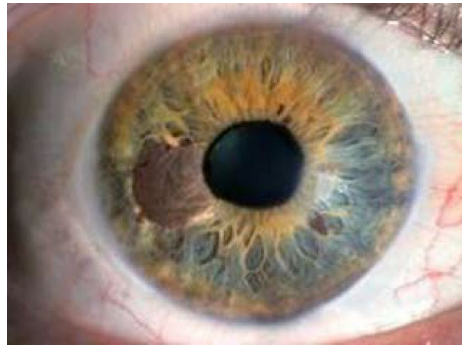


Fig. 4. Retinal melanoma formation (Courtesy of Emeritus Prof. Bertil Damato, MD, PhD, Ophthalmology, Liverpool Ocular Oncology Service).

CUBED (colored, uncertain, bleeding, enlarged, delay)⁸⁹. It should be noted that melanoma is not limited to individuals with lighter skin and hair tones with low melanin levels; it also encounters individuals with darker skin tones who have acral lentiginous melanomas (ALM) that exist in subungual spaces, hands, and soles, where visual clinical diagnosis is quite challenging^{88,89}. Furthermore, noninvasive image processing encounters image artifacts of varied lesion areas, structures, fuzzy borders, background overlap, hair reflections, and variations in skin color pigmentation⁹². In an attempt to degrade image artifacts, Sreelatha et al.⁹³ have highlighted the importance of enhancing pattern recognition techniques in image processing and prognosis of melanocytic lesions. Their lesion segmentation method is based on gradient and feature adaptive contour (GFAC) from the collected images of the dermatoscope, where image noises are deduced via multiple Gaussian distributed pattern methodologies. At an advanced imaging stage of individuals with a family history of melanoma, an in vivo reflectance confocal microscopy (RCM) is used to beam a laser of near-infrared wavelength of 830 nm as a coherent monochromatic light penetrating skin tissues of up to 300 μm imaging depth⁹¹.

Upon further analysis following the image processing stage, an adhesive patch biopsy is utilized to assess the necessity of the biopsy procedure^{88,89}. Once a suspicious lesion is identified, an excision biopsy (e.g., elliptical, punch, and saucerization) is performed for histopathologic evaluation. However, a complete excisional biopsy encounters difficulties in acral/face surfaces and complex nail matrices of suspected diffuse pigmentation, melanonychia striata, or amelanotic changes^{88,89}. Complete excisional biopsy is cumbersome to execute in challenging areas such as acral and patient's face surfaces, where other tedious biopsy techniques should be applied via shave, punch, or elliptical/fusiform incisional biopsy⁸⁸. Moreover, a biopsy on a single tumor lesion cannot precisely depict tumor sub-clones and those with high metastasis potential⁹⁴.

The prognoses and differentiation of malignant versus benign melanoma involve non-invasive optical coherence tomography, optical-based thermography, photodynamic, sonography, gene expression analysis, electrical impedance spectroscopy, tissue elastography, fiber diffraction, and reflectance confocal microscopy⁸⁸. A description of each methodology mechanism is provided in⁸⁸, where the optical-based non-biopsy diagnosis of skin cancer is performed by passing a light wave into the skin tissue and correlating the reflected scattered light to the stage of the disease. On the other hand, the photodynamic-based approach induces a photosensitive marker in the suspected area to identify the presence of tumor cells. The sonography mechanism transduces collected signals of the reflected propagation of sound wave properties into electrical signals that determine the disease stage. The thermal imaging mechanism detects electromagnetic radiation emitted by an object whose temperature is above absolute zero and correlates collected measurements to the stage and grade of the disease; this technique differentiates between healthy and melanoma lesions via infrared imaging processing since cancerous lesions experience higher metabolic activity than healthy ones, and thus differ in temperature⁸⁸. Microscopic observations are conducted to assess the number of dermal mitotic figures, amplify cellularity, and analyze cytologic atypia.

At the distinctive electrophysiology of melanoma cancerous cellular scale, electrical impedance spectroscopy (EIS) is a noninvasive technology used for detecting malignancy by emitting painless, very low-voltage electrical current⁹⁵. Given the unique electrochemical of the targeted tissue, the electrical current emitted by EIS transduces a signal reading of 0–10, with 0–3 of normal tissue and 4–10 of predicted melanoma⁹⁵. From a mechanical testing perspective, tissue elastography is performed to assess the elastic deformation of a tissue, where normal tissue easily deforms as opposed to a malignant one; this procedure is conducted by imposing light pressure via an ultrasonic transducer resulting in ultrasonic imaging of the scanned lesion⁹⁶. Finally, the noninvasive gene expression detection method is performed by a real-time polymerase chain reaction (PCR), where cell-isolated RNA is amplified, followed by hybridization with U133 plus 2.0 GeneChip human genome Affymetrix⁹⁷.

The above non-biopsy diagnosis mechanisms are mostly hospital-based, difficult to calibrate, costly, susceptible to poor variable sampling time, limited to the type of biomarkers used, constrained with the number of collected data samples, and time-consuming, leading to diagnostic delays and a lack of specificity and sensitivity of each method. They also experience motion control constraints of patients that might lead to false results. Therefore, scholars in the field shifted their attention toward a minimally invasive procedure in identifying circulating tumor cells (CTCs) derived from melanoma. Thus, a new field in detecting tumorigenesis, denoted as “liquid biopsy,” has emerged. CTCs, as an indication of distanced metastases, originate from a solid tumor and travel via the peripheral blood^{94,98,99}. They are the cornerstone of forming metastases at distant organs, forming cancer of secondary type.

Metastatic cutaneous melanoma was the first malignancy in which CTCs were discovered via mRNA transcript detection biomarker, and other forms of CTCs for other types of cancers followed, e.g., breast, prostate, lung, and colorectal cancers^{94,98,99}. CTCs are prognostic biomarkers, and they are beneficial when a biopsy cannot be implemented due to the inaccessibility of the tumor or when a patient suffers from multiple metastases^{94,98,99}. Marsavela et al.⁹⁸ have highlighted melanoma CTC's detection and molecular characterization methodologies and other cancers' enrichment. They illustrated that for the detection module, several techniques could be implemented, such as immunostaining, fluorescence in situ hybridization (FISH), next-generation sequencing (NGS), droplet digital polymerase chain reaction (PCR), and real-time polymerase chain reaction RT-PCR. As for the enrichment module, filtration and immunoenrichment are exercised, whereas advanced methods for discriminating CTCs have been applied through the dielectrophoresis (DEP) method or via the microfluidics approach. However, there are constraints facing the clinical utilization of melanoma CTCs, such as their short life cycles, rarity in peripheral blood, highly pronounced molecular heterogeneity and phenotype with multiple none-overlapping subpopulations, limited number of blood samples, and lack of unified isolation protocol^{98,99}. Furthermore, blood samples for CTC analysis are hard to obtain from cancer patients with malignant tumors having an inserted port-a-cath due to poor venous access.

The highly profound heterogeneity of melanoma CTCs advocates the need for a novel strategy to quantify the stages of the disease at a cellular level. It is concluded in⁹⁹ that a multi-biomarker strategy should be imposed to detect CTCs in melanoma as opposed to an individual approach. Thus, the findings of this work in relating cellular contractile force to its associated electrophysiology could potentially contribute to differentiating the heterogeneity of melanoma CTCs at the phenotypic and molecular level, contributing to real-time disease management and monitoring of targeted treatment. Kurma and Alix-Panabières¹⁰⁰ highlight the mechanobiology and survival tactics of CTCs during invasive metastatic cascade motility when they encounter a capillary bed during extravasation/intravasation. Their study analyses highlight the adaptations of CTC within the microcirculation in the harsh bloodstream system to survive through molecular factors and interfacing with other cells and blood components (e.g., immune cells and platelets inside capillaries)—promoting metastasis in distant organs.

Regmi et al.¹⁰¹ have demonstrated that under-exercised conditions, high-shear stresses (HSSs) experienced within a microfluid system destroy CTCs. They have fabricated a microfluidic circulatory module to analyze the effects of hemodynamic fluid on CTCs of ovarian, lung, leukemic, and breast cancer cells at variant metastatic phenotypes. They arrive at three findings; first, CTCs got destroyed at a given condition of HSSs attaining a value of 60 dynes cm⁻², whereas low shear stresses (LSSs) of 15 dynes cm⁻², such as that experienced by human arteries at resting state preserve the tumorigenesis of CTCs; second, within the first 4 h of circulation, HSS leads to necrosis in over 90% of CTCs, where the survived CTCs within the 4-h circulation underwent apoptosis within 16–24 h of post circulating incubation; lastly, extended imposing of HSS treatment efficiently hinder the viability of highly metastatic and drug-resistant breast cancer cells, whereas leukemic cells mimicking white blood cells were less affected. However, it has been thoroughly demonstrated in^{100,102} that CTCs adjust to the surrounding microenvironment of capillaries via their mechanobiology characteristics, such as stiffness, contractility, and deformability (i.e., the cellular tendency to modify its shape under biomechanical forces experienced in the microcirculation system). This facilitates their extravasation and promotes metastasis generation, where cell motility is dominant when actin stress filaments plant anchorage seeding at other favorable host microenvironments identified as the premetastatic niche (PMN)^{100,102}.

In line with the premise of this work, which investigates a mathematical representation depicting the interrelation of cellular electrophysiology in stimulating cellular motility, Lee et al.¹⁰³ study the influence of fluid shear stress in activating yes-associated protein 1 (YAP1) to promote cancer motility. They've developed a biomimetic platform to simulate the mechanical properties of microfluidic movements experienced by tumor cells. They have proved that fluid frictional force within the lymphatic microenvironment activates YAP1 to promote cancer cell motility, whereas the generated forces of fluid wall shear stress (WSS), as in venous or arterial flow, stall taxis. They concluded that YAP1 was swiftly stimulated by low-level WSS typical of the lymphatic vasculature to promote cancer cell motility. Thus, this amplifies the premise of this work that cancerous cells' unique biophysics and mechanobiology enable them to refrain from apoptosis and reach infinite and rapid division without relying on growth factors and angiogenesis⁸⁸. Thus, differentiating the distinctive biophysical

activities embodied in the cellular electrochemical domain that allows for cellular motilities (invasion of distanced organs) shall provide medical practitioners and biotechnologists a solid platform to detect cancer at a cellular level, achieving more successful targeted therapies to combat metastasis, enhancing prognosis stage, and lowering mortality rate among melanoma patients. Furthermore, differentiating various stages of melanoma based on its biophysical characteristics and interrelating that feature to its mechanobiology and morphology at a cellular level shall provide oncologists with a bioinformatic tool to detect the disease at a cellular level and tailor an effective targeted therapy to combat the mitosis aspect of the disease, which is the prominent premise of this interdisciplinary work.

Analyzing the mechanobiology and biophysics of melanoma CTCs is beyond the scope of this work. However, the anticipated collected bioinformatic data of various melanogenesis cells in terms of their electrophysiology, dependent contractile force, and associated cellular morphology shall enrich the exponentially growing field of artificial intelligence (AI) within the convolutional neural networking module. This shall be the extension of this work, potentially leading to a novel diagnostic supplement and attaining an effective targeted therapy allocation.

Significance of the electrochemical approach as opposed to other non-conventional methodologies

To provide a comprehensive research study on the subject of cellular electrophysiology, especially to novice readers, this section first highlights the merits, drawbacks, and mechanisms of different non-conventional methodologies utilized to analyze the characteristics of cells: surface acoustic wave (SAW), optical fluorescence, and electrochemical approach. By advocating the last approach, a vast literature review of experimental findings on cancer electrophysiology has been provided in Section “[Cancer electrophysiology](#)” manifest the heterogeneity of tumorigenesis on the essence of the biophysics of cells. This should provide a solid platform and a sense of high appreciation for the importance of cellular biophysics’ role in cancer formation before invoking the subject of mathematical modeling of the biophysics of cancer cells (Section “[Mathematical modeling of the electrophysiology of a living cell: analytical approach](#)”), with its detailed derivations and flourished empirical solutions. Hence, in addition to the aforementioned limitations and constraints of conventional approaches in detecting cancer at a cellular level, illustrated in the introduction section of this paper, non-conventional techniques have been investigated, which include SAW-based sensors, lab-on-a-chip (LoC), optical fluorescence, and electrochemical-based approach.

SAW sensors are compact and can be wirelessly controlled^{104–106}. The operation of SAW biosensors is based on placing a targeted biological specimen between two interdigital transducers (IDTs): input and output IDT^{104–106}. The piezoelectric-based input IDT is stimulated by voltage, generating acoustic waves. The waves propagate, crossing over a biological model towards the output IDT, where the acoustic waves are captured and transduced by mechanical deflections of the output IDT fingers^{104–106}. The problems of the acoustic-wave-based approach are in fourfold: (1) it requires lengthy calibration processes^{107,108}; (2) the wave propagation is difficult to control¹⁰⁹; (3) a pre-knowledge of acoustic wave properties associated with the biological system is necessary that can lead to a limited sensitivity, and specificity feature in terms of detecting any biological phenomena¹¹⁰, and (4) most importantly, acoustic waves could be invasive, and hence can endanger healthy cells¹¹¹.

The optical fluorescence-based approach processes molecular images at various illumination wavelengths^{39,48,112,113}. This approach is non-invasive, yet it exhibits a “dark” signal noise constraint¹¹⁴, like the SAW approach, its sensitivity is dependent on the species’ size^{110,115,116}. Finally, an electrochemical-based approach is established by sensing the electrophysiological potentials of living cells. This approach, as manifested in Alqabandi et al.², relies on chemical potential experienced within a living cell domain; it offers high resolution and sensitivity of measurements, where the change rate of ionic concentration is dynamic, so is the biological system: reporting a close to a real-time response². Thus, this paper highly advocates the electrochemical approach for extracting the electrophysiology of cancer cells as one of two significant factors differentiating cancer cells at various stages. The other important factor lies within the field of mechanobiology (contractile force), which shall be further addressed in Section “[In vitro real-time characterization of melanoma contractile force via a self-probing cantilever-based biomechatronic platform](#)” of this paper.

Typical methods of extracting the cell-membrane potential via an electrochemical approach are classically pursued through three techniques: a patch clamp^{19,49,117}, voltage-sensitive fluorescent dyes^{19,39}, and utilization of nano/microelectromechanical means^{2,19,52}. A patch clamp could be invasive and doesn’t faithfully represent the cell-membrane potential in the cell’s intended normal living environment⁴⁹. The voltage clamp approach is described as fixing (clamping) the membrane potential at a fixed value, where a pipette and electrodes are used, which leads to no capacitive current flow of the cell membrane; thus, the total membrane current equals the ionic current^{19,49,117}. On the other hand, the voltage-sensitive fluorescent dye method is based on optical detection of the percentage difference experienced in fluorescence dye molecules when interacting with the electric field of the cell membrane^{19,48}. It is worth re-stating that cell-membrane potential is also referred to in the literature as transmembrane potential.

Despite the simplicity of the voltage-sensitive fluorescent dye approach in preparations, its unique feature of being implemented to a population of cells, the applicability of analyzing the spatial profile of cell-membrane potential, and unlike patch clamp, it can detect a minute change of cellular physics within a biological structure. Yet, it experiences significant drawbacks^{19,39}. The deficiencies of the dye optical detection method are mainly due to calibration constraints, limited sensitivity to capture various biological electrochemical phenomena at once, and the extensive usage of such dye is limited and needs to be improved in obtaining confidence in the measured cell-membrane potential. It experiences difficulty attaining an absolute value of cell-membrane potential^{19,39,118}.

The third approach is an exponentially growing field in extracting the electrophysiology of cells based on utilizing nano/mirco-electro-mechanical-system (N/MEMS) technology. It is demonstrated that by placing a cell between two electrodes in a microfluidic channel, the presence of the cell will generate a potential difference

between the electrodes; upon a specific stimulation, the cell-membrane potential can be obtained^{2,19,52}. Moreover, this approach allows the registration of the biophysics of a single, as well as a population of cells; also, it analyzes signal propagation in temporal and spatial domains, lessens cross contaminations, maintains cell viability due to the merits associated with the miniaturized LoC in terms of biocompatibility, thermal stability, neutralized acidity (pH), controlled supply of nutrients and oxygen, as well as disposal of wastes and carbon dioxide in a high throughput, less laborious, and cost-effective working environment. Moreover, it avails the benefit of controlling signal propagation instead of the random propagation of signals experienced in a petri dish. In addition, this technique provides reusability for countless experiments and stability in obtained measurements. Therefore, in this work, such an approach concept is highly promoted. Figure 5 summarizes the various non-conventional methods addressed within this paper in studying the biophysical characteristics of cells.

Mathematical modeling of the electrophysiology of a living cell: analytical approach

Considerable research efforts are being geared towards finding new instrumentations and detection techniques of cancer at a cellular level that would overcome the problems and limitations of the currently existing ones, e.g., CT scan, X-ray, MRI, PET, and bone scan^{6–17}. Cell electrophysiology plays a pivotal role in cancer formation, which has initiated the necessity to develop a device that could detect the biophysics of cells^{2,19,39,52}. Furthermore, cellular electrophysiology is considered a cornerstone in understanding cellular phenotype mutation in different phases, cellular motility, apoptosis, mitosis, tissue reconstruction, inflammation healing, and cell-cell communication via ion and gap junction processing of signals^{2,39,119}. Moreover, it has defined two classes of cells: Excitable (action potential propagating cells), such as neurons, muscle cells, and endocrine, as well as non-excitable cells (non-propagating action potential cells), such as fibroblast tissue cells, fat cell adipocytes, and endothelial cells within the boundary interior of veins, capillaries, and arteries^{39,119}. Thus, detecting such cellular phenomena can be a label-free biomarker of cell status, type, and functionalities. However, it is fundamentally noteworthy to state that to optimally design, characterize, fabricate, and test a functionalized biosensor that would detect such cellular phenomena is to initially understand the biophysics of cells and investigate the controlling parameters of cellular electrophysiology. Therefore, this section sheds light on a vital

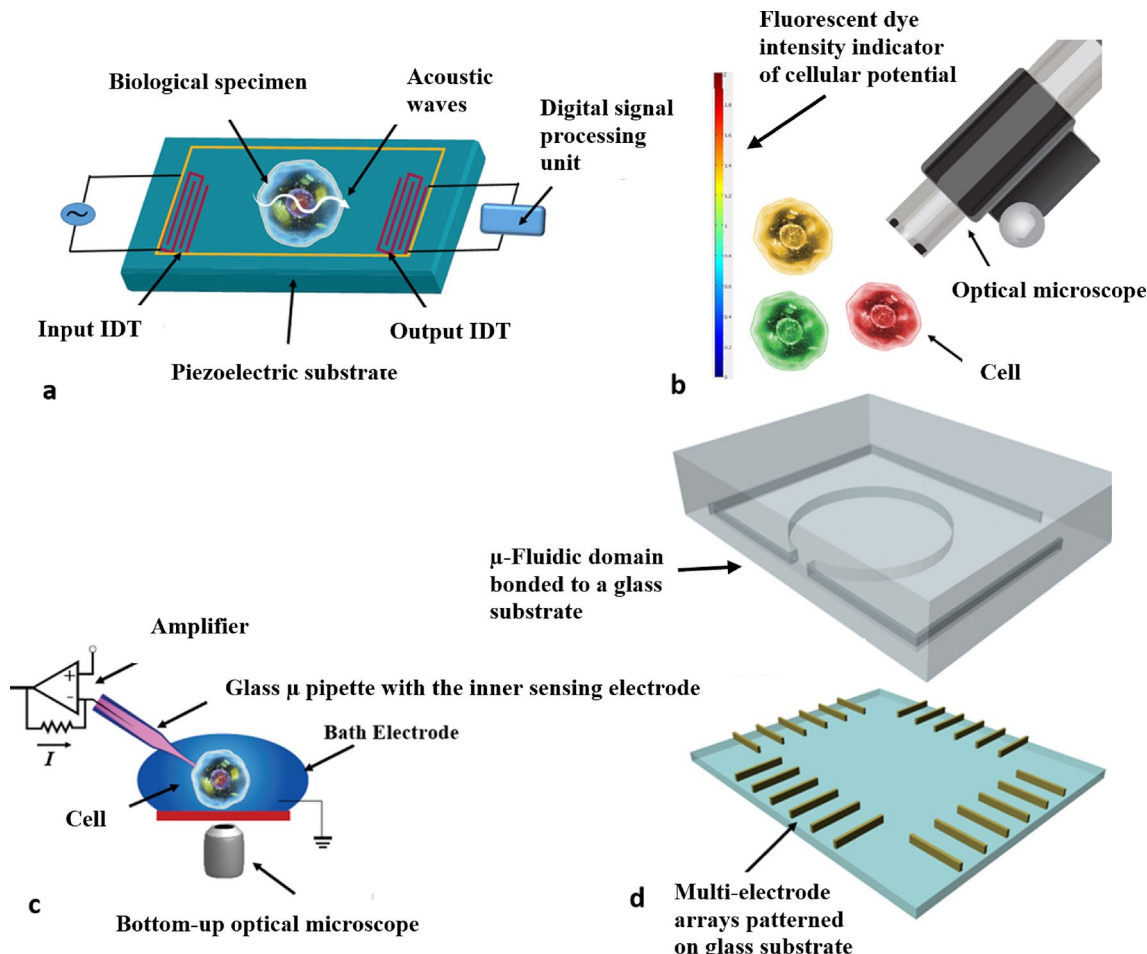


Fig. 5. Non-conventional methods in studying the characteristics of cells: (a) SAW-based sensor. (b) Optical Fluorescent Sensor. (c) Patch Clamp Method. (d) N/MEMS technology consisting of a microfluidic and multi-electrode-array domain.

aspect of the proposed research methodology, which is the mathematical modeling of the electrophysiology of cells; understanding the dominant controlling parameters' role in shaping the physics associated with cellular electrophysiology should tremendously shorten lead time and alleviate costs and efforts before conducting bio-experiments—enabling researchers to simulate and tentatively predict the outcomes of experiments without the suffer and cost associated with ordering, incubating, and culturing of cells. Furthermore, the development of the mathematical modeling would assist in effectively analyzing the obtained experimental results prior to microfabricating a customized biosensor and, hence, efficiently validating the developed analytical model with the experimental findings.

As per the reviewed literature in Section “[Cancer electrophysiology](#)”, cells exhibit unique cellular biophysics that can be utilized as a label-free tool in discriminating various stages of cancer. However, it is essentially vital that before microfabrication, the design of microelectronics with dedicated controlling software and, eventually, the extraction of cellular electrophysiology to assess the proposed hypothesis, the cellular biophysics, and its associated controlling parameters should be first comprehended. Mathematical modeling unlocks the key to understanding the biophysics behavior of cells; furthermore, it assists in obtaining an efficient tool for designing of experiments (DOEs) and further predicts and justifies obtained experimental findings in testing the proposed hypothesis and arriving at the concluded theorem raised in this work.

Overview of the mathematical approach of cellular electrophysiology

In biochemistry, two anchor mathematical models are highly pronounced in literature, which have enormously impacted the understanding of cellular biophysics: The Nernst–Plank equation^{[120–124](#)} and the Hodgkin–Huxley cable model^{[125–128](#)}. Those great scholars, Planck, Hodgkin, and Huxley were awarded Nobel Prizes. Hodgkin and Huxley received the award in 1963 in Physiology or Medicine, whereas Planck received the Nobel Prize in Physics in 1919. Their findings have greatly enriched the understanding of the mechanisms of electrophysiology, especially within the fields of neuroscience, cardiology, endocrinology, cellular functionalities, muscle tissue contractions, and neuroinformatics.

The Nernst–Planck equation depicts electro-diffusion, mass transport phenomena, and chemical particles' kinematics within a medium^{[120–124](#)}. Its applications are not just limited to free ion kinematics, yet it extends to encounter the effect of pairing and clustering multiple ion transport^{[120](#)}; this equation can be coupled with other theorems, e.g., Poisson theorem, to extend its applicability^{[123](#)}. Furthermore, it models the biological ion channels by considering ions in the spatial and temporal domains as charged-hard spheres of excess potential^{[122](#)}. Nernst equation describes the equilibrium potential of different ion concentrations, and thus it cannot depict cell-membrane potential; however, it can only describe cell-membrane potential if one ion type concentration is evaluated, excluding other ions' concentrations, which does not faithfully describe the biological system of various contributions of multiple ion channels^{[119](#)}. It should have been noted in the aforementioned reviewed literature on cell-membrane potentials (Section “[Cancer electrophysiology](#)” of this paper) the different magnitudes and signs of cell-membrane potential, which suggest that cell-membrane potentials in literature can have either negative or positive signs with magnitude; this is justified mathematically by the natural logarithmic component of the Nernst–Planck equation in that the differences in signs are indications of higher or lower ion concentrations of intracellular to extracellular region, or vice versa, with respect to the cell membrane^{[119,129](#)}. Also, this is physically attributable to the hyperpolarization and depolarization nature of cells due to the flux of specific nutrients out and in the cell^{[43,45,47–49,130](#)}.

The second standout mathematical model, the Hodgkin–Huxley model, consists of a set of four non-linear differential equations, which initially exemplified the membrane potential of nerve impulses. This placed their mathematical work at a high rank in bridging the gap between theoretical and experimental approaches^{[125,126](#)}. They measured membrane potential within a giant axon of a squid by filling a capillary tube with seawater and then inserting it into the axon to act as an electrode, enabling the extraction of potential difference in millivoltage within the membrane; this experimental setup has contributed significantly to developing their mathematical modeling, and equivalent analogical electric circuit, and further predicting ion channels that modern technology have approved of their existence^{[125](#)}.

As in the Nernst–Planck model, the Hodgkin–Huxley model has opened new frontiers for researchers to extend its application by combining the cable model with other theories to suit their specific experimental setup. For example, Roth and Basser^{[128](#)} developed a model of electromagnetic induction on a passive (voltage-independent) nerve fiber, and they complemented their mathematical model with that of Hodgkin and Huxley.

Many scholars rely on models that are either discrete or lumped; however, a continuous system more efficiently mimics, to some extent, living structures, and hence, it is considered more accurate in closely capturing cellular physics. Furthermore, many researchers in the bio-field don't encounter the resistivity of the medium surrounding the living cell (extracellular isopotentiality). In addition, the cell membrane is considered passive. This initiates the necessity of having active/passive cell membrane functionalities by inducing an active injected current at an effective node within an RC circuit in developing the mathematical model. In addition, a leakage factor illustrated by Warburg diffusion^{[2,131](#)} must be present in a continuous model to closely capture, to a certain degree, the electrophysiology of a stimulated cell by encountering diffusion (leakage) of charges/ions. These are among the novel objectives of this paper in extending the mathematical model of the cell's biophysics, which shall be illustrated in the following subsection.

Development of the mathematical model of cellular electrophysiology

The living cell is a complex and harsh system that can be further simplified and closely examined through mathematical representations^{[132](#)}. This subsection is devoted to providing novice readers with an in-depth understanding of the physics and controlling parameters associated with the generation of cell-membrane potential. As partly depicted in Fig. 6, cells consist of water, inorganic ions (i.e., Na^+ , Ca^{2+} , Cl^- , Mg^{2+} , etc.),

macromolecules (DNA/RNA), and micro-organic molecules (i.e., vitamins, sugars, proteins, cholesterol, and fatty acids)^{25,119}. A mammalian living cell consists of three main regions: extracellular, cell membrane, and intracellular medium (cytoplasm), as shown in Fig. 6a. The cell membrane, Fig. 6b, is of a closed boundary, and its thickness varies from 65 to 100 Å (10^{-10} m), and it is considered amphipathic since it consists of arrays of a phospholipid bilayer, Fig. 6c: hydrophilic (water-loving) head, and two hydrophobic (water-fearing) tails¹¹⁹. Accordingly, the cell membrane then segregates two conductive media with a high dielectric property. Hence, the cell membrane experiences a capacitance behavior. Similarly, there is a potential drop between the intracellular and extracellular domain, and such drop resembles a membrane resistance, as shown in Fig. 6d. As per the latter figure, the cell membrane is considered in biophysics as a series of parallel RC circuits, where the total capacitance is distributed into the capacitive and resistive current. Finally, Fig. 6e shows a microscopic image of a population of liver cells, illustrating the cell membrane, cytoplasm, and nucleus.

The electrochemical potential of a cell is attributable to the ion transfer between the intracellular and extracellular domains by diffusion via ion channels (voltage-gated channels (Fig. 6b)), ATP pumping, and/or biological transporters^{2,19,39,122}. Therefore, the biophysics of a cell can be represented as a network of electrical circuitry, as depicted in Fig. 6d, which explains the cell's distinctive electrophysiology that initiates various signal-transduction activities, such as mitosis and cell-cell communication^{2,19,39}. This makes the field of

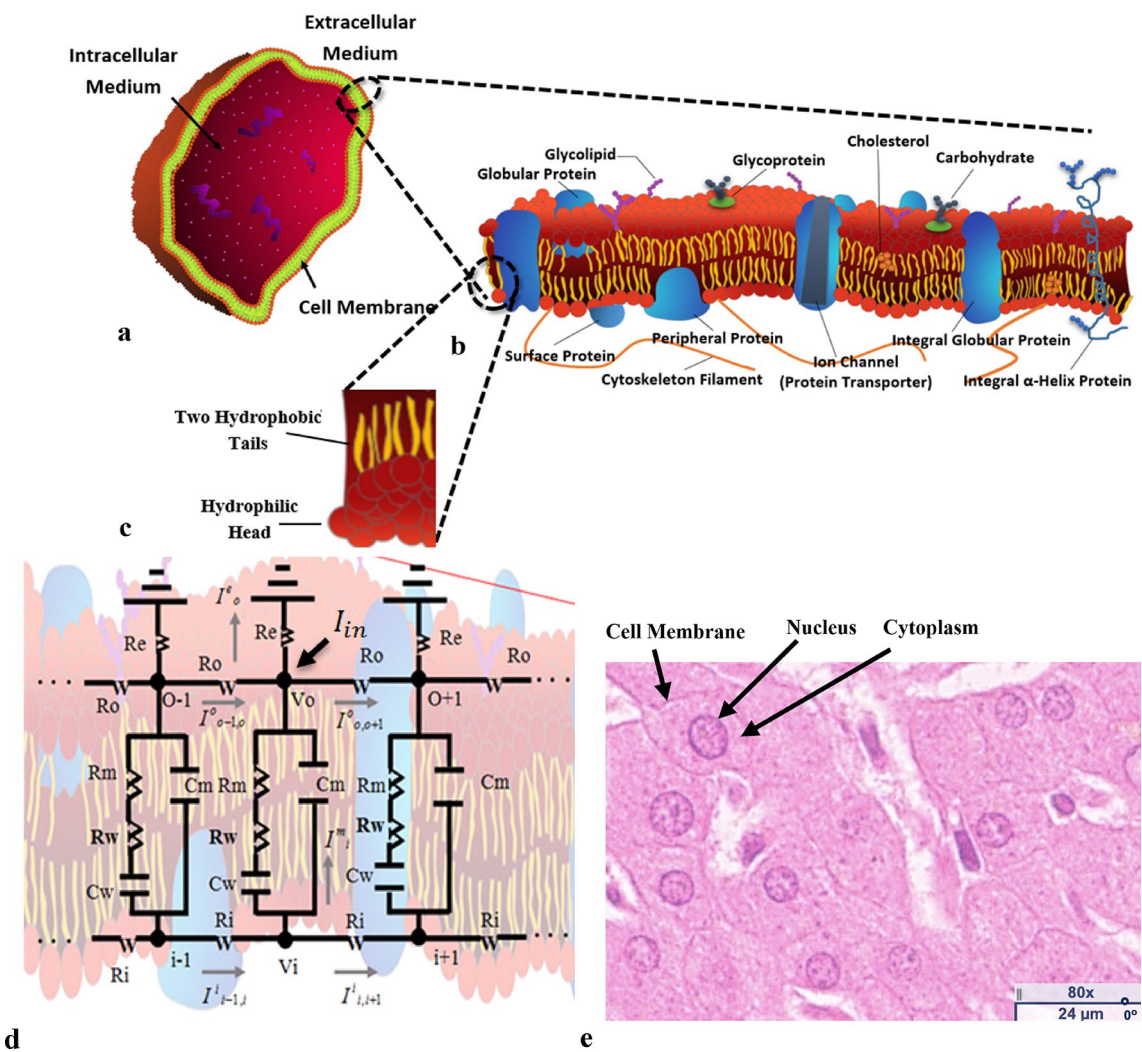


Fig. 6. Living cell formation. (a) a living cell with three distinctive regions: cell membrane, extracellular, and intracellular region. (b) exploded view of the cell membrane, where cellular arrays of phospholipid bilayer are shown in (c). In (d), an electric circuit representation of a series of parallel RC circuits experienced within a cell membrane, where cell-membrane resistance is denoted as R_m (Ω), cell-membrane capacitance is denoted as C_m (F), R_i is the longitudinal internal resistance (Ω), R_o is the longitudinal resistance of current flow (Ω), R_e is the resistance of physiological medium (Ω), R_w is the Warburg resistance (Ω), C_W is the Warburg capacitance (F), and I_{in} is the effective current injection from an electrode (A). (e) A microscopic image with a scale bar of a population of liver cells showing cell membrane, cytoplasm, and nucleus: Hematoxylin and eosin (H&E) stain, a very kind courtesy of Dr. Ahmad Al-Taleb, Consultant Histopathologist, Histopathology Unit, Mubarak Al-Kabeer Hospital, State of Kuwait.

Symbol	Unit	Description
C_m	F (Farad)	The capacitance of the cell membrane
C_w	F (Farad)	The capacitance of Warburg diffusion (leakage of charge)
C_{me}	F (Farad)	Equivalent capacitance of Warburg and cell membrane capacitors in parallel
R_m	Ω (Ohm)	Resistance of cell membrane
R_w	Ω (Ohm)	Resistance of Warburg diffusion (leakage of charge)
R_{me}	Ω (Ohm)	The equivalent resistance of Warburg and cell membrane resistors in series
R_i	Ω (Ohm)	Longitudinal intracellular resistance of the living cell
R_o	Ω (Ohm)	Longitudinal resistance to current flow
R_e	Ω (Ohm)	Resistance of the buffered medium
I_{in}	A (Ampere)	Effective current injected from a stimulated electrode

Table 2. Controlling parameters of the electrical circuitry resembling a living cell.

Circuit diagram	Constitutive relation after applying Ohm's law
	$I_{j-1,j}^o = \frac{V_{j-1}^o - V_j^o}{R_o}$
	$I_{j,j+1}^o = \frac{V_j^o - V_{j+1}^o}{R_o}$
	$I_j^e = \frac{V_0 - (V_{earth}=0)}{R_e}$
	$I_j^m = C_{me} \frac{dV_j^m}{dt} + \frac{V_j^m}{R_{me}}$ Where the first term defines current via a capacitance (Q (charge) = CV ; $dQ/dt = C dV/dt$; $I = C dV/dt$), whereas the second term defines current via a resistance

Table 3. Ohm's representations of the external node characteristics of a living cell.

biophysics more pronounced within this study, where cell electrophysiology and cellular energy production play a dominant role in cancer formation and motility that can be detected and quantified^{2,19,39}.

This section provides detailed derivations to effectively grasp the concept of cells' electrophysiology. It extends the analytical model carried out in¹³⁰ by accounting for Warburg diffusion impedance (charge leakage)^{2,131}, as shown in Fig. 6d. As experimentally proofed in Alqabandi et al.², Warburg diffusion plays a vital role in justifying the phase angle shift for not reaching 90° in a typical potential current phase angle configuration; instead, a 45° is being reached, implying ion diffusion of slow species/charge kinematics within the electrochemical domain. The mathematical representation of the cable model's cell-membrane potential is based on Kirchhoff's Current Law, Laplace and Fourier Transforms, and their Inverse Transforms.

It is assumed that a cell, close to a sphere shape, is trapped between two electrodes (stimulating and recording) within a microfluidic chamber in an in vitro experimental setup. The assumptions are carried out such that (1) the living cell is stimulated via injection of an effective current (I_{in}) at a cell's single external node (o), as shown in Fig. 6d and (2), the direction of current flow is taken randomly, and the opposite can also be assumed. The current flow is longitudinal near the cell interior boundary, radial from the cell to the extracellular domain, and then to the grounded recording electrode. The extracellular medium has uniform resistivity. Also, the recording electrode potential is set with respect to the ground. The following table (Table 2) summarizes the circuit model's controlling parameters, representing the cell's electrophysiological characteristics.

By examining the external node (j^o), and applying Ohm's law, we arrive at the following constitutive relations that are illustrated in Table 3:

The mathematical representations of capacitive and resistive current flow exhibit the characteristics of outflow current experienced biologically within ATP pumps and transporters in transferring charged ions. Next, in a similar manner, at the internal node (j^i), the constitutive relations are defined in the following table (Table 4):

Where, $I_{j-1,j}^o$, $I_{j-1,j}^i$, I^o , V_j^m , V_j^i , and V_j^o , are respectively the exterior current from node (j-1) to node (j), interior current from node (j-1) to node (j), exterior current, membrane potential, intracellular potential,

and extracellular potential. Applying Kirchhoff's Current Law (KCL) at the external and internal nodes, where the charge is conserved, and hence “I” is conserved ($I_{innode} = I_{outnode}$).

$$I_{j-1,j}^o - I_{j,j+1}^o + I_j^m - I_j^e + I_{in}\delta_{jo} = 0 \quad (1)$$

The Kronecker delta term, $\delta(x)$, is introduced into Eq. (1) to set current injection “On” or “Off,” and it is defined as:

$$\begin{aligned} \delta(x) &= \begin{cases} 0 & x \neq 0 \\ \infty & x = 0 \end{cases} \\ \int_{-\infty}^{\infty} \delta(x) dx &= \text{area} = 1 \\ \int_{-\infty}^{\infty} f(x) \delta(x) dx &= f(0) \end{aligned}$$

At internal node:

$$I_{j-1,j}^i - I_{j,j+1}^i - I_j^m = 0 \quad (2)$$

Rewriting Eqs. (1) and (2) in terms of potential at both external and internal nodes. Therefore, the following terms are obtained:

At external node:

$$\frac{V_{j-1}^o - 2V_j^o + V_{j+1}^o}{R_o} + C_{me} \frac{dV_j^m}{dt} + \frac{V_j^m}{R_{me}} - \frac{V_j^o}{R_e} + I_{in}\delta_{jo} = 0 \quad (3)$$

At internal node:

$$\frac{V_{j+1}^i - 2V_j^i + V_{j-1}^i}{R_i} - C_{me} \frac{dV_j^m}{dt} - \frac{V_j^m}{R_{me}} = 0 \quad (4)$$

Equations (3) and (4) describe a lumped equivalent system, whereas a biological system is continuous. Thus, Eqs. (3) and (4) shall be converted into continuous equations by taking a differential small element (Δx). It should be noted that R_i 's and R_o 's are in series, while R_e 's, C_{me} 's, and R_{me} 's are in parallel. Therefore,

$$\begin{aligned} \frac{1}{R_{me,eqv}} &= \frac{1}{R_{me}} + \frac{1}{R_{me}} + \dots + \frac{n}{R_{me}} = \frac{n}{R_{me}} = \frac{\Delta x}{r_{me}} \Rightarrow R_{me} = \frac{r_{me}}{\Delta x} \\ \frac{1}{R_{e,eqv}} &= \frac{1}{R_e} + \frac{1}{R_e} + \dots + \frac{n}{R_e} = \frac{n}{R_e} = \frac{\Delta x}{r_e} \Rightarrow R_e = \frac{r_e}{\Delta x} \\ C_{me,eqv} &= C_{me} + C_{me} + \dots + nC_{me} = \Delta x C_{me} \\ R_{o,eqv} &= R_o + R_o + \dots + nR_o = \Delta x r_o \\ R_{i,eqv} &= R_i + R_i + \dots + nR_i = \Delta x r_i \end{aligned}$$

As for $\delta(x)$

Circuit diagram	Constitutive relation after applying Ohm's law
	$I_{j-1,j}^i = \frac{V_{j-1}^i - V_j^i}{R_i}$
	$I_{j,j+1}^i = \frac{V_j^i - V_{j+1}^i}{R_i}$
	$I_j^m = C_{me} \frac{dV_j^m}{dt} - \frac{V_j^m}{R_{me}}$ Where, first term defines current via a capacitance ($Q(\text{charge}) = CV$; $dQ/dt = C dV/dt$; $I = C dV/dt$), whereas second term defines current via a resistance

Table 4. Ohm's representations at the internal node characteristics.

$$\begin{aligned}
\delta(x) &\rightarrow \frac{1}{c}\delta(x) \\
x &= cX \\
\int_{-\infty}^{\infty} \delta(x)f(x)dx &= \int_{-\infty}^{\infty} \frac{1}{C}\delta(x)f(cX)dX \quad \text{by definition.} \\
\text{Also, by definition,} \\
\int_{-\infty}^{\infty} \delta(x)dx &= 1 \quad \text{and since } x = cX \\
&= \int_{-\infty}^{\infty} \delta(cX)d(cX) = C \int_{-\infty}^{\infty} \delta(cX)dX = 1 \\
\delta(cX) &= \frac{1}{c}\delta(x) \\
\int_{-\infty}^{\infty} \delta(x)f(x)dx &= f(0) \quad \text{by definition, and since } x = cX \\
C \int_{-\infty}^{\infty} \delta(cX)f(cX)dx &= \int_{-\infty}^{\infty} \delta(x)f(cx)dx \\
&= \frac{1}{c}\delta(x) = f(cx0) = f(0) \\
\therefore \delta(cX) &= \frac{1}{C}\delta(x) \quad \therefore \delta(cX) = \frac{1}{C}\delta(x) \text{ Where } c \text{ is some constant .}
\end{aligned}$$

Thus, the following terms are defined:

$$\left. \begin{array}{l} R_{me} \rightarrow \frac{r_{me}}{\Delta x} \\ R_i \rightarrow r_i \Delta x \\ \delta_{jo} \rightarrow \delta(x) \Delta x \end{array} \right\}; \quad \begin{array}{l} C_{me} \rightarrow C_{me} \Delta x \\ R_o \rightarrow r_o \Delta x \end{array} \quad (5)$$

Substituting terms of Eq. (5) into (3) and (4).
For Eq. (4)

$$\frac{V_{j+1}^i - 2V_j^i + V_{j-1}^i}{r_i(\Delta x)} - C_{me} \Delta x \frac{dV_j^m}{dt} - \frac{V_j^m}{r_{me}} \Delta x = 0 \quad (6)$$

Multiplying Eq. (6) by $\frac{1}{\Delta x}$, and by taking the limit $\Delta x \rightarrow 0$, the following term is obtained.

$$\text{As } \lim_{\Delta x \rightarrow 0} \frac{1}{r_i} \frac{\partial^2 V_i}{\partial x^2} - C_{me} \frac{\partial V_m}{\partial t} - \frac{V_m}{r_{me}} = 0 \quad (7)$$

For Eq. (3)

Multiplying the above term by $\frac{1}{\Delta x}$, the following equation is obtained:

$$\frac{1}{r_o} \frac{\partial^2 V_o}{\partial x^2} + C_{me} \frac{\partial V_m}{\partial t} + \frac{V_m}{r_{me}} - \frac{V_o}{r_e} + I_{in} \delta(x) = 0 \quad (8)$$

To simplify Eqs. (7) and (8), time and distance are rescaled, which yields:

$$\begin{aligned}
X &= x \sqrt{\frac{r_i}{r_{me}}} \rightarrow x = X \sqrt{\frac{r_{me}}{r_i}} \\
T &= \frac{t}{\tau_{me}} \rightarrow t = T \tau_{me} = T r_{me} C_{me} \\
k &= \frac{r_o}{r_i}; \mu = \frac{r_{me}}{r_e}; v = \sqrt{r_{me} r_i}; \tau_{me} = r_{me} C_{me}
\end{aligned}$$

Since $\delta(x) = \delta\left(X \sqrt{\frac{r_{me}}{r_i}}\right) = \sqrt{\frac{r_i}{r_{me}}}\delta(X)$, and with the above simplification expressions, Eq. (8) becomes:

$$\frac{r_i}{r_o r_{me}} \frac{\partial^2 V_o}{\partial X^2} + \frac{\partial V_m}{r_{me} \partial T} + \frac{V_m}{r_{me}} - \frac{V_o}{r_e} + I_i \sqrt{\frac{r_i}{r_{me}}} \delta(X) = 0$$

Multiplying both sides by r_{me}

$$\frac{\partial V_m}{\partial T} + V_m = -\frac{1}{k} \frac{\partial^2 V_o}{\partial X^2} + \mu V_o - v I_{in}(T) \delta(X) \quad (9)$$

Similarly, for Eq. (7), substituting the above simplification expressions and then multiplying both sides by r_{me}

$$\frac{\partial^2 V_i}{\partial X^2} = \frac{\partial V_m}{\partial T} + V_m \quad (10)$$

Thus, the cell-membrane potential is defined as the difference between the intracellular and extracellular potential: $V_m = V_i - V_o$

Equations (9) and (10) are two coupled partial differential equations (PDEs) that depict the physics of the biological system. They are second-order PDEs within a spatial domain (X variable), so two boundary conditions are required. Also, they are first-order PDEs, so one initial condition is required in the temporal domain (T variable). Proper boundary and initial conditions are essentially important to describe the bio-environment efficiently.

Boundary conditions (finite biological system):

$$V_i(X, T) \rightarrow 0, V_o(X, T) \rightarrow 0 \text{ as } |X| \rightarrow \pm L, \text{ where } L \text{ is the length of the cell.}$$

Or

$$\frac{dV}{dX} = 0, \quad X = \pm L$$

Initial condition

$$V_m(X, T = 0) = 0$$

For a step current injection:

$$I_{in}(T) = \begin{cases} 0 & T < 0 \\ -I_o & T \geq 0 \end{cases}$$

For a rectangular pulse input:

$$I_{in}(T) = \begin{cases} -I_o & 0 \leq T \leq T_o \\ 0 & \text{Otherwise} \end{cases}$$

Rearranging the finally obtained terms:

$$\frac{\partial V_m}{\partial T} + V_m = -\frac{1}{k} \frac{\partial^2 V_o}{\partial X^2} + \mu V_o - v I_{in}(T) \delta(X) \quad (9)$$

$$\frac{\partial^2 V_i}{\partial X^2} = \frac{\partial V_m}{\partial T} + V_m \quad (10)$$

where

$$\begin{aligned} V_m(X, T) &= V_i(X, T) - V_o(X, T) \\ k &= \frac{r_o}{r_i}; \mu = \frac{r_{me}}{r_e}; v = \sqrt{r_{me} r_i}; X = x \sqrt{\frac{r_i}{r_{me}}}; T = \frac{t}{\tau_m}; \tau_m = r_{me} C_{me} \\ I_{in}(T) &= I_o \sin(\omega t) \quad 0 < T < \infty \end{aligned}$$

The partial differential equations shall be solved using the Fourier and Laplace Transform method, extensively used in feedback control theory, electronic circuits, and heat mass transfer. The tedious calculus problems are transformed into algebraic ones, and the Laplace and Fourier Inverse Transforms allow shifting between spatial and temporal variables to a parameter 's' domain and vice versa: The parameter 's' can be considered a conditional constant. The Laplace Transform complements the shortage of obtaining a function definition that the Fourier Transform failed to have.

Applying the Laplace Transform with respect to (T), the Laplace transform is defined as,

$$\bar{V}(s) = \mathcal{L}\{V(t)\} = \int_0^\infty e^{-st} V(t) dt$$

The Laplace transform of a derivative of a function is defined as:

$$\mathcal{L}\left[\frac{df}{dt}\right][s] = s\mathcal{L}[f][s] - f[0]$$

Thus, respectively, Eqs. (9) and (10) become,

$$\begin{aligned} s\bar{V}_m + \bar{V}_m &= -\frac{1}{k} \frac{\partial^2}{\partial x^2} \bar{V}_o + \mu \bar{V}_o - v \mathcal{L}[I_{in}(T)] \delta(x) \\ s\bar{V}_m + \bar{V}_m &= \frac{\partial^2}{\partial x^2} \bar{V}_i \end{aligned}$$

Now since,

$$\begin{aligned}\mathcal{L}[I_{in}(T)] &= \int_0^\infty e^{-sT} I_{in}(T) dT = I_o \int_0^\infty e^{-sT} \sin(wT) dT \\ \because \sin(wT) &= \frac{e^{iwT} - e^{-iwT}}{2i} \quad (\text{Euler's definition}) \\ \therefore \mathcal{L}[I_{in}(T)] &= I_o \int_0^\infty e^{-sT} \frac{e^{iwT} - e^{-iwT}}{2i} dT = \frac{I_o}{2i} \int_0^\infty [e^{(iw-s)T} - e^{-(iw+s)T}] dT \\ &= \frac{I_o}{2i} \left\{ \frac{1}{iw-s} e^{(iw-s)T} \Big|_0^\infty + \frac{1}{iw+s} e^{-(iw+s)T} \Big|_0^\infty \right\} = \frac{I_o}{2i} \left[\frac{1}{s-iw} - \frac{1}{s+iw} \right] \\ &= \frac{I_o}{2i} \frac{s+iw - s-iw}{s^2 + w^2} = \frac{I_o}{2i} \frac{2iw}{s^2 + w^2} = \frac{I_o w}{s^2 + w^2}\end{aligned}$$

Thus, Eqs. (10) and (9) would respectively become,

$$s\bar{V}_m + \bar{V}_m = \frac{\partial^2}{\partial x^2} \bar{V}_i \quad (11)$$

$$s\bar{V}_m + \bar{V}_m = -\frac{1}{k} \frac{\partial^2}{\partial x^2} \bar{V}_o + \mu \bar{V}_o - v \left[\frac{I_o w}{s^2 + w^2} \right] \delta(x) \quad (12)$$

Applying Fourier Transform to Eqs. (11) and (12) with respect to X, and by utilizing the definition of Fourier Transform:

$$\bar{\bar{V}} = F\{f(x)\} = \hat{f}(w) = \int_{-\infty}^{\infty} f(x) e^{-iwx} dx$$

Revising Fourier Transform properties is essential for the following derivations. Therefore, if the Fourier Transform is defined as the following,

$$F(w) = F\{f(t)\} = \frac{1}{\sqrt{2\pi}} \int_{-\infty}^{\infty} f(t) e^{-iwt} dt$$

and if the function $f(t)$ is defined as a differential function with Fourier Transform (FT) $F(w)$, then FT of its derivative is given by $iwF(w)$, which can be used to transform differential equations into algebraic ones. It is important to note that such an approach only applies to problems whose domain consists of a set of real numbers. Accordingly, the FT of a Kronecker delta function (δ) is,

$$F\{\delta(x)\} = \frac{1}{\sqrt{2\pi}} = \frac{1}{\sqrt{2\pi}} \int_{-\infty}^{\infty} \delta(x) e^{ixy} dx$$

As a result, Eqs. (11) and (12), respectively, become

$$s\bar{\bar{V}}_m + \bar{\bar{V}}_m = -y^2 \bar{\bar{V}}_i \quad (13)$$

$$\begin{aligned}\text{And since } F\left\{\frac{\partial}{\partial x}\right\} &= -iy \rightarrow \therefore F\left\{\frac{\partial^2}{\partial x^2}\right\} = [-iy]^2 \\ \therefore i = \sqrt{-1} \rightarrow \therefore F\left\{\frac{\partial^2}{\partial x^2}\right\} &= -y^2\end{aligned}$$

$$s\bar{V}_m + \bar{V}_m = \frac{y^2}{k} \bar{V}_o + \mu \bar{V}_o - \frac{v}{\sqrt{2\pi}} \frac{I_o w}{s^2 + w^2} \quad (14)$$

Since the cell-membrane potential is defined as $\bar{V}_m = \bar{V}_i - \bar{V}_o$, hence Eqs. (13) and (14) respectively become,

$$[s+1] [\bar{V}_i - \bar{V}_o] = -y^2 \bar{V}_i \quad (15)$$

$$[s+1] [\bar{V}_i - \bar{V}_o] = \frac{y^2}{k} \bar{V}_o + \mu \bar{V}_o - \frac{v}{\sqrt{2\pi}} \frac{I_o w}{s^2 + w^2} \quad (16)$$

Rearranging Eq. (15):

$$\bar{V}_o = \frac{1+s+y^2}{1+s} \bar{V}_i \quad (17)$$

Plugging Eq. (17) into Eq. (16)

$$\overline{\overline{V}}_i = -\frac{v}{\sqrt{2\pi}} \frac{I_o w}{s^2 + w^2} \frac{1+s}{-\left(\frac{s(y^2+\mu k+y^2k)+ky^2+(y^2+1)(y^2+\mu k)}{k}\right)}$$

In order to simplify the expression, the following terms are defined:

$$\begin{aligned} P &= ky^2 + (y^2 + k\mu) (1 + y^2) \\ Q &= ky^2 + y^2 + \mu k \end{aligned}$$

Thus,

$$\overline{\overline{V}}_i = \frac{vk}{\sqrt{2\pi}} \frac{I_o w}{s^2 + w^2} \frac{1+s}{(P + sQ)} \quad (18)$$

Substituting (18) into (17)

$$\overline{\overline{V}}_i = \frac{vk}{\sqrt{2\pi}} \frac{I_o w}{s^2 + w^2} \frac{(1+s+y^2)}{(P + sQ)} \quad (19)$$

At this stage, double transformed ($\overline{\overline{V}}_i, \overline{\overline{V}}_o$) as functions of y and s , e.g., $\overline{\overline{V}}_i(y, s), \overline{\overline{V}}_o(y, s)$, are obtained. Therefore, the Laplace Inverse Transform is required to move from the spatial domain parameter (s) to a temporal domain (t). In order to perform the Inverse Laplace Transform, partial fractions are implemented with the exclusion of constant terms, and by just evaluating the “ s ” term.

$$\begin{aligned} \overline{\overline{V}}_i : \frac{1+s}{(s^2 + w^2)(P + sQ)} &= \frac{1+s}{(s - iw)(s + iw)(P + sQ)} \\ &= \frac{A}{s - iw} + \frac{B}{s + iw} + \frac{C}{P + sQ} \\ &= \frac{A(s + iw)(P + sQ) + B(s - iw)(P + sQ) + C(s^2 + w^2)}{(s - iw)(s + iw)(P + sQ)} \\ &= \frac{(AQ + BQ + C)s^2 + (AP + BP - BiwQ + AiWQ)s + iwPA - iwPB + w^2C}{(s - iw)(s + iw)(P + sQ)} \end{aligned}$$

Equating coefficients:

$$s^2 : AQ + BQ + C = 0 \rightarrow C = -AQ - BQ \quad (20)$$

$$s : PA + iwAQ + BP - iwBQ = 1 \quad (\text{Multiplying both sides by } iw)$$

$$APiw - w^2AQ + iwBP + w^2BQ = iw \quad (21)$$

$$\text{Constant} : APiw - BPiw + Cw^2 = 1 \quad (22)$$

Plugging Eq. (20) into (22), the following term is obtained.

$$APiw - BPiw - w^2AQ - w^2BQ = 1 \quad (23)$$

Adding Eq. (21) to (23), and solving for A, this yields

$$\begin{aligned} 2iwAP - 2w^2AQ &= iw + 1 \\ \frac{1+iw}{2iwP - 2w^2Q} &= \frac{1+iw}{2w(ip - wQ)} \end{aligned}$$

Subtracting Eq. (21) from (23) and solving for B

$$\begin{aligned} 2iwBP + 2w^2BQ &= iw - 1 \\ B &= \frac{iw - 1}{2w(ip + wQ)} \end{aligned}$$

Finally,

$$\begin{aligned} C &= -Q[A + B] = \frac{-Q}{2w} \left[\frac{1+iw}{ip - wQ} + \frac{iw - 1}{ip + wQ} \right] = \frac{-Q}{2w} \left[\frac{ip + wQ - wP + iw^2Q - wP - iw^2Q - ip + wQ}{-P^2 - w^2Q^2} \right] \\ &= \frac{Q}{2w} \left[\frac{2wQ - 2wP}{P^2 + w^2Q^2} \right] = \frac{Q(Q - P)}{P^2 + w^2Q^2} \end{aligned}$$

Reconsidering constants by referring to the table of Inverse Laplace Transform ($\frac{1}{s-a} \rightarrow e^{at}$). Thus, the Inverse Laplace Transform of \bar{V}_i with respect to "s" is given by

$$\bar{V}_i(y, T) = \frac{vk}{\sqrt{2\pi}} I_o w \left[\frac{1+iw}{2w(iP-wQ)} e^{iwT} + \frac{iw-1}{2w(iP+wQ)} e^{-iwT} + \frac{Q(Q-P)}{(P^2+w^2Q^2)-Q} e^{-\frac{P}{Q}T} \right] \quad (24)$$

Similarly, the same process is applied for $\bar{\bar{V}}_o$

$$\begin{aligned} \bar{\bar{V}}_o : \frac{1+s+y^2}{(s^2+w^2)(P+sQ)} &= \frac{1+s+y^2}{(s-iw)(s+iw)(P+sQ)} = \frac{A}{s-iw} + \frac{B}{s+iw} + \frac{C}{P+sQ} \\ &= \frac{A(s+w)(P+sQ)+B(s-iw)(P+sQ)+C(s^2+w^2)}{(s^2+w^2)(P+sQ)} \\ &= \frac{(AQ+BQ+C)s^2+(AP+iwQA+BP-iwBQ)s+iwAP-iwAP-iwBP+cw^2}{(s^2+w^2)(P+sQ)} \end{aligned}$$

Equating coefficients

$$\begin{aligned} s^2 : AQ+BQ+C &= 0 \\ C &= -AQ-BQ \end{aligned} \quad (25)$$

$$s : AP+iwQA+BP-iwBQ = 1 \quad (\text{Multiplying both sides by } iw)$$

$$iwAP-w^2AQ+iwBP+w^2BQ=iw \quad (26)$$

$$\text{Constant} : APiw-iwBP+Cw^2=1+y^2 \quad (27)$$

Plugging Eq. (25) into (27), this results in,

$$iwAP-iwBP-w^2AQ-w^2BQ=1+y^2 \quad (28)$$

Adding Eq. (26) to (28), the following term is obtained:

$$2iwAP-2w^2AQ=1+y^2+iw$$

Finally, subtracting (26) from (28)

$$2iwBP+2w^2BQ=iw-1-y^2$$

Therefore,

$$A = \frac{1+y^2+iw}{2w(ip-wQ)}; B = \frac{iw-1-y^2}{2w(iP+wQ)} \quad (29)$$

And for C:

$$\begin{aligned} C &= -Q(A+B) \\ C &= \frac{Q(Q-P+Qy^2)}{P^2+w^2Q^2} \end{aligned} \quad (30)$$

Similarly, constants for $\bar{\bar{V}}_o$ are considered, and by referring to the Inverse Laplace Transform table ($\frac{1}{s-a} \rightarrow e^{at}$), the Inverse Laplace Transform of $\bar{\bar{V}}_o$ with respect to "s", is defined as,

$$\bar{\bar{V}}_o(y, t) = \frac{vk}{\sqrt{2\pi}} I_o w \left[\frac{1+y^2+iw}{2w(ip-wQ)} e^{iwT} + \frac{iw-1-y^2}{2w(iP+wQ)} e^{-iwT} + \frac{Q(Q-P+Qy^2)}{(P^2+w^2Q^2)Q} e^{-\frac{P}{Q}T} \right] \quad (31)$$

Multiplying each denominator and numerator of Eqs. (24) and (31) by its complex conjugate ($a+ib \rightarrow a-ib$), putting over a common denominator to make the numerator real:

For Eq. (24)

$$\bar{V}_i(y, T) = \frac{vk}{\sqrt{2\pi}} I_o w \left[e^{iwT} \frac{(-wQ-iP-iw^2Q+wP)}{2w(w^2Q^2+P^2)} + e^{-iwT} \frac{(iw^2Q+wP-wQ+iP)}{2w(wQ^2+P^2)} + e^{-\frac{P}{Q}T} \frac{(Q-P)}{(P^2+w^2Q^2)} \right]$$

Using the identities:

$$\begin{aligned} e^{+iwT} &= \cos(wT) + i\sin(wT) \\ e^{-iwT} &= \cos(wT) - i\sin(wT) \\ \bar{V}_i(y, T) &= \frac{vk}{\sqrt{2\pi}} I_o w \left[\frac{1}{w(w^2Q^2 + P^2)} [-wQ \cos(wT) + wP \cos(wT) + P \sin(wT) + w^2Q \sin(wT)] + \left[e^{-\frac{P}{Q}T} \frac{(Q-P)}{(P^2+w^2Q^2)} \right] \right] \end{aligned}$$

This is an even function of y since only embedded y^2 within the equation appears. Similarly, after multiplication of the complex conjugate of the numerator and denominator of Eq. (31) and using the same identities used for \bar{V}_i , the following term is obtained for \bar{V}_o :

$$\bar{V}_o(y, t) = \frac{vk}{\sqrt{2\pi}} I_o w \left[\frac{w(P-Q-y^2Q) \cos(wT) + (P+w^2Q+y^2P) \sin(wT)}{w(w^2Q^2 + P^2)} + \frac{(Q-P+Qy^2)}{(P^2+w^2Q^2)} e^{-\frac{P}{Q}T} \right]$$

$\bar{V}_o(y, T)$, also appears to be an even function in y and by taking the Inverse Fourier Transform with respect to y

$$\begin{aligned} V_i(X, T) &= \frac{1}{\sqrt{2\pi}} \int_{-\infty}^{\infty} e^{-iyX} \bar{V}_i(y, T) dy \\ V_o(X, T) &= \frac{1}{\sqrt{2\pi}} \int_{-\infty}^{\infty} e^{-iyX} \bar{V}_o(y, T) dy \end{aligned}$$

Knowing that:

- $e^{-iyX} = \cos(yX) - i\sin(yX)$
- $\cos(y, X)$ is an even function.
- $\bar{V}_i(y, T)$ and $\bar{V}_o(y, T)$ are also even functions as per the obtained derivations.
- $\sin(y, T)$ is an odd function.
- Integration of an odd function over a symmetric interval = 0

$$\begin{aligned} \int_{-a}^a f(x) dx &= 0 \quad \text{if } f(x) \text{ is odd.} \\ \int_{-a}^a f(x) dx &= 2 \int_0^a f(x) dx \quad \text{if } f(x) \text{ is an even function.} \end{aligned}$$

Therefore,

$$V_i(X, T) = \sqrt{\frac{2}{\pi}} \int_0^{\infty} \cos(yX) \bar{V}_i(y, T) dy \quad (32)$$

$$V_o(X, T) = \sqrt{\frac{2}{\pi}} \int_0^{\infty} \cos(yX) \bar{V}_o(y, T) dy \quad (33)$$

Hence, the two-coupled-partial differential equations, Eqs. (9) and (10), are transformed into two integrals, where,

The cell-membrane potential is defined as:

$$V_m = V_i - V_o \quad (34)$$

where

$$\bar{V}_i(y, T) = \frac{vk}{\sqrt{2\pi}} I_o w \left[\frac{1}{w(w^2Q^2 + P^2)} [-wQ \cos(wT) + wP \cos(wT) + P \sin(wT) + w^2Q \sin(wT)] + \left[e^{-\frac{P}{Q}T} \frac{(Q-P)}{(P^2+w^2Q^2)} \right] \right] \quad (35)$$

$$\bar{V}_o(y, t) = \frac{vk}{\sqrt{2\pi}} I_o w \left[\frac{(w(P-Q-y^2Q) \cos(wT) + (P+w^2Q+y^2P) \sin(wT))}{w(w^2Q^2 + P^2)} + \frac{(Q-P+Qy^2)}{(P^2+w^2Q^2)} e^{-\frac{P}{Q}T} \right] \quad (36)$$

where

$$\begin{aligned} P &= ky^2 + (y^2 + k\mu)(1 + y^2) \\ Q &= ky^2 + y^2 + k\mu \\ k &= \frac{r_o}{r_i} \mu = \frac{r_{me}}{r_e} v = \sqrt{r_{me} r_i} r_{me} = r_m + r_w \end{aligned}$$

When setting the Warburg impedance to nil (zero), the obtained results are in agreement with the findings of the peer-reviewed work in¹³⁰; this validates the full derivations carried out in this paper. As per the obtained

results, all capacitance terms have explicitly vanished from the fully derived cell-membrane potential, which could mislead the general reader by suggesting that the capacitive factor does not play a role in shaping the cell-membrane potential. However, as shall be further elaborated on in Section “[Discussion of the empirical results](#)”, in short, the capacitive term does play a role, and mathematically, such a role is implicit.

Empirical solution of the mathematical model of cellular electrophysiology

The transformed Eqs. (32) and (33), are respectively the intracellular and extracellular potential, and their difference gives the membrane potential of a cell (V_m). The two integral equations are evaluated numerically using symbolic Maple 16 (Maplesoft, Ontario, Canada), and resultant figures of cell-membrane potential with respect to time and space are obtained via an M-File command processed through MATLAB 7.12 (The Mathworks Inc., Natick, MA). The numerical algorithms shall allow different scenarios to be drawn; hence, the dependencies among controlling physical parameters in shaping the cell-membrane potential can be analyzed. Due to a lack of experimental findings of intercellular and extracellular physical parameters, the values are assigned subjectively considering three scenarios: all parameters are equal to unity, and some resistivity is higher or lower in magnitude than others.

The arbitrarily selected parameters should provide in-depth analyses in presenting the concept of electrophysiology of cells, and this shall further investigate the dependencies among controlling parameters of the analogical circuit of the living cell. The following table (Table 5) summarizes three different scenarios evaluated numerically.

Discussion of the empirical results

The cyclic events of rise and drop of the cell-membrane potential of any mammalian cells, as shown in the numerically generated figures (Figs. 7, 8, 9, 10, 11, 12, and 13), are the initiation of numerous events of cell-cell communication, as well as intracellular activities that would lead to cell motility and eventually exertion of contractile forces, where the latter are of particular interest in cell mechanobiology that shall be further addressed in Section “[In vitro real-time characterization of melanoma contractile force via a self-probing cantilever-based biomechatronic platform](#)” of this paper in examining the proposed hypothesis. Slightly deviating from the main topic of this research, investigating such electrophysiology of cells is quite beneficial within the cardiology field by understanding the mechanisms of defibrillation in case of a cardiac heart arrest medical emergency, ECG monitoring, and configuration of pacemaker electrodes¹³³. Also, this aids in understanding the staging of neuron diseases such as that of multiple sclerosis (MS)¹³⁴.

The generated figures (Figs. 7, 8, 9, 10, 11, 12, and 13) illustrate that cell-membrane potential is a function of time and space. It should be noted that those numerically generated figures are dimensionless. In analytical biophysics, dimensionless parameters are introduced to illustrate the relationships among different variables, in our case, dimensionless cell-membrane potential, spatial and temporal domain without specific reference to their units of measurement. Thus, such parameters assist in characterizing the biophysical behavior of a cell and provide insights into various dependent phenomena.

The subfigures b of Figs. 7, 8, 9, 10, 11, 12, and 13 clearly demonstrate that the slope of the cell-membrane potential to unit time defines the power of the amount of work performed in moving charged ions within the cell membrane from intracellular to extracellular domain (or vice versa): the intercellular to extracellular potential difference defines cell-membrane potential resembled as an exerted work per unit charge of any moving charged nutrients/ions against an electric field. This is crucially important that despite the vanished capacitive terms in the finally obtained equation of cell-membrane potential, the cell's overall implicit capacitive nature is still present. This also illustrates the active characteristic of the developed circuit, on the essence of the injected effective current, and in the presence of the passive components of the system: resistors and capacitors.

Scenarios		Case	r_o	r_i	κ	r_m	r_w	r_{me}	r_e	μ	v	I_o	W
I	all = unity	1	1	1	1	1	1	2	1	2	$\sqrt{2}$	1	1
II	κ = variable	1	4	0.25	1	1	2	1	2	$2\sqrt{2}$	1	1	
	μ = fixed	1	2	0.5	1	1	2	1	2	2	1	1	
	v = variable	6	3	2	1	1	2	1	2	$\sqrt{6}$	1	1	
III	κ = fixed	1	1	1	2	1	3	1	3	$\sqrt{3}$	1	1	
	μ = variable	1	1	1	4	2	6	1	6	$\sqrt{6}$	1	1	
	v = variable	1	1	1	6	3	9	1	9	3	1	1	

Table 5. Numerical solution of arbitrarily selected parameters: three different scenarios.

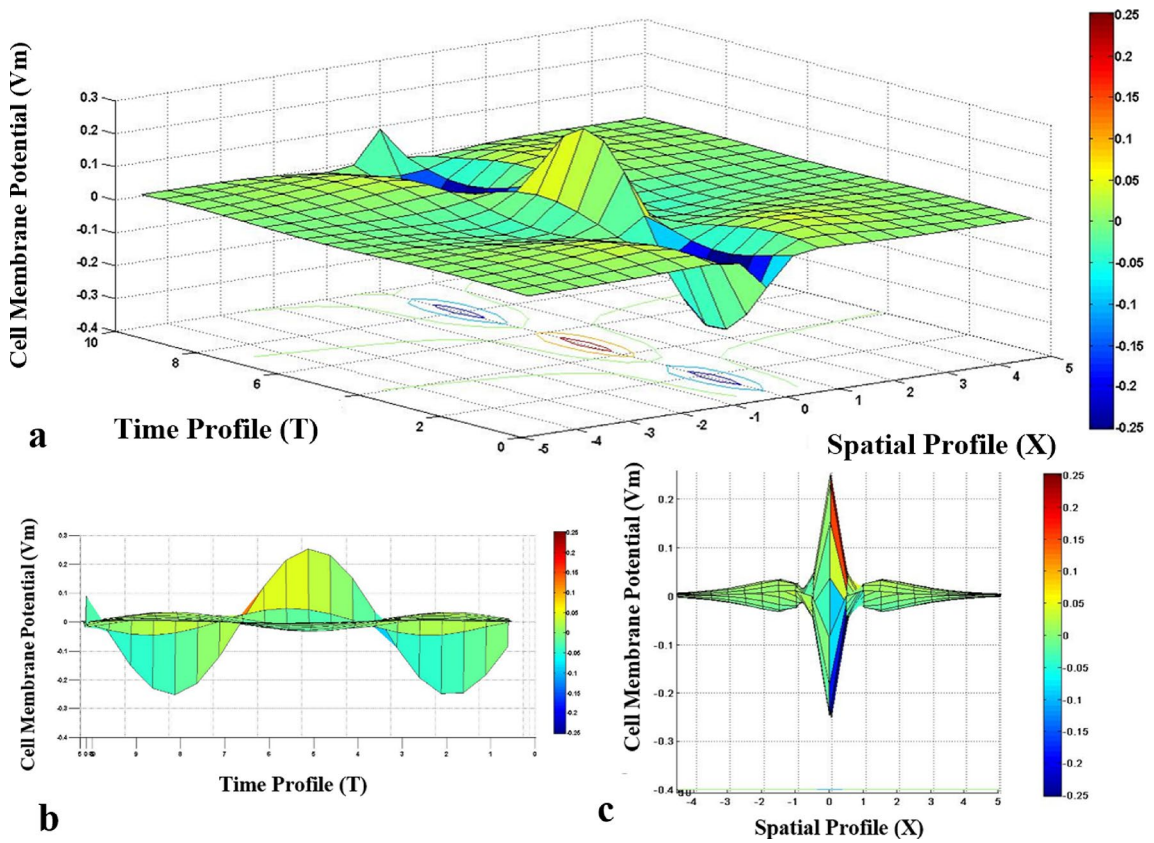


Fig. 7. Case I. All essential parameters equal to unity, (a–c) cell-membrane potential (V_m) with respect to spatial (X) and time (T) profiles.

This section of this paper is devoted to re-stress the importance of identifying all different phases of cellular potentials; for example, knowing the resting potential of cells, which typically ranges from -10 to -90 mV³⁹, is beneficial in identifying cell-membrane potential (V_m), and then linking V_m to a nature of a disease and/or to specific functionalities performed by a cell (cellular motility). The three different scenarios of the arbitrarily selected values of the controlling parameters, investigating the theory of cell-membrane potential, resulted in Figs. 7, 8, 9, 10, 11, 12, and 13 manifest that the term ν , describing the ratio of longitudinal resistance to current flow to intracellular resistance, cannot be held fixed if either μ or κ is changing due to the resistor coupling with these two terms. It has been found that by fixing μ and varying κ and ν (scenario II), κ and ν are inversely proportional; also, it is found that as the ratio of longitudinal resistance of cell membrane to its intracellular increases (κ increases), the cell-membrane potential amplitude increases. Furthermore, by fixing κ , and varying μ and ν (scenario III), μ and ν are appeared to be directly proportional; moreover, as the ratio of effective cell-membrane resistor, which is the sum of Warburg diffusion and cell-membrane resistors in series, to buffer medium resistance increases (μ increases), the cell-membrane potential amplitude increases. Therefore, measuring cell-membrane potential is affected by the resistivity of the medium in which it is placed; it is eventually reflected in its intracellular and extracellular potentials. Moreover, the amplitude of the cell-membrane potential is more pronounced at the external node, where the effective current is injected, and it is gradually depleting when moving away from the injected effective node along the spatial profile as depicted in sub-figures “c” of Figs. 7, 8, 9, 10, 11, 12, and 13.

Mathematical modeling has shown that the contributed factor of Warburg diffusion impedance is essential in shaping the overall cell-membrane potential, just as it has been justified experimentally in². Furthermore, the presented model could have been extended to encounter injection of currents at various locations within a cell membrane, either simultaneously or consecutively. To the authors' best knowledge, there has not yet been a legitimate justification that would give a specific pore on a cell of a size ranging from 7 to 10 Å (10^{-10} m) as indicated in¹¹⁹, to specifically open or close (flux/efflux) with respect to a distinctive nutrient, e.g., sodium (Na^+) and not to other nutrient types (i.e., Mg^{2+} , Ca^{2+} , etc.), yet another pore on the same cell would have specificity for opening and closing for, e.g., chlorine (Cl^-) anion. Such biophysics phenomena could be interpreted, mathematically, as a conditional current passing through an array of logic switches on the exterior of the cell membrane (combination of logical gate arguments), which also can ignite a switch of a gap junction of a cell-cell communication on global mathematical modeling of a cluster of cells.

In nature, the moving of ions/charges within a cell membrane is not ideally in a straight line parallel to the generated electric field; instead, it could take a curved infinitesimal path within a cell membrane as a generalized form; this is mathematically depicted in the proposed model by the integral and cosine term; this is again in

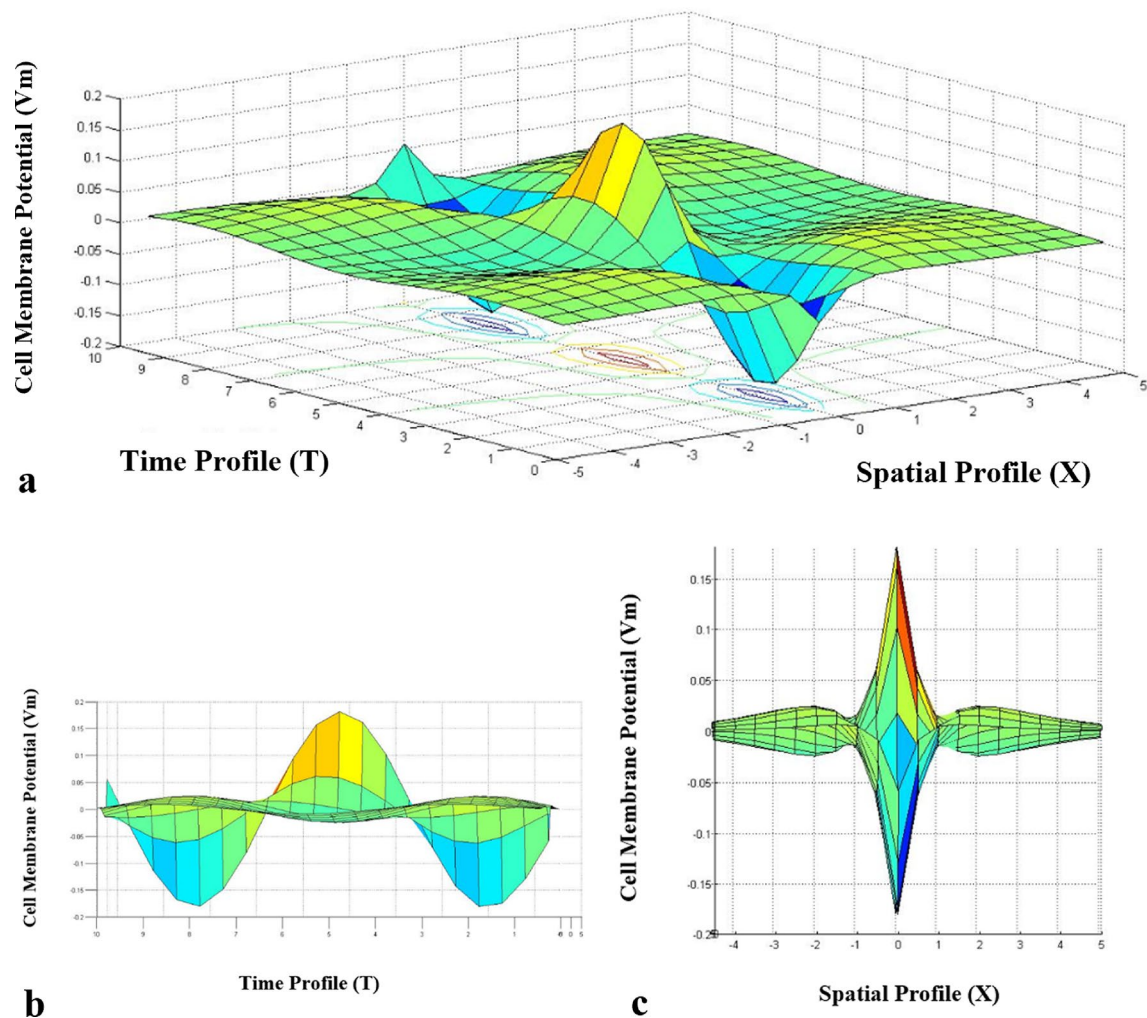


Fig. 8. Case II. ($\kappa = 0.25$, $v = 2\sqrt{2}$, μ is fixed), (a–c) cell-membrane potential (V_m) with respect to spatial (X) and time (T) profiles.

a great harmony of the biological kinematics of ions within the cellular domain described earlier by the term ‘diffusion.’ stochastic movements of ion molecules from high to low concentration.

The mathematically implicit effective cell-membrane capacitive factor, the sum of paralleled capacitors (Warburg and cell membrane), plays a dominant role in shaping the overall cell-membrane potential despite its explicit absence from the finally obtained expression. Similarly, the slope of the “c” subfigures of Figs. 7, 8, 9, 10, 11, 12, and 13 gives energy (work required) to transfer charges between the two domains segregated by the cell membrane—a lipid bilayer that significantly impedes the kinematics of one-way movement of charged ions.

The contribution flourished in this section, by encountering the Warburg diffusion impedance factor in the constructed analogical circuit of cellular biophysics, arrives at the definition of the effective cell-membrane signature. Such diffusion impedance accounts for a charge leakage that could be physically interpreted, e.g., as a charge leakage of nutrients via cells’ pores.

The three drawn scenarios: (1) fixation of the ratio of effective cell-membrane potential (the sum of the serial resistors consisting of the cell membrane and Warburg diffusion) to physiological medium resistance, which defines μ , and then varying κ and v ; (2) fixation of the ratio of longitudinal resistance of current flow to longitudinal internal resistance of the cell cytoplasm, which defines κ , and then varying μ and v ; and finally (3) equating all independent generalized parameters/resistors (i.e., r_i , r_o , r_m , r_w , and r_e) to unity, all yield the same cyclic configuration pattern of cell-membrane potential profile against time and space.

Considering that living cell-membrane potential in nature starts at a negative cytoplasm (negative resting potential) in a stage of polarization, resting potential is an invariant time potential at which ionic equilibrium is maintained, and electrochemical kinetics driving the ion kinematics are balanced³⁹. Then, upon stimulation, the cell membrane starts to polarize from negative; this is denoted as stage (I), moving to a swift depolarization stage (stage II: negative to positive), then to repolarization stage towards resting potential (stage III: positive to negative), and finally more negative passing resting potential in a stage denoted as hyperpolarization (stage IV). After stage (IV) has elapsed and re-initialization of stage (I) recommenced, such period is termed in biophysics as a refractory period; this entire process goes into a cycle along the cell membrane, where specific

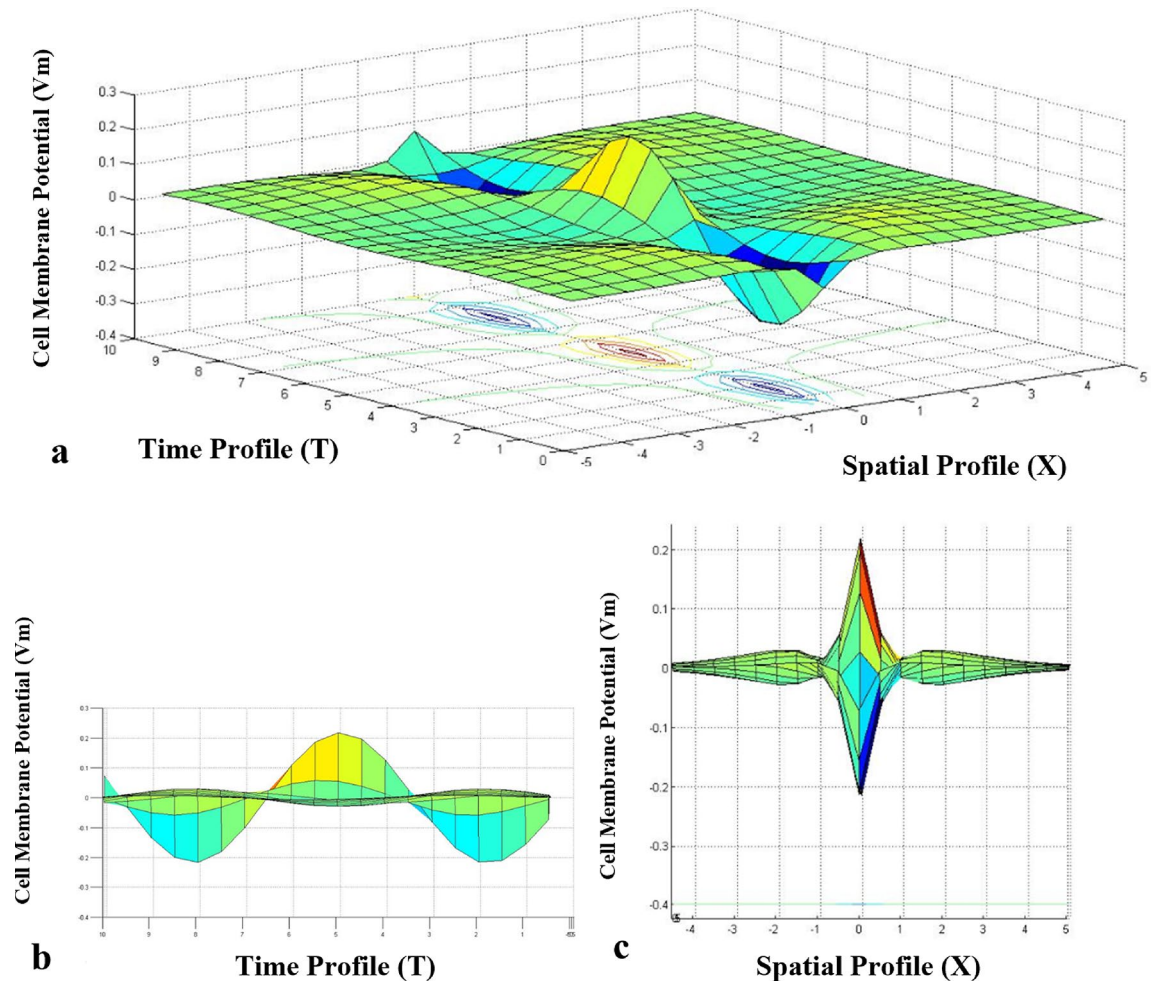


Fig. 9. Case II. ($\kappa = 0.5$, $v = 2$, μ is fixed), (a–c) cell-membrane potential (V_m) with respect to spatial (X) and time (T) profiles.

types of ion channels are open and close in an orchestrated manner, led by an electrochemical signaling maestro, producing a prominent pattern of hyper/depolarization. Such patterns of the constant initiations of signal peaks (action potentials) are representations of excitable cells. Thus, the obtained numerical findings (Fig. 14) are in agreement with the physical cellular potential going into cycle events of polarization, depolarization, and hyperpolarization^{39,43,45,47–49,130}.

It should be re-emphasized that the values set for the controlling parameters are arbitrary and only utilized to investigate the theory of cell-membrane potential and study the dependency of the controlling parameters of the illustrated analogical circuit of the living cell on each other: shaping the overall electrophysiology of a cell. To closely examine the various stages that cell potential goes through, Fig. 13b has been enlarged into the above figure (Fig. 14), illustrating the different phases of cellular potential.

The cyclic analog wave signaling of cell-membrane potential, as shown in Figs. 7, 8, 9, 10, 11, 12, and 13, justify the polarity of cells; imagine a cell, close to a spherical shape, contracts and extracts due to ‘firing/overshooting’ of action potential (depolarization), the opening of the voltage-gated channel, and undershooting (hyperpolarization), closure of the certain voltage-gated channel. If an initial stimulation takes place when the cell is at a resting potential (time-invariant potential) of -0.15 V, as depicted in Fig. 14, then the cell for some short period of time (about 0.7 – 1.6 T) shall maintain a minor increase in its negativity (negative cytoplasm) that could be attributable to either an increase or decrease in outward or inward current flow from of the cell, respectively.

At around 1.7 T, the cell starts to depolarize by having a few numbers of either Na^+ or Ca^{2+} channels open, where the respective cations start to flow into the intercellular domain. The stimulation reaches a threshold value, where the cell-membrane potential steeply increases in a depolarization stage of either increase or decrease of inward or outward current flow from the cell, respectively, suggesting an increase in the number of influx cations of Na^+ and/or Ca^{2+} into the intracellular domain. The cell membrane reaches a peak at 5.2 T of an action potential of 0.35 V, which is also the equilibrium potential, e.g., of Na^+ . At this stage, the cation of K^+ starts to repel against the similarly charged cation of, e.g., Na^+ , occupying the K^+ initial territory within the intracellular domain. The cytoplasm starts to gradually lose its positivity in a repolarization process by gradually opening

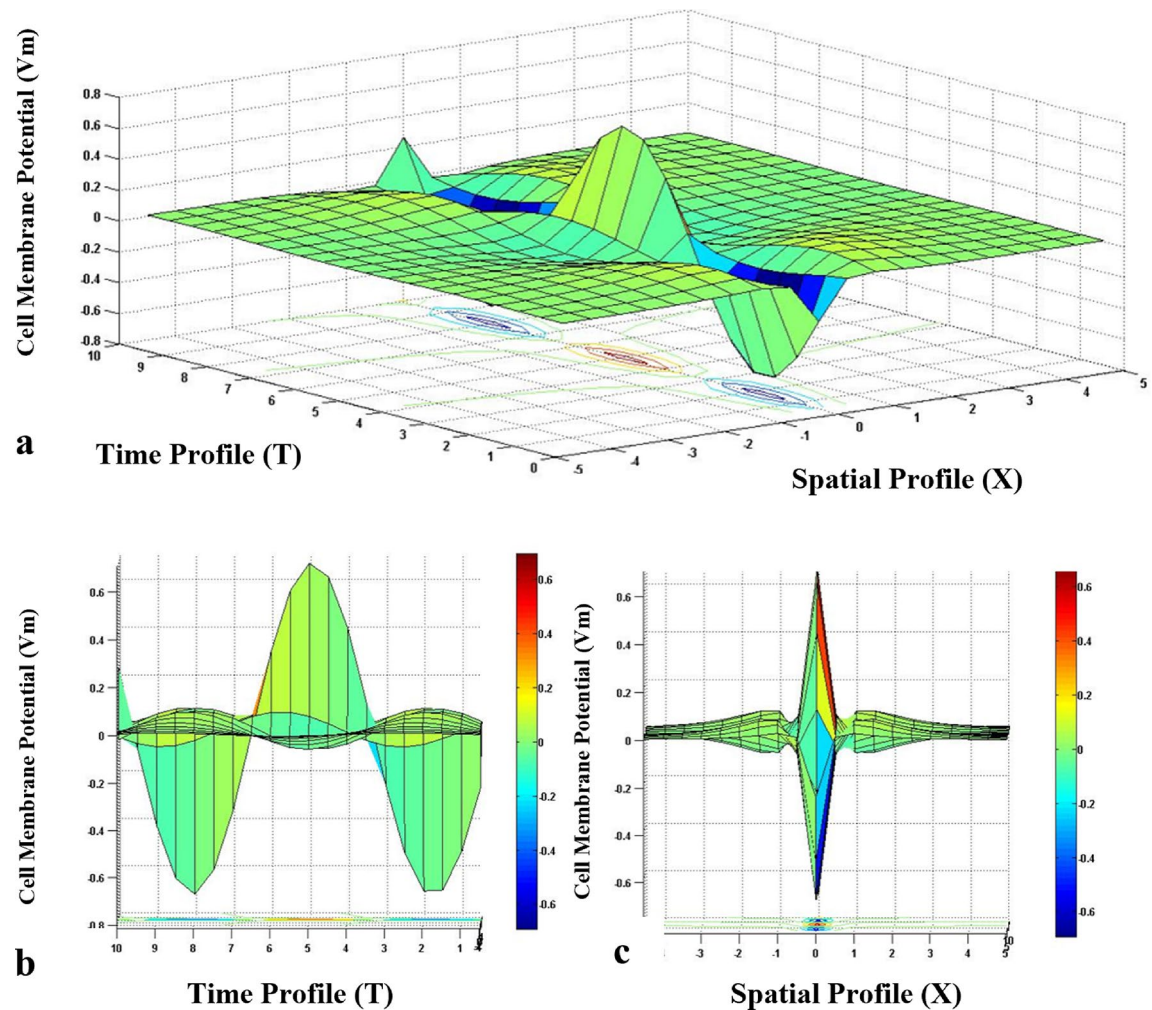


Fig. 10. Case II. ($\kappa = 2$, $v = \sqrt{6}$, μ is fixed), (a–c) cell-membrane potential (V_m) with respect to spatial (X) and time (T) profiles.

K^+ ion channels, permitting the efflux of K^+ cations out of the cell. This is followed by hyperpolarization, which passes the cell's initial resting potential as the cytoplasm's negativity increases. The hyperpolarization stage could be attributable to an increase in the number of voltage-gated channels, e.g., of K^+ and/or Cl^- , allowing either efflux or influx of K^+ cations or Cl^- anions, out and in the cell, respectively. Finally, the ionic ATP pumps restore the initial concentrations of K^+ and Na^+ , where the cell membrane goes back to resting potential before starting a new cycle. As a summary and for better illustration, the diffusion of K^+ and Na^+ are animated and depicted in Table 6a, which summarizes the different phases of cellular potentials in terms of resting potential polarization, action potential depolarization, equilibrium potential repolarization, and resting potential hyperpolarization.

The detailed analytical approach, which is flourished in this section, relates polarization/hyperpolarization and depolarization to various cellular activities and the nature of a disease. For example, it has been mostly found that cell mitosis (rapid division proliferation) is linked to depolarization, yet in seldom cases, mitosis takes place during polarization and hyperpolarization³⁹. This is evident in cancer cells where the cell-membrane potential is highly depolarized (low polarized characteristic); on the other hand, polarized/hyperpolarized cell-membrane potential cells, such as somatic cells, which are the building cells of an organism, are quiescent and don't undergo mitosis. Yet, their malignant types are depolarized¹³⁵. Remarkably, it has also been observed that in the case of quiescent somatic cells, the cells' mutation cycle from 'G1' to DNA synthesis 'S' phase is not possible due to the highly polarized nature of cell-membrane potential of these cells¹³⁵. It is concluded that hyperpolarized (excess of cytoplasm negativity of a cell) and depolarized (excess of cytoplasm positivity of a cell) cell-membrane potential are respectively associated with non-proliferated and cancerous cells, in which depolarization is linked to increasing activities of Na^+ ion channels^{43,45,47–49,130,136}.

Another interesting phenomenon that emerged after comprehending the controlling parameters of the electrochemical characteristics of cells is the ability of certain cells to transform from a non-proliferating phase to a proliferating one and vice versa, such as that experienced during inflammation, injury, or restoration of skin in response to a specific electrochemical or environmental signal; among those is the vascular smooth muscle cells (VSMCs)³⁹. This is also evident in the motilities of fibroblasts to a wounded area to perform restoration^{137–139};

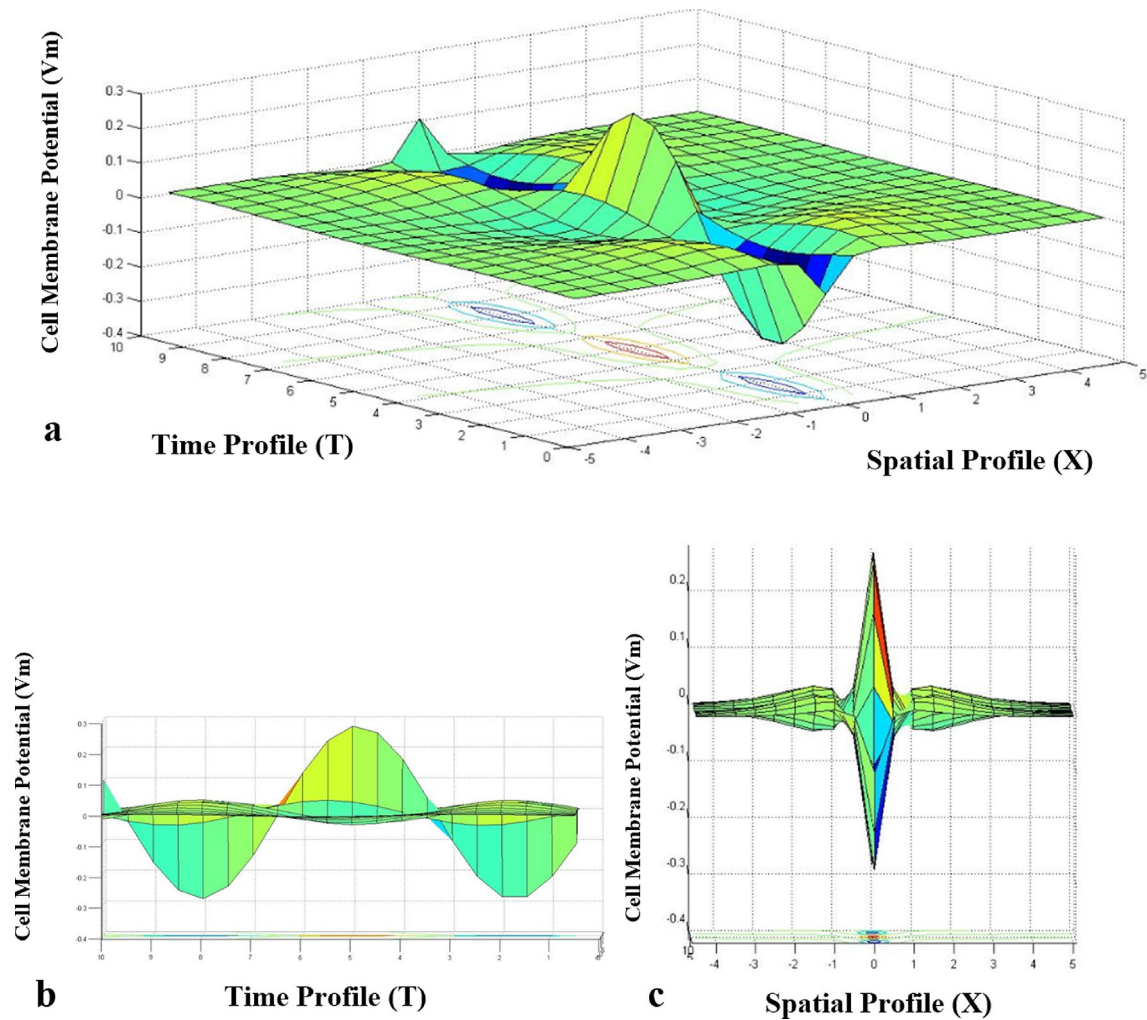


Fig. 11. Case III. ($\mu = 3$, $v = \sqrt{3}$, κ is fixed), (a–c) cell-membrane potential (V_m) with respect to spatial (X) and time (T) profiles.

this is depicted in Table 6b¹¹⁹. Fibroblasts, mesenchymal cells, depict electrochemical signaling in the event of tissue wounding and production of extracellular matrix, upon which such cellular biophysics promotes fibroblast cells' motility, exerting contractile force during cells' movements^{120,121}. As in cancer cell's motility depicted in Fig. 3, fibroblasts' motility is initiated by actin polymerization at the cell's leading edge, constructing protrusive lamellipodia and filopodia, accompanied by detachment of the actin filaments at the trailing edge of the cell¹³⁷.

Another example of the dominant role that cellular electrochemical activities play in stimulating the mechanobiology of cell's movements can be clearly witnessed by a microscopic video taken from a 16-mm movie made by Dr. David Elliot Rogers at Vanderbilt University in the 1950s¹⁴⁰. This video presentation, provided in Table 6c, highlights the importance of (1) distinctive electrophysiological characteristics of each cell type, (2) cell-cell communication, and (3) the dominant role that cellular biophysics plays in stimulating cell's motility (cellular mechanobiology). A neutrophil (a type of white blood cell of the immune system produced by hematopoiesis in the bone marrow), of distinctive biophysics, and upon its release into the peripheral blood and circulates for 8–10 h before migrating into the tissue, with a life span of only a few days, it exhibits a cell-to-cell communication with a *Staphylococcus aureus* (a type of bacteria) that releases chemoattractants (distinctive electrochemical signaling picked up by the immune cell receptor); this provokes cell's motility mechanism of the neutrophil that commences chasing (crawling) mechanism towards the targeted bacterium via a field of red blood cells within a blood smear. The bouncing bacterium around red blood cells, due to thermal energy, is finally captured and engulfed by the neutrophil in a process known as Phagocytosis¹⁴¹. Zhu et al.¹⁴² studied fibroblast migration and allocated a novel research avenue in wound healing therapy. They concluded their analyses by amplifying the dominant role of cellular electrochemical signaling in stimulating the fibroblast's motility. Their findings concluded that human fibroblast motility results from a new bFGF-regulating mechanism, which orchestrates Smo and Gli regulators within Hedgehog (Hh) signaling in fibroblast motility. Specifically, they determined that Smo regulates β -catenin nuclear translocation via activation PI3K/JNK/GSK3 β , whereas β -catenin positively stimulates fibroblast cell migration and the expression of Hh signaling genes, including Smo and Gli¹⁴².

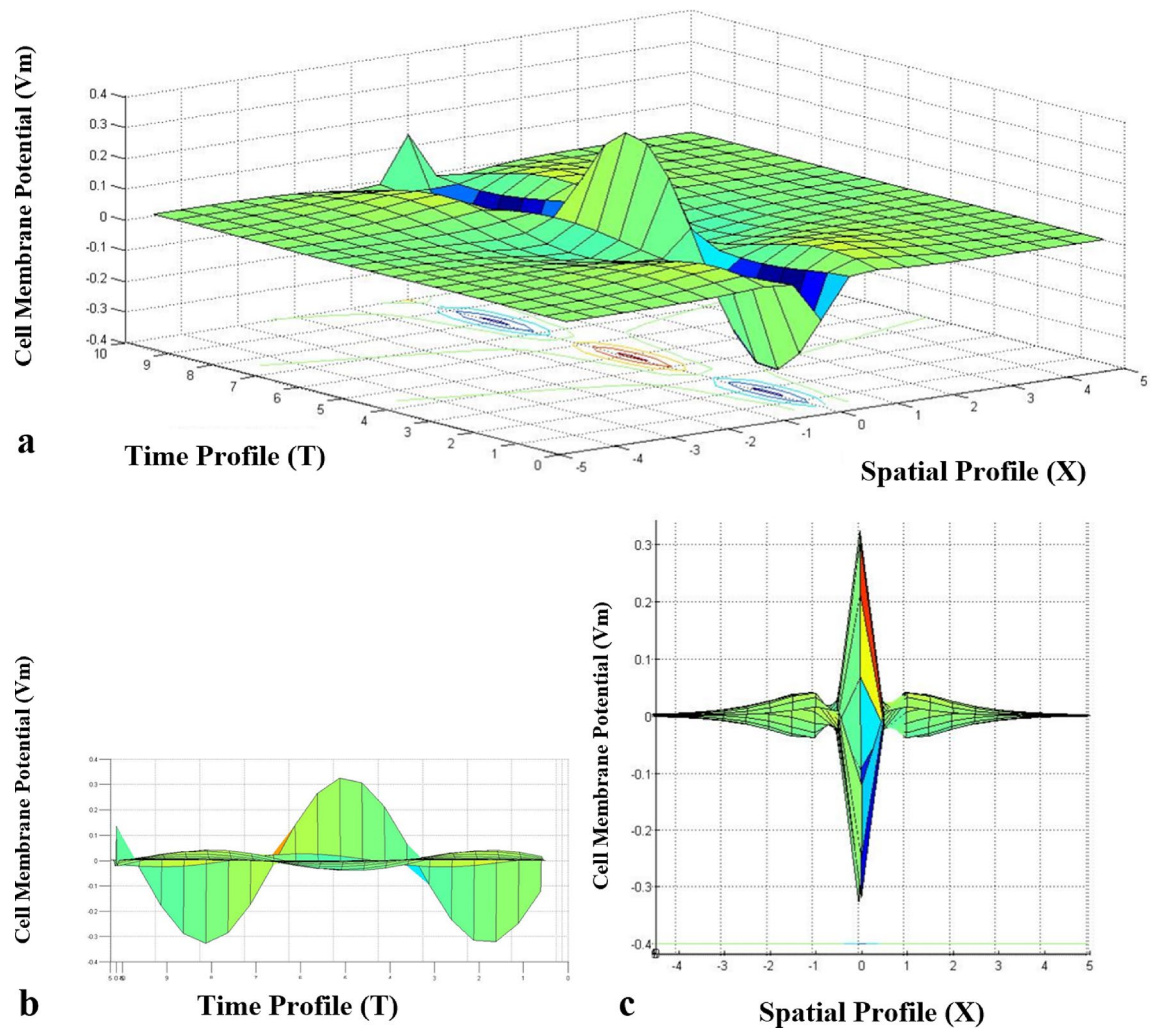


Fig. 12. Case III. ($\mu = 6$, $v = \sqrt{6}$, κ is fixed), (a–c) cell-membrane potential (V_m) with respect to spatial (X) and time (T) profiles.

This work, within this section, assists researchers in sensor technology, molecular biophysics, analytical chemistry, biotechnologists, and biologists in investigating the response of a cell subjected to an injected current. The ability to unlock the coding of electrochemical language/signaling of cells could be beneficial in allocating a novel approach in directing cells, including stem cells, toward performing a specific task, pretreating cancerous cells to be healthy ones, effectively delivering medicine by up/down-regulating the performance of specific ion channels, and finally repairing disrupted genes, e.g., PTEN, TSGp53, that are respectively responsible for Autism¹⁴³, and the dual role of p53 in Parkinson's and cancer diseases¹⁴⁴. Furthermore, the electrochemical approach could provide a novel technique for identifying the different phenotypes of stem cells, which are hard to segregate by using a fluorescence-activated cell sorting (FACS) machine, arriving at their heterogeneity, manipulating them, and finally analyzing their subpopulation dependencies and their interconnections with their niche.

This section also provides in-depth analyses of the biophysics of cells and their equivalent analogical electric circuits that capture cellular electrophysiology. Furthermore, the outcome of this analytical study is to investigate the potential spatial and temporal dependence of cell membranes when stimulated by a current. This analytical approach simulates, to some extent, an experimental case where a cell is trapped in a buffered medium and then stimulated by an electrode, and another adjacent electrode finally records cell-membrane potential; this will be the target subject of Section “Materials and methods” that addresses the electrochemical profiling of cell membrane of well-established melanoma cell-line models, which to the authors’ best knowledge, such characteristics have not been yet extracted experimentally in distinguishing the different stages of the melanogenesis.

Miniaturized-versatile-biomechatronic platform: quantifying the cell-membrane potential

The findings of the previous sections are aggregated and embodied in the design of a robust biomechatronic platform that captures the electrophysiology of cells and thus identifies melanogenesis. The biology of cancer

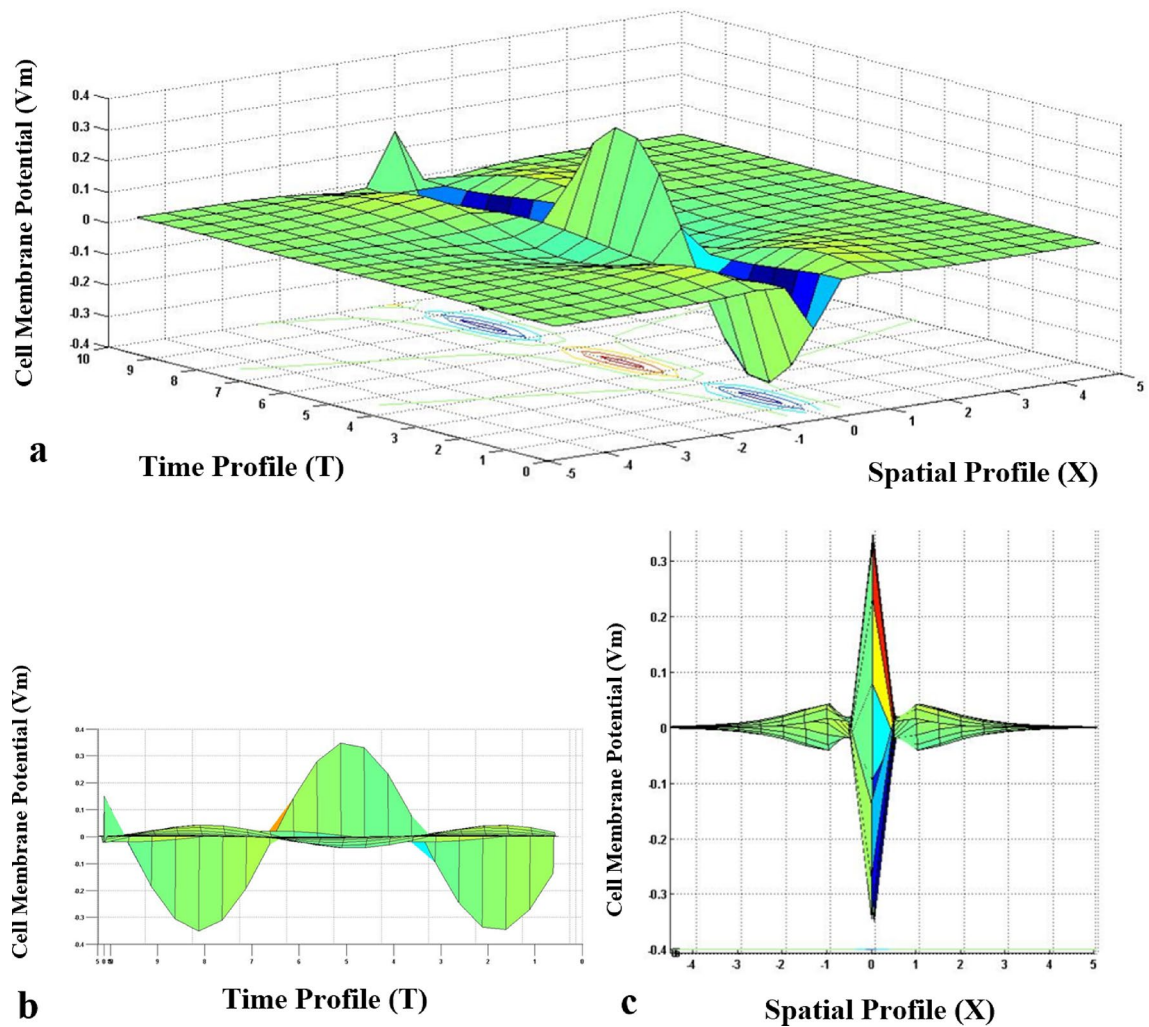


Fig. 13. Case III. ($\mu = 9$, $v = 3$, κ is fixed), (a–c) cell-membrane potential (V_m) with respect to spatial (X) and time (T) profiles.

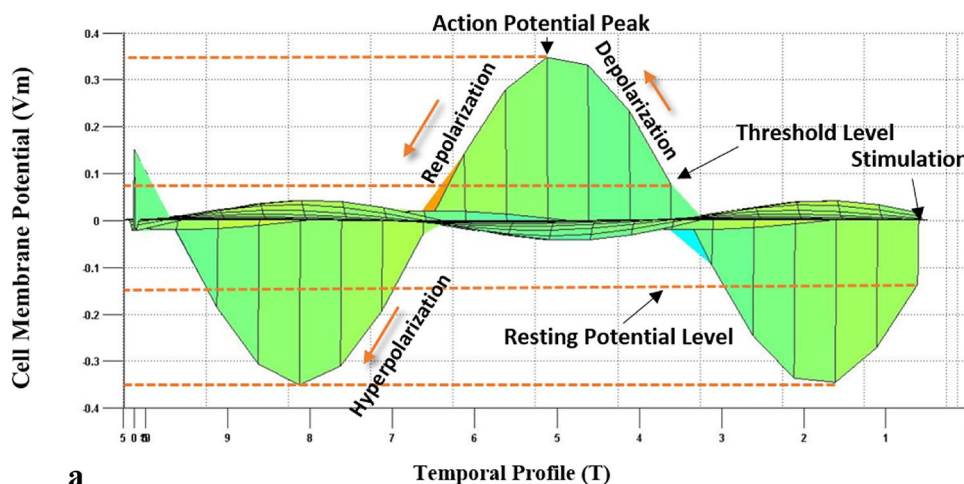


Fig. 14. Numerical result of cell-membrane potential (V_m) versus temporal profile (T) based on non-ideal/arbitrarily selected parameters ($\mu = 9$, $v = 3$, κ is fixed) due to a lack of experimental findings of intracellular and extracellular resistive values to illustrate the different phases of cellular potentials: polarization, depolarization, repolarization, and hyperpolarization.

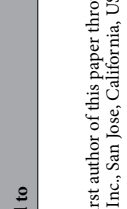
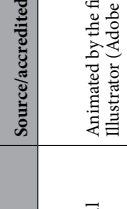
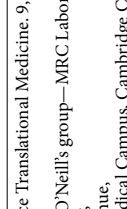
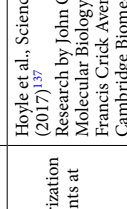
No.	Sneak preview	QR code to the movie presentation	Brief description	Source/accredited to
a		 	This is an animated movie presentation depicting different phases of cellular electrochemical characteristics: resting potential polarization, action potential depolarization, equilibrium potential repolarization, and resting potential hyperpolarization.	Animated by the first author of this paper through Adobe Illustrator (Adobe Inc., San Jose, California, USA)
b		 	Motilities of fibroblasts, mesenchymal cells, to wounded area to perform tissue restoration via the initiation of actin polymerization at the cell's leading edge, constructing protrusive lamellipodia and filopodia, accompanied by detachment of the actin filaments at the trailing edge of the cell	Hoyle et al., Science Translational Medicine, 9, eaal2774 (2017) ¹³⁷ Research by John O'Neill's group—MRC Laboratory of Molecular Biology, Francis Crick Avenue, Cambridge Biomedical Campus, Cambridge CB2 0QH, UK
c		 	A neutrophil chasing (crawling towards) a <i>Staphylococcus aureus</i> through a field of red blood cells within a blood smear. The bouncing bacterium around red blood cells due to thermal energy is finally captured and engulfed by the neutrophil in a process known as Phagocytosis ^{141,142}	Dr. David Elliott Rogers (MD) ¹⁴⁰ , the estate of David Rogers, Vanderbilt University. This classical microscopic video was extracted from a 16-mm movie made at Vanderbilt University in the 1950s

Table 6. Movie presentations manifesting the prevalent role of the electrochemical (biophysics) of cells in stimulating cell migrations (motilities).

and cellular viability requirements, together with computational fluid dynamics (CFD) and finite element method (FEM) analyses that fairly discussed in Alqabandi¹⁴⁵, as well as understanding the biophysics of cells, would all contribute to further developing and reaching an optimal design of experiment (DOE) of the proposed biomechatronic platform flourished in this section. Accordingly, a microfluidic (μ F) domain is integrated with multi-electrode arrays (MEAs) to form an integrated lab on a chip (iLoC). The proposed iLoC, together with the customized microelectronics and dedicated controlling software, provide a hybrid biomechatronic structure that would extract cellular biophysics and, hence, identify the different stages of the disease. Upper and lower multi-electrode arrays are integrated within the microfluidic system to stimulate and faithfully record the cell-membrane potential of each melanoma cell-line model. The objectives are to have a biocompatible and robust system that would preserve the cell's integrity throughout a sufficient number of in vitro experiments and attain repeatability in the obtained readings.

Microfabrication of the mechanical structure

As presented in Alqabandi¹⁴⁵, detailed empirical analyses have been performed in COMSOL Multiphysics 4.2a (Burlington, MA, USA) prior to microfabrication to visualize the flow pattern and arrive at a sensible flow speed that would ease the process of flushing the μ F system in a controlled applied pressure manner: achieving repeatable and durable usages of the proposed system. Furthermore, such empirical analyses assist in attaining an optimal pitch distance between two adjacent electrodes (stimulating and recording), upon which uniform current distribution is maintained.

In light of the cells' physical characteristics, which are fairly discussed in sections “[Cancer biology overview](#)” and “[Cancer electrophysiology](#)”, the microfluidic channels are characterized to accommodate the size of living cells, avoid clogging, and allow system maintenance. The proposed miniaturized mechanical structure consists of a μ F domain sandwiched between upper and lower glass substrates; gold (Au) MEAs are patterned on the glass substrates, as depicted in Fig. 15.

The materials for the μ F domain have been chosen to serve three criteria: ease of machinability, biocompatibility, and high dielectric resistivity (acting as an insulator). Such characteristics are found in the AZ-related family of polymers that are widely used in biological applications¹⁴⁶. Thus, AZ EXP 125nXT photoresist material is a negative working-photoresist-polymer binder utilized in the proposed μ F system.

The MEAs were patterned on two glass substrates that were 1 mm thick. The transparent glass substrate allowed an accessible view of cell manipulation and trapping under a microscope. First, Piranha cleaning was carried out on the glass substrates (3:1 = H_2SO_4 : H_2O_2) for 30 min. This was followed by optical photolithography to pattern the gold electrodes in a standard lift-off process. The glass substrates were coated with positive photoresist AZ 1518 (Microresist, Berlin, Germany) and spun at 3000 rpm (forming a layer of 1.8 μ m thick), followed by a prebake process on a hotplate for 1 min at 115 °C. A high-resolution exposure dose of 60 mJ, together with a patterned mask, was performed. The glass substrates were developed using a resist developer AZ 400 K 1:4 in a beaker for 6 min, where no post-bake process was carried out. The developed glass substrate was examined under the microscope to verify design specifications. Ar sputter metallization was performed, where an adhesive layer of 5 nm Ti and 300 nm of the functional layer of Au were sputtered/deposited on the AZ1518 resist structure. This was followed by a lift-off process using Dimethylsulfoxide (DMSO), performed at 80 °C for 4 h; the glass substrate was then cleaned using isopropyl alcohol (IPA) and acetone. Prior to deicing, ~ 2 μ m photoresist for backside protection was added. Diesaw was utilized to cut different MEAs on the glass substrates of 17 × 20 mm; the μ F channel area (a reddish component of Fig. 15) is 10 × 20 mm.

The AZ 125nXT-based μ F system (channels and reservoirs) was developed on top of the bottom glass substrate, as shown in Fig. 15, where the optical photolithography process was performed. The bottom glass substrate was coated with negative photoresist AZ 125nXT (Microresist, Berlin, Germany), forming a layer of 17 μ m. A soft-baked process on a hotplate at 140 °C for 8 min was carried out, followed by a hard-contact exposure dose of 6 J/cm². The microfluidic features were developed in 6 min using AZ MIF 814 with no post-baked process to be performed. The developed system was examined under the microscope for any microfabrication deficiencies in the developed process. Also, Dektak 3 was utilized to confirm that the developed channel depth (photoresist height) is within design specification: ~ 20 μ m.

Two 1-mm holes were drilled into the top glass substrate in line with inlet and outlet reservoirs, followed by a glass substrate cleaning process using IPA. The miniaturized mechanical structure of the two (upper and lower) glass substrates, together with the μ F domain, was bonded on a hot plate at 100 °C for 5 min. A microscope was utilized to confirm the alignment of the upper and lower electrode arrays and examine the MEAs' intersection with the microfluidic channels. The two connecting adaptors were adhered to the clean upper surface of the glass substrate via the UV adhesion method. Figure 16 depicts the final microfabricated μ F domain incorporated with the MEAs.

Microelectronics architecture

The continuous numerical analog cyclic signal propagations of cellular potential, obtained in Section “[Mathematical modeling of the electrophysiology of a living cell: analytical approach](#)”, initiate the need for an analog-to-digital converter (ADC) to arrive at the cell-membrane potential experimentally and eventually analyze the collected data. Therefore, the microelectronic architecture has been designed and constructed based on the essence of understanding cellular biophysics covered in the previous section. Furthermore, as per the microfabricated mechanical components of the overall biomechatronic platform, there are 11 pairs of electrodes (upper and lower); therefore, a 12-channel-ADC module (Microsystems Ltd., Varna, Bulgaria) has been constructed, where one module is a dummy (12th module). The ADC module is of a fully differential input type with a resolution of 24 bits. The maximum full-scale error is ± 0.01%, with the ability to generate maximum internal and external voltages up to ± 10 V and ± 100 V, respectively. Furthermore, the input common-mode

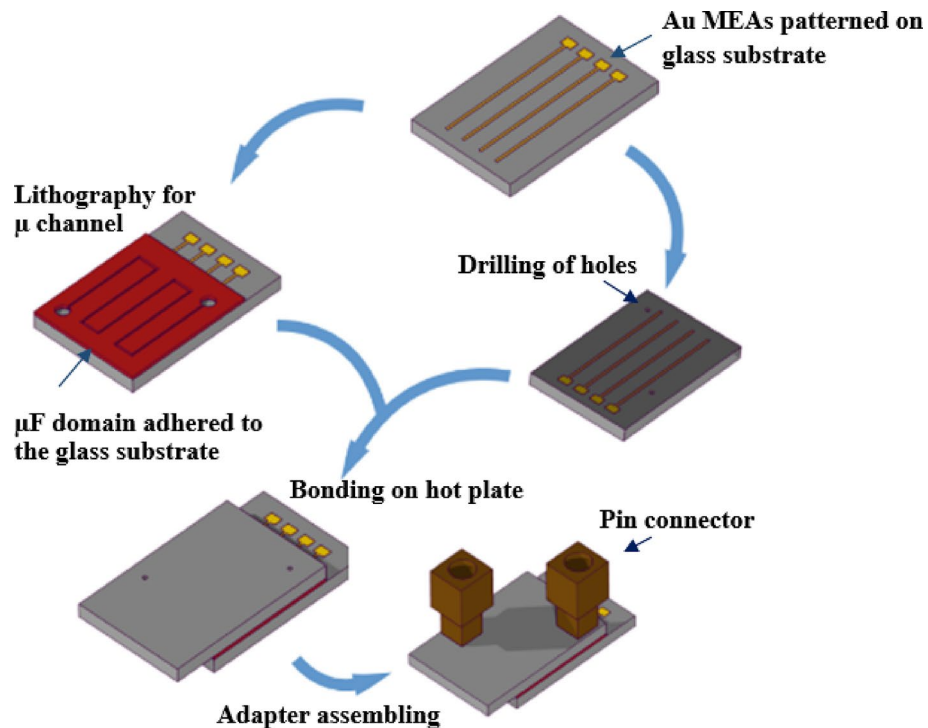


Fig. 15. 3D illustrations and assembling of the proposed μ -structure platform, consisting of two upper and lower glass substrates and a microfluidic domain. An array of gold electrodes is patterned on the glass substrates. The upper glass substrate is drilled at two locations in line with the two inlet and outlet reservoirs. The connecting pin adaptors adhere to the upper glass using UV adhesion. The 3 domains (μ F system and lower and upper MEA glass substrates) are thermally adhered on a hot plate.

voltage is ± 2 V, with an input impedance of 20 Mohm and a bias current of 30 pA. The ADC module has an 8-input range of potentials: ± 1 mV, ± 2 mV, ± 4 mV, ± 8 mV, ± 16 mV, ± 32 mV, ± 64 mV, and ± 128 mV. The selection of such input ranges shall be further justified in the next section. In addition, a biasing voltage can be applied to the electrodes, generating maximum internal and external voltages up to +10 V and +100 V, respectively. The ADC module allows for the reversal of biasing polarity, switching the role of stimulating and recording between the upper and lower electrodes. Hence, this is quite beneficial in extracting the cell-membrane potential of adhesive and non-adhesive cells, in which the former could be adhered to either the upper or lower electrode, whereas the latter is floating within the vicinity of either one. The ADC module is connected to a National Instrument multi-function data acquisition card (NI USB-6009, 14-Bit, 48 KS/s) via a customized DB M15 pin cable. A shield cover is dedicated to protecting the underlying circuitry (wires, pads, etc.) from any electromagnetic emissions.

An MS7212 multi-function process calibrator (MASTECH, Guangdong, China) is utilized to generate potential/current: charging electrodes; also, it acts as a multi-meter to investigate whether electrodes and other connections of the microsystem are faithfully transmitting signals. A BNC-pin cable interconnects the multifunction process calibrator with the 12-channel ADC module. A dedicated power supply module (Microsystems Ltd, Varna, Bulgaria) energizes the 12-channel-ADC platform. Figure 17 shows the microelectronics hardware architecture of the electrophysiology biomechatronic-based platform.

In order to capture the polarity of a living cell by recording the differential voltage between the upper and lower electrode, where the cell is trapped, a passive (no active components) transition printed circuit board (PCB) has been fabricated. Furthermore, a flexible cable is uniquely customized to connect the miniaturized electrophysiology-based biomechatronic platform with the transition board. The customized, flexible cable pads are soldered to the patterned gold electrodes on the glass substrate (upper and lower). The final connection is examined under the microscope, and the signal is checked through a multifunction multi-meter, as shown in Fig. 18.

The ADC module consists of four ADC blocks, each having 3 parallel channels, thus forming twelve parallel measurement channels. The 12th channel is a dummy since only 11 pairs of electrodes can be active when conducting the *in vitro* experiments. Figure 19 illustrates the electronic circuit schematic diagram of the injection/measurement principle of operation for the electrophysiology biomechatronic-based platform. One channel of the ADC is presented for illustration purposes only, and it applies to all channels. The schematic diagram of a multiplexer (MUX), which processes the multi-input signal to a single output, is not shown. The system works in two phases, switched by a microswitch control block driven by a digital circuit of 0/1 logical value. The microswitches A and B, in Fig. 19, work synchronously; it should be noted that there are two phases: a charging and measuring phase to the left and right of the miniaturized biomechatronic platform. The system

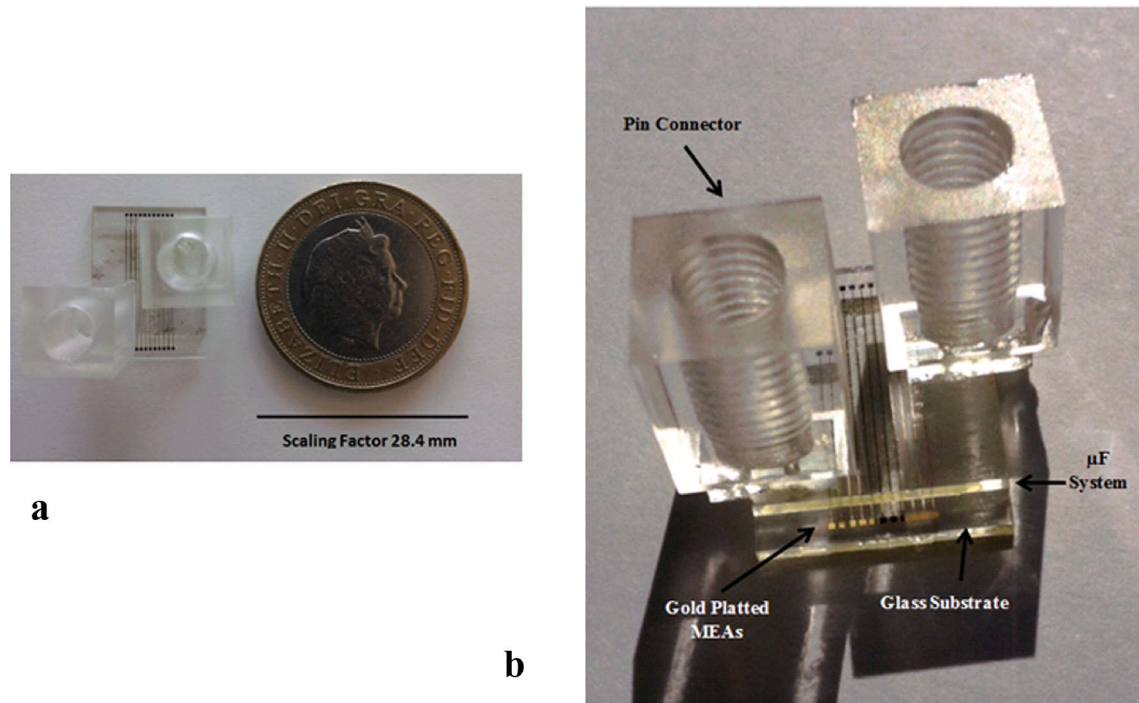


Fig. 16. Microfabricated μ F domain incorporated with MEAs. (a) A top view of the LoC module is placed next to a two-sterling British pound coin as a scaling factor. (b) An image showing connecting pins of culturing and outlet reservoir and gold-plated upper and lower MEAs patterned on two glass substrates (upper and lower), which are crossing the microfluidic channels.

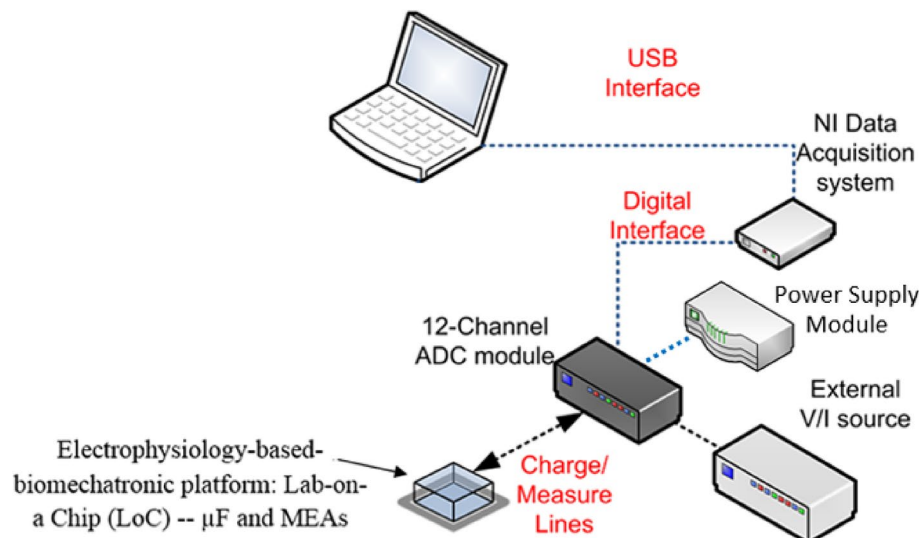


Fig. 17. Microelectronic hardware architecture of the electrophysiology-based biomechatronic platform connected to a 12-channel-ADC module through NI card and multifunction voltage/current generator. The system is connected to a PC to collect and analyse experimental data.

consists of two microswitches, A and B—taking either position '1' or '2'. Therefore, if the microswitches are at position '2' on both sides, this is considered the charging phase (potential injection mode) of the electrodes; alternatively, if the microswitches are at position '1' on both sides, this is considered the measuring potential phase, where the electrodes are disconnected from the voltage source. The high impedance-voltage amplifier is utilized to measure charges and prevent the microelectronic regime's discharging at a fast rate. The resistors bias the amplifier inputs to the ground if no signal is present. Finally, the polarity of the voltage source can be

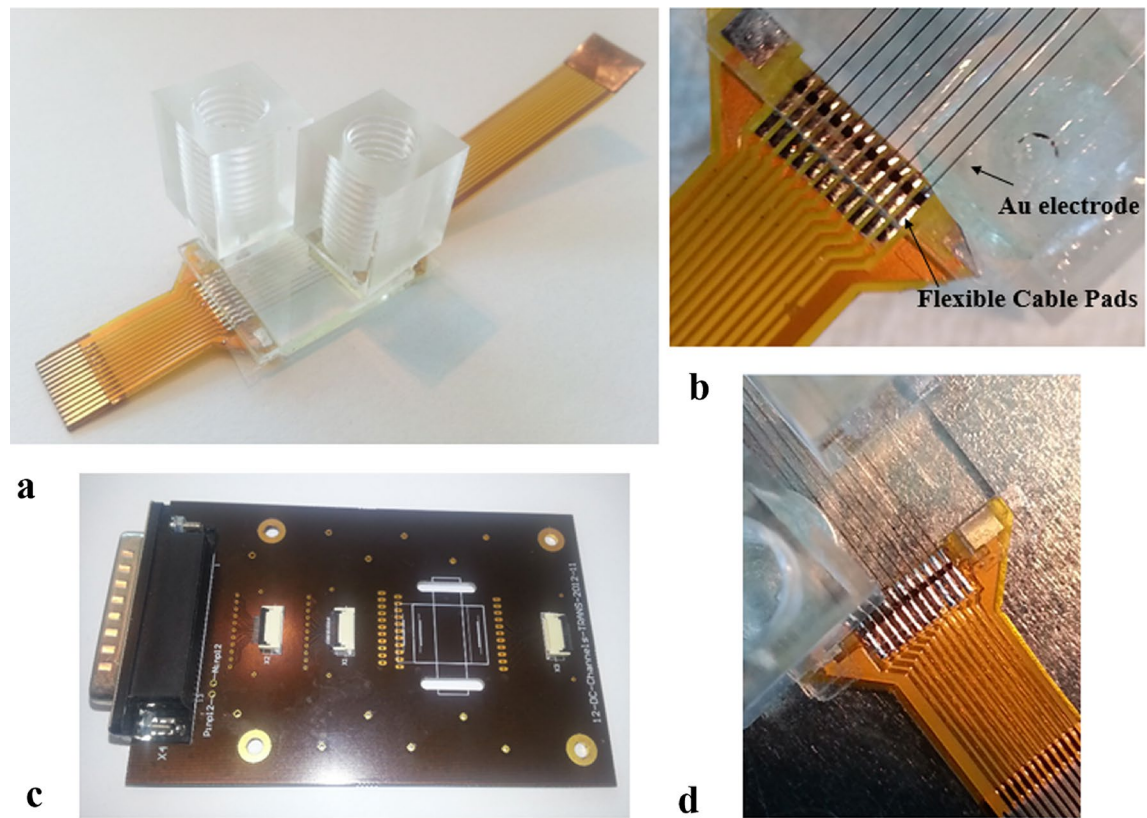


Fig. 18. Integrated lab on a chip (iLoC) consisting of a μ F domain incorporated with MEAs. (a) Assembled flexible cable to upper and lower multi-electrode arrays. (b) Soldering of bottom gold electrodes patterned on a glass substrate to flexible electrode pads. (c) Transition-printed-circuit board (PCB) showing passive components: input connector pinout, pins and cables. (d) Soldering upper gold electrodes, patterned on a glass substrate, to flexible cable pads.

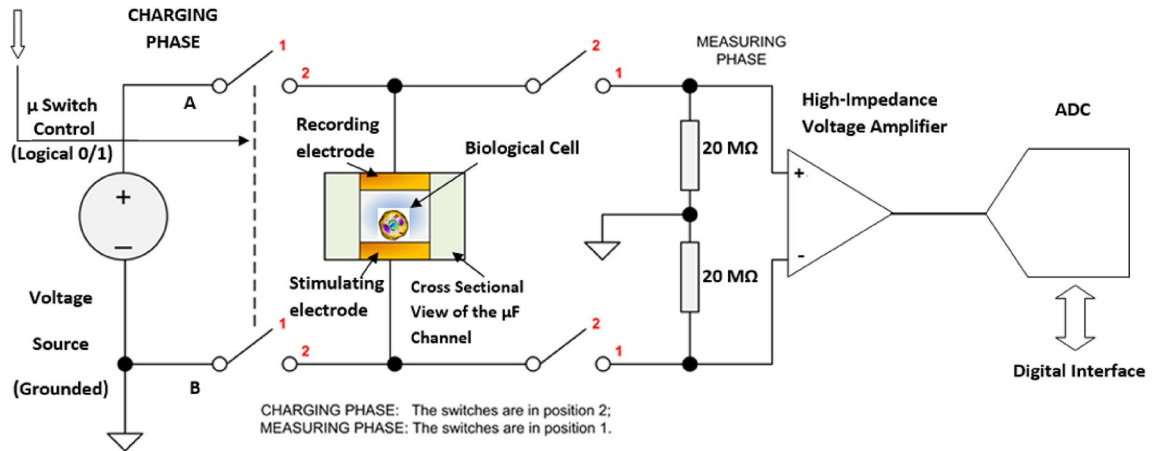


Fig. 19. Schematic diagram illustrating the working principle of the electrophysiology biomechatronic platform of one channel of an ADC. Positions 1 and 2, respectively, show the measuring and charging regime of the microelectronic characteristics of the platform. A cross-sectional view of the μ F system with a living cell entrapped between upper and lower electrodes is illustrated.

reversed, giving the flexibility of reversing the role of the upper and lower electrodes to either record or stimulate (inject) electrodes and vice versa.

The electrochemical bio-mechatronic platform operating software

The controlling software of the electrophysiology biomechatronic platform has been coded in the DELPHI application programming language, and it operates under the Microsoft Windows platform. This program has been customized to serve the experimental needs of the miniaturized electrochemical bio-mechatronic device (Fig. 20). Furthermore, the pre-set controlling parameters are in line with the reviewed literature in terms of biophysics of cells based on the various scholars' findings in the field of cellular electrophysiology that were presented in Section “[Cancer electrophysiology](#)” of this paper.

This DOE-oriented program operates with up to 12 channels; only 11 are used in the current setup. This allows data collection from various pairs of 11 electrodes: stimulating and recording electrodes. Thus, this shall enable the extraction of cells' electrophysiology and conduction of further biophysics analysis.

The hardware system consists of a 12-channel-analog-to-digital-converter (ADC) module to account for the 11 pairs of electrodes (upper and lower electrodes) embedded within the microfluidic domain. The objective is to capture the polarity of a cell and extract the cell-membrane potential. The ADC converters are slow and precise. The maximal update rate for collecting data from all 11 channels is 5 updates per second. Each ADC hardware component has 3 channels; hence, there are 4 ADCs to accommodate the 11 pairs of electrodes, leaving channel 12 as a dummy one.

The user starts by charging the electrodes via an internal or external source. The former charge–voltage approach takes up to ± 10 V as a maximum charge, whereas the latter approach takes up to ± 100 V. It should be noted that when internal charging is in active mode within the biomechatronic system, there is an internal amplifier gain of 2 within the ADC module. Hence, the maximum voltage generator connected to the 12-channel-ADC module shouldn't exceed 5 V; the internal generation of voltage doubles the potential, and that is attributable to the usage of a power operational amplifier (OPAM). The OPAM is utilized to enhance system performance in case of a lack of a high-voltage source to be fed to the electrodes. As for the external charging, the upper and lower electrodes can be both charged, or one is charged, and the other is grounded. The charging starts once the user clicks the “Charge on” command.

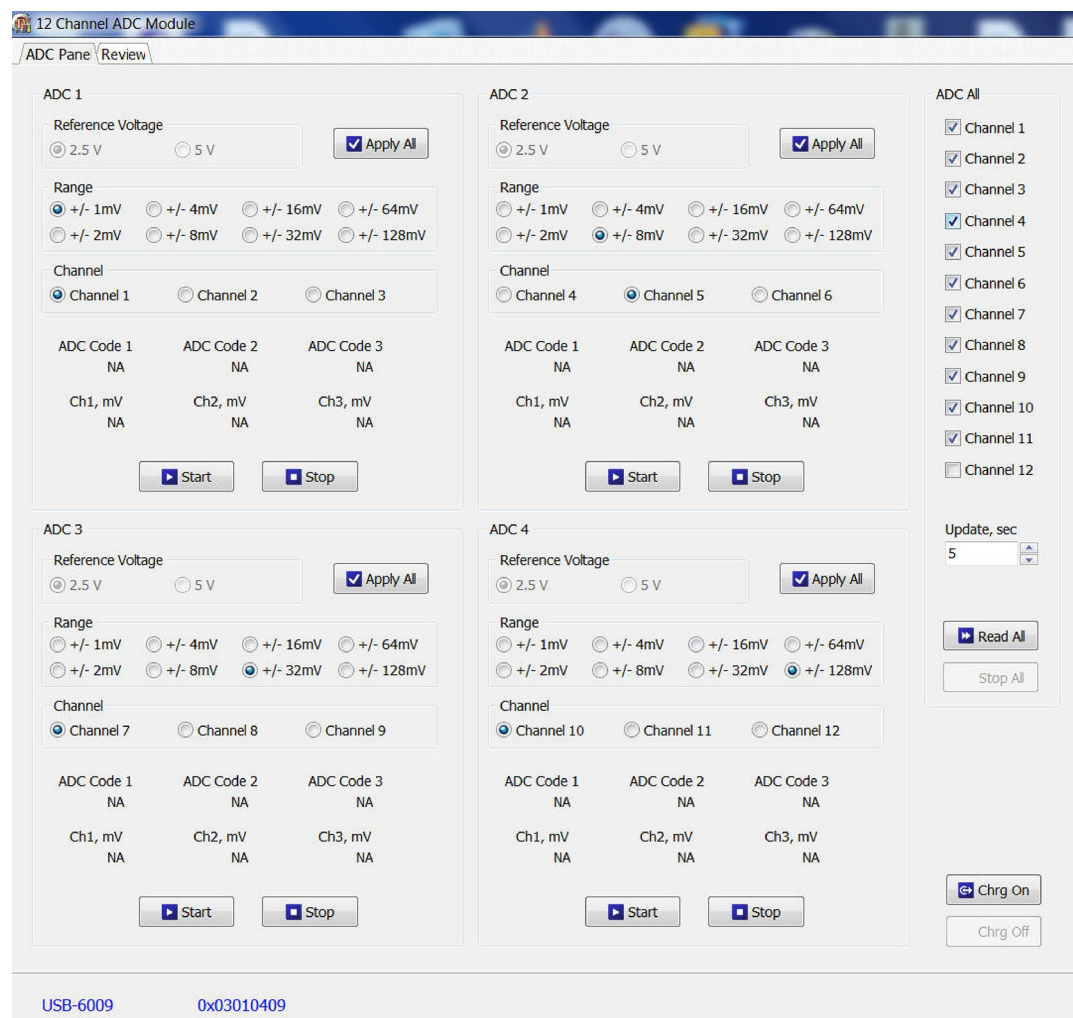


Fig. 20. Customized electrochemical biomechatronic platform operating software control panel.

Each ADC, by default, has a fixed reference voltage to ensure its operation. Furthermore, each ADC is on one circuit, and its associated 3 channels must all have one value of voltage difference range. The ADC microelectronics measure the differential voltage between the upper and lower electrodes. For example, if a voltage range is selected to be $+/- 4$ mV, then voltage measurements between -4 mV and $+4$ mV are possible. All voltages exceeding $+4$ mV will cause ADC saturation, i.e., the program will show the upper limit of the range as 4 mV. Respectively, all voltages below -4 mV will cause the program to show the lower limit as -4 mV. Thus, the user can recognize the saturation by the obtained readings; if all obtained readings are constantly $+4$ mV or constantly -4 mV, then the chosen range is too small, so it must be increased.

The detection regime range of voltages is in line with the potential of cell-membrane findings within the published literature^{40–43,45–47}, illustrated in Section “Cancer electrophysiology”. Each channel corresponds to a pair of electrodes: bottom and upper. The developed software provides flexibility in terms of assigning the same detection range value to all ADCs’ channels by a single click on the “Apply All” button, or it allows users to perform different experiments by assigning different detection ranges for different ADCs. Furthermore, the developed software will enable users to obtain the readings for a single ADC module. Finally, as shown in Fig. 20, the user can select which channel(s) to obtain readings from and choose the update time; for example, every 5 s, the system registers a reading.

The biological model: the rationale behind the selection of the melanoma cell lines for the in vitro experiment

Well-established-eight-melanoma cancer cell lines have been prudently selected with distinctive genetic complexities and genomic mutations; they were categorized into two groups: Group I (SK-MEL-1, A-375, G-361, WM-115) and Group II (NM-2C5, M-4A4, M4A4 LM3-4 CL16 GFP ((CL 16)), M4A4 LM3-2 GFP ((LM3))). The cell lines have been procured from the American Type Culture Collection (ATCC, Maryland, USA), and all cell culture plasticware was supplied by Corning (Corning Life Sciences, Leicestershire, UK). The melanoma cell lines, grouped in II, clearly illustrate the genetic complexities and intensity of metastasis among all cell lines within this cluster; on the other hand, Group I exhibits four cell lines that are closely related in terms of malignancy severity, yet this would significantly manifest the notable merit of the proposed biomechatronic platform in allocating the fine distinction of malignancy grade/intensity among these four cell lines in particular, based on their electrophysiological heterogeneity.

As per the ATCC specifications, SK-MEL-1 cell line^{147,148} is a primary tumor source extracted from a lymphatic metastatic system of a widely spread malignant melanoma skin tissue within a human *Homo sapiens* organism. The cell line has been acquired from a thoracic duct of a 29-year-old Caucasian male patient. The A-375 is an adherent primary malignant cell line, which was derived from a 54-year-old female’s skin tissue within the *Homo sapiens* organism of 62 chromosomes that shows a rapid growth^{149,150}. The primary malignant melanoma, G-361 cell line^{151–153}, was extracted from a skin tissue within *Homo sapiens* of a 31-year-old Caucasian male. The fourth cell line encompassed in the class I group is WM-115¹⁵⁴, which is an adherent primary melanoma skin cancer of *Homo sapiens* organism extracted from a 58-year-old female.

The 4-cell lines within Group II are isogenic (genetically alike) and are derived via serial dilution of polyclonal and metastatic human breast cancer cell line MDA-MB-435¹⁵⁵. As per ATCC, they are all adherent cells derived from a 31-year-old Caucasian female. The 4 cell lines within Group II possess a distinctive degree of metastatic intensity. NM-2C5 is a non-metastatic cell line, M-4A4 is an early-stage metastatic (lungs and lymph nodes), LM3 is an intermediate metastatic initiated from a second-generation lung metastasis, and finally, CL16 is a highly metastatic melanoma, and it has initiated from a third generation-lung metastasis¹⁵⁵.

It is a debatable issue among scholars within the cellular biology field of the initiation of the cell lines within Group II, whether they represent breast cancer or melanoma on the essence of the parent cell line MDA-MB-435. Ross et al.¹⁵⁶ have identified the systematic variation within gene expression in characterizing MDA-MB-435, and they concluded that its gene expression pattern is closer to melanoma as opposed to breast cancer. Furthermore, it is found that MDA-MB-435 is of melanocytic origin based on immunohistochemical staining¹⁵⁷. Finally, MDA-MB-435 shares the same origin as the melanoma cell line, M14, as per a single nucleotide polymorphism (SNP) array analysis¹⁵⁸. Therefore, it is concluded that such four-cell lines within Group II do represent melanoma.

Materials and methods

Cell culturing protocol and growth inhibition

All cell lines within Group I and II, as well as the calibrating cancer cell line model MCF7 (early-stage breast cancer cell) and invasive breast cancer cell line (MDA-MB-231), were cultured per the protocol set forward by ATCC. This includes multiple washing processes, staining, suspension, filtering, centrifugation, and aspiration. The design constraints associated with the cell culturing microenvironment are highlighted in³⁴.

The calibrating cancer-cell-line models, MCF7 and MDA-MB-231, are utilized since their cell-membrane potentials are well documented in peer-reviewed literatures^{47,159–161}. Hence, they shall both act as calibrating tools to check the applicability of our proposed miniaturized biomechatronic platform. All cell lines were extracted at the logarithmic (Log) growth phase to arrive at the maximum viability of cells and highly active proliferation kinetics; the genetic stability was maintained by not exceeding ten times the cultures’ passage from frozen stock.

SK-MEL-1 Cell lines of Group (I) were cultured in eagle’s minimum essential medium (EMEM) (ATCC 30-2003, Middlesex, UK) as a growth medium, supplemented at 10% concentration with fetal bovine serum (FBS), and streptomycin plus penicillin (100 µg/ml and 100 u/ml, respectively). During the SK-MEL-1 culturing process, non-essential amino acids and 1 mM sodium pyruvate were added. The entire process was conducted in a laminar flow chamber, where the culture was conditioned to a humidified atmosphere of 98% relative humidity and 5% CO₂, at a 37 °C temperature. The medium was renewed 2–3 times a week or during acidification, per

the pH indicator (phenol red). Within the same group, the lightly pigmented human melanoma cell line, G-361 (ATCC, Middlesex, UK), is cultured in an ATCC-formulated McCoy's 5a medium modified (ATCC 30-2007), supplemented with 10% FBS and 1% penicillin-streptomycin (10,000 U/ml and 10,000 µg/ml, respectively) in 5% CO₂, at 37 °C culture conditions.

The adherent epithelial primary melanoma cell lines, WM-115, were cultured in ATCC-formulated eagle's minimum essential medium (EMEM, ATCC: 30-2003), containing a 10% concentration of FBS. The cultured conditions were maintained at 34 °C in a 5% CO₂ atmosphere. Finally, within this batch, A-375 was maintained in a growth medium of ATCC-formulated dulbecco's modified eagle's medium (DMEM, ATCC: 30-2002), supplemented with fetal bovine serum (10%) at 37 °C in a CO₂ incubator (95% relative humidity, 5% CO₂).

The early-stage breast adenocarcinoma cell, MCF-7, was cultured in a growth base medium of ATCC-formulated eagle's minimum essential medium (EMEM, ATCC: 30-2003), supplemented with fetal bovine serum to a final concentration of 10%, and 0.01 mg/ml human recombinant insulin, at 37 °C in CO₂ incubator (95% relative humidity, 5% CO₂).

An adhesive human breast cancer cell line (MDA-MB-231), procured from ATCC, was extracted from a 51-year-old Caucasian female. The cell was cultured in Leibovitz's L-15 medium (ATCC, Middlesex, UK), supplemented with 10% fetal bovine serum (FBS). The cell layer was rinsed with 0.25% (w/v) Trypsin – 0.53 mM EDTA solution to eliminate traces of serum (trypsin inhibitor). The cell lines were harvested by trypsinization by adding 2–3 mL of trypsin-EDTA solution. A growth medium and a considerable amount of aliquots were then added, and finally, cultures were incubated at 37 °C without CO₂.

The cell lines of Group II were derived from the triple-negative human breast cancer cell line, MDA-MB-435. They were maintained in dulbecco's modified eagle's medium (DMEM) (ATCC 30-2002, Middlesex, UK), supplemented with 10% fetal bovine serum (FBS) and 5% penicillin/streptomycin (P/S). Cultures were propagated and conditioned in a humidified atmosphere of 5% CO₂, at a temperature of 37 °C. Table 7 summarizes the cell culturing protocol and growth inhibition of all cell lines within Groups I and II.

Cell viability check, serial dilution, and system sterilization

The culturing process is proceeded by a viability test. The cell viability and counting are investigated through the Moxi Z mini automated cell counter (ORFLO Technologies, WA, USA). A sample of 75 µL of the cultured cell medium is extracted via a micropipette and then injected into one of the two-fill ports of the Moxi Z device. The Moxi Z cassette consists of a microfluidic culturing reservoir and channels crossed by an array of microelectrodes. The Moxi Z device utilizes the gold standard Coulter Principle with a patented thin-film sensor technology to report accurate cell viability marks, numbers, and mechanobiology results in 8 s. The gold standard counter is based on cell impedance², where passing batches of cells through the microchannel leads to escalation of resistivity; thus, by Ohm's law (i.e., V ((voltage))=I ((current)) x R ((resistance))), this yields an increase in voltage that are exemplified as spikes of each passing cell; equally sized spikes are aggregated into a curve-fitting histogram.

Acquiring the number of cells per unit volume via Moxi Z enables the extraction of a single cell through serial dilution in a 96-well plate. The dilution factor was 0.1 (e.g., each subsequent well is tenfold diluted). The extracted single cell was allocated using a Keyence VHX-2000ES digital microscope (Keyence, Milton Keynes, UK). A trypan blue dye is used to confirm cell viability during the serial dilution stage, where dead cells lose their integrity and absorb the blue dye.

The entire system could be sterilized by different means; it can be performed by pumping ethanol into the µF chamber. Sterilization can also be carried out by exposing the device to UV light, as in¹⁶². Furthermore, plasma can be used for patterning features on the substrate, strengthening bonding, surface treatment to the microfluidic structure, as well as sterilization of the µF device as in¹⁶³. The microfluidic surface treatment is

Cell line	Group	Characteristic	Cultured in
SK-MEL-1	I	Primary metastasis melanoma	Eagle's minimum essential medium (EMEM) + 10% concentration with fetal bovine serum (FBS) + streptomycin plus penicillin (100 µg/ml and 100 u/ml, respectively)
A-375	I	Late invasive malignant melanoma	ATCC-formulated dulbecco's modified eagle's medium (DMEM) + FBS (10%)
G-361	I	Primary metastasis melanoma	ATCC-formulated McCoy's 5a medium modified (ATCC 30-2007) + 10% FBS + 1% penicillin streptomycin (10,000 U/ml and 10,000 µg/ml, respectively)
WM-115	I	Low-metastasis melanoma	ATCC-formulated Eagle's minimum essential medium (EMEM) + 10% FBS
NM-2C5	II	Non-metastatic melanoma	Dulbecco's modified eagle's medium (DMEM) + 10% FBS + 5% penicillin/streptomycin (P/S)
M-4A4	II	Early-stage (weakly metastatic)	Dulbecco's modified eagle's medium (DMEM) + 10% FBS + 5% penicillin/streptomycin (P/S)
M4A4LM3-4CL16 GFP (CL 16)	II	Intermediate (moderately metastatic)	Dulbecco's modified eagle's medium (DMEM) + 10% fetal bovine serum (FBS) + 5% penicillin/streptomycin (P/S)
M4A4LM3-2GFP (LM3)	II	Highly invasive metastasis melanoma	Dulbecco's modified eagle's medium (DMEM) + 10% FBS + 5% penicillin/streptomycin (P/S)
MCF-7	Calibrating cancer cell-line model	Poorly invasive human breast adenocarcinoma	Eagle's minimum essential medium (EMEM) + 10% FBS + 0.01 mg/ml human recombinant insulin
MDA-MB-231	Calibrating cancer cell-line model	Invasive-metastasis breast cancer	L-15 medium + 10% FBS

Table 7. Summary of the cell culturing protocol and growth inhibition of all cell lines within Groups I and II, as well as calibrating cancer line models.

performed by inducing O_2 plasma to its mechanical structure, which makes the hydrophilic characteristic of the μF surface more pronounced and enhances adhesion¹⁶⁴. On the contrary, to prevent cells from adhering to the channel surfaces, a 5% w/v bovine serum albumin (BSA, Sigma) could be induced into the microchannel and incubated overnight as in¹⁶³.

In vitro experiments

The microfluidic-multi-electrode module (LoC) was first filled with DI water to remove any resultant debris from the microfabrication processes, and measures were taken to avoid forming air pockets within the system. Then, a sterilization process was performed using ethanol. At last, a PBS wash was implemented to enhance the biocompatibility of the structure, and then the system was left to dry. At the termination of the experiment, trypsin was utilized to detach cells from the LoC domain, followed by DI water filling, sterilization, and PBS wash for miniaturized device reusability.

The in vitro experiments have been conducted under clean room conditions, where the entire experimental microelectronic hardware and micromechanical structure components are placed on an anti-vibration table to eliminate noises and damp any residual vibrational energy into the experimental system; the experimental setup is shown in Fig. 21.

The electromagnetic field radiation within the immediate vicinity of the miniaturized system was measured by an EMF meter, which was negligible: 12×10^{-14} Tesla. This assures that electromagnetic interferences with the in vitro experimental setup are minimal. The multifunction meter examined the connecting pads and patterned electrodes to investigate the faithfulness of the proposed miniaturized device in registering signals.

The experiments have been conducted at various stages. At stage (-1), measurements were taken directly from the miniaturized device without adding any biological substances or liquid. Stage (0) is followed by adding a buffer medium (PBS) to the microfluidic culturing reservoir, and then readings were registered; stage (1) is injecting trypan blue dye, and measurements were collected. The trypan blue dye is utilized for the subsequent stage of investigating cell viability. Finally, a single cell is extracted from the serial dilution process by a micropipette and injected into the iLoC domain. Breaking the experiments into stages critically assists in allocating and eliminating noises within the system and eventually arriving at the distinctive potential of the cancer cell. Furthermore, the developed customized driving software has an embedded triangle smoothing algorithm, which enhances the signal-to-noise ratio and reduces noise. Syringes were used to trap cells within the microfluidic/MEA domain, and a Keyence flexible microscope was utilized to monitor cell positioning. Different values of potential stimulations through the working electrode were used, and over 500 recording

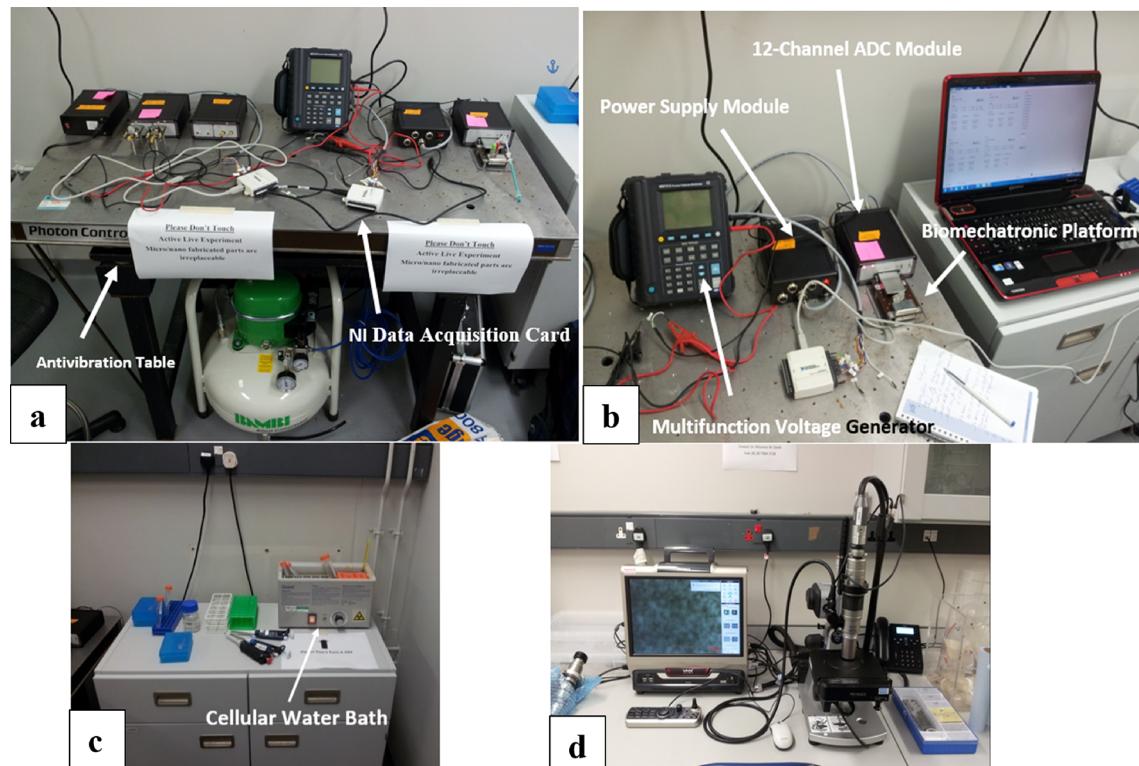


Fig. 21. Electrophysiology in vitro experimental setup. (a) Anti-vibration table and NI data acquisition card. (b) Miniaturized biomechatronic platform, multifunction voltage generator, 12-channel-ADC module, and power supply module. (c) Cellular water bath to maintain a temperature of 37 °C for cultured cells. (d) VHX-2000ES Keyence Digital Microscope.

points were registered in a number of trials for each melanoma cell type, together with the well-documented MCF-7 and MDA-MB-231 cell line model, achieving repeatability in the obtained registered data.

Results and discussion of the electrophysiology in vitro experiments

On the basis of cellular electrophysiology, the cell-line models have been selected to investigate the heterogeneity of melanoma cells, which exhibit different genetic complexities. First, a number of in vitro experiments were conducted on well-documented-cell-line models in biophysics literature: poorly invasive human breast adenocarcinoma (MCF-7) cell line and human breast cancer cell line (MDA-MB-231). The resultant electrophysiology potential of MCF-7 was found to be -43.96 ± 0.43 mV (Mean \pm SD, n=18 trials ((single cell per trial))), whereas the cellular potential of MDA-MB-231 was -25.78 ± 0.17 mV (Mean \pm SD, n=19 cells), where SD is the standard deviation.

The obtained results have placed confidence in the developed biomechatronic platform, as the extracted cell-membrane potential of MCF-7 and MDA-MB-231 were within the range of peer-reviewed findings within the literature, in which they were obtained through different methods, e.g., the standard patch clamp method or fluorescence method. It's reported in^{159,160} that MDA-MB-231 possesses a cell-membrane potential of -29.2 ± 1.6 mV, while MCF7 has a cell-membrane potential of -42.1 ± 5.3 mV⁴⁷.

As per the obtained experimental findings, it is found that as the stage of metastasis ascends, the magnitude of cell-membrane potential drops. The highly invasive metastatic melanoma cell, CL16, experiences the lowest cell-membrane potential in magnitude (-4.324 ± 2.98 mV, n=26), as opposed to non-metastatic (NM-2C5) and early stage (M-4A4) cell-line melanoma, whose cell-membrane potentials are respectively, -48.27 ± 3.08 mV (n=26), and -42.50 ± 2.56 mV (n=21). Similarly, by examining the metastases of WM-115 (low), LM3 (intermediate), and A-375 (Late), they show a distinctive variation of cell-membrane potentials in descending order of magnitude: -37.29 ± 2.11 mV (n=19), -27.28 ± 2.89 mV (n=24), and -12.69 ± 2.79 mV (n=23), respectively. Interestingly, the proposed miniaturized biomechatronic platform has managed to discriminate between the closely comparable melanoma cell lines in terms of metastasis based on their extracted electrophysiology: G-361 and SK-MEL-1. The former exhibits a cell-membrane potential of -31.88 ± 1.67 mV (n=20), while the latter has a cell-membrane potential of -27.84 ± 2.66 mV (n=22).

The relatively small spread of measurements could be attributable to instrumentation errors due to weak soldering of the flexible cable with some patterned gold electrodes on a glass substrate and/or external noise interferences to the experimental setup. However, as illustrated earlier, the microfabricated components, soldered connections, and measurements of electromagnetic interferences were closely examined to keep the source of errors as minimal as possible. Furthermore, the micro-device was extensively sterilized and cleaned after each in vitro experimental trial to avoid cross-contamination. The resultant cell-membrane potentials (V_m) of the melanoma and the calibrating breast cancer cell line models are summarized in Table 8.

As it has been illustrated in Alqabandi et al.², cancer cells differ from healthy ones by having an increase in their permeability (fusion pore size), leading to an influx of water and Na^+ , and efflux of K^+ , Mg^{2+} , and Ca^{2+} ions out of the cell. As fairly discussed in sections “[Cancer electrophysiology](#)” and “[Mathematical modeling of the electrophysiology of a living cell: analytical approach](#)”, this ultimately leads to a drastic reduction of cell-membrane capacitive characteristics in storing ion charges, a decrease in depolarization and hyperpolarization time, as well as a drop in cell-membrane potential. Also, this sheds light on the interrelated effect of cellular electrophysiology and mechanobiology of cells, such that the physical characteristic of cells affects their permeability and, thus, its biophysics; the mechanobiology of cells will be deliberately addressed in the upcoming section. Therefore, as a cell progresses in the cancer stage, its permeability increases; hence, its electrophysiological potential drops in magnitude. The advancement of the cancer stage is allocated by the decline of the magnitude of the cell-membrane potential, and this is a manifestation of the depolarization process taking place^{39,43,45,47–49,130}. The depolarization could be attributable to a reduction in the intracellular activities of K^+ ion, and/or an increase in the intracellular activities of Na^+ ³⁹. Thus, depolarization is experienced with melanoma cells as they ascend in the stage of their tumorigenesis. To the best of the authors' knowledge and the performed extensive literature review, this is the first time that the characterization of the electrophysiology of

Cell-line model	Description of metastasis	V_m (mV)	n
MCF-7	Poorly invasive human breast adenocarcinoma	-43.96 ± 0.43	18
MDA-MB-231	Invasive-metastasis breast cancer	-25.78 ± 0.17	19
NM-2C5	Non-metastatic melanoma	-48.27 ± 3.08	26
M-4A4	Early-stage (weakly metastatic)	-42.50 ± 2.56	21
WM-115	Low-metastasis melanoma	-37.29 ± 2.11	19
G-361	Primary metastasis melanoma	-31.88 ± 1.67	20
SK-MEL-1	Primary metastasis melanoma	-27.84 ± 2.66	22
M4A4LM3-2GFP	Intermediate (moderately metastatic)	-27.28 ± 2.89	24
A-375	Late invasive malignant melanoma	-12.69 ± 2.79	23
M4A4LM3-4CL16 GFP	Highly invasive metastasis melanoma	-4.324 ± 2.98	26

Table 8. The resultant extracted electrophysiology potential of melanoma and breast cancer cell lines in mV (healthy, early-stage metastasis, intermediate, late, and highly invasive metastasis).

the different stages of melanoma is being achieved, leaving the cell-membrane cytoplasmic component intact as opposed to other invasive methods in extracting cell-membrane potential, e.g., patch clamp method.

In vitro real-time characterization of melanoma contractile force via a self-probing cantilever-based biomechatronic platform

Review of the different approaches in quantifying the contractile force of cells

As fairly explained in Section “[Cancer mechanobiology](#)” and depicted in Fig. 3, Cellular mobility initiates due to received electrochemical, mechanical, and/or diffusible/non-diffusible signals picked by receptor proteins on cell membrane^{2,64}. During mobilization, cells form ECM via focal adhesion complexes with the surrounding environment. As they move, they experience external forces, e.g., viscous interaction and internal forces of the cellular cytoskeleton^{63,64,165}. It is, therefore, the dominant cellular contractile force that overcomes other external and interaction forces to push the cell forward, which has been experimentally characterized through invasive and non-invasive manners; this can be grouped into three categories: local point probing, entire cell probing, and a population of cells probing^{64,166}.

Figure 22 shows different methods for extracting cellular contractile force. Exposing a cell or a population of cells to a shear flow in a cone-and-plate viscometer (Fig. 22a), and then by applying Navier Stoke’s equation, the cellular contractile force with respect to the shear stress exerted on cells would be estimated^{63,167}. Similarly, extracting the contractile force of a cell or a population of cells can be achieved by forcing a cell or a group of cells to adhere to a thin polymer substrate, e.g., Si, coated with ECM-cell-molecular adhesion (Fig. 22b), and then cells would experience tensile or compression test⁶⁴. However, such approaches extract the mechanobiology of cells in an imposed/forced manner, which raises the question of whether the findings of such approaches would genuinely represent the contractile force of a cell. AFM¹⁶⁸, Fig. 22c, and magnetic twisting cytometry (MTC)^{19,169,170}, Fig. 22d, both perform a local point deformation on a cell, wherein the former approach, the tip needle deflection of the AFM cantilever, can be correlated to the cellular force. In contrast, the latter approach utilizes a magnetic field to force a magnetic bead to deform the cell, and eventually, such elastic/viscoelastic deformation is correlated to cellular contractile force. The MTC method is similar to the hardness test in solid mechanics. These last stated two methods are invasive and cannot be applied to a population of cells.

Optical tweezers or laser-trap approach¹⁷¹ uses a laser beam to attract a high refractive dielectric silica bead into a cell and hence forces a whole cell to deform (Fig. 22e). In a similar manner, but with mechanical deformation, the micropipette aspiration technique imposes suction of a cell^{19,169,170}. By ignoring the frictional forces between the cell and the internal surface of the micropipette, the changes in cellular geometry (elasticity) are correlated to cellular force (Fig. 22f). However, both approaches are invasive. They can endanger the viability of a cell. A seventh approach is culturing a cell in an array of nano/micropillars^{172,173}, where the cell is then exerting additional force when migrating to a new location (Fig. 22g). This again raises the paradox question of whether the resultant forces, correlated to those deflected pillars, are again genuinely representing the cellular contractile force or not. Also, such an approach requires optical imaging to record the deflection of the nano/micropillars, which adds to the cost and complexity of the experimental setup; this would be constrained by the optical resolution. Also, cells differ in morphology when experiencing a micropillar environment during their migration, as opposed to flat surfaces. Another approach is named a 3D-ECM-invasion assay (Fig. 22h), where cells are spread on collagen, and then their surface indentations are measured after cell de-attachments¹⁷⁴. However, such an approach requires a time-consuming experimental preparation and setup.

A cantilever-based micro-electro-mechanical system (MEMS)^{166,175} is used to record the deflection of the beam in response to exerted cellular surface compressions on the functional layer of the beam via Piezoresistive elements, where such deflection is then correlated mathematically to cellular contractile force (Fig. 22i). This approach is non-invasive. It can be applied on a single as well as a population of cells, has a self-registering mechanism, can operate in a controlled microfluidic environment to maintain cell viability, is cost-effective, and, most importantly, reports the dynamics of a cell in real-time. Therefore, such an approach is highly advocated in this research to extract the contractile forces of melanoma cells.

Cantilever-based N/MEMS platform

Despite the infancy of the nano/micro-electro-mechanical-system field in probing the contractile force of cells, yet it has grown massively among biotechnologists for the past decade to explore the mechanobiology of cells⁶⁸. Yin et al.¹⁶⁶ have microfabricated a cantilever within a microfluidic channel to measure the contractile force of a cell. An embedded Piezoresistive mechanism, forming a Wheatstone bridge, has been utilized to capture the deflections of a beam. They have implemented the negative dielectrophoretic (nDEP) to trap a cell. Similarly, Yang and Yin¹⁷⁵ have designed and analyzed a Piezoresistive microcantilever to sense surface stresses generated from a cell loading on the cantilever. They propose improvements in sensitivity by modifying the dimensions, and at the same time, they have allocated sources of noise within the system. On the other hand, Goericke and King¹⁷⁶ investigate different configurations of a microcantilever sensor and its embedded Piezoresistive elements to enhance the sensitivity of the microdevice.

Raorane et al.¹⁷⁷ have utilized an Au/Si N_x-based-coated-microcantilever-paddle array configuration to quantify protein enzymes associated with a disease. In their work, the minute mechanical structure acts as a transducer of biological intermolecular forces. Ricciardi et al.¹⁷⁸ have proposed a label-free-microfluidic cantilever array in an immunoassay application within a liquid domain. They have uniquely utilized Pyrex material instead of the conventional PDMS in fabricating their microfluidic channel. Their proposed system can be utilized to progress cancer cell mutation. They highlight the merits of performing experiments in liquid as opposed to vacuum or air, in which it reduces the false and positive negative response in measured data, and most importantly, considering that cell membrane and proteins change their morphology status, depending on the domain they are in – liquid or vacuum/air domain. Park et al.⁷⁴ have quantified the contractile forces of self-

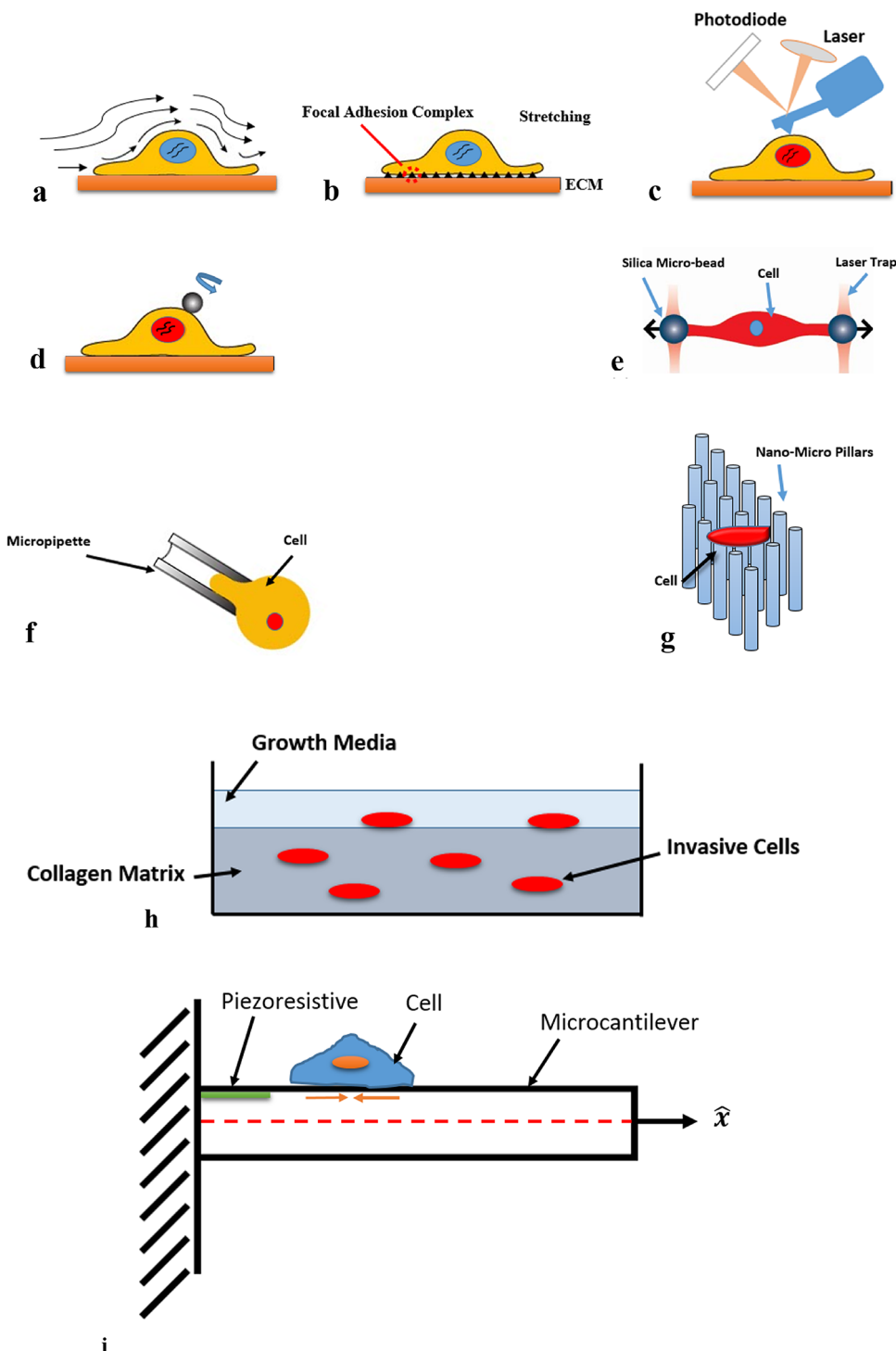


Fig. 22. Various approaches in extracting cellular contractile force. (a) Shear flow analysis method. (b) Substrate focal adhesion complex approach. (c) AFM approach. (d) MTC approach. (e) Laser trap approach. (f) Micropipette approach. (g) Micropillar approach. (h) 3D-ECM-invasion assay method. (i) Piezoresistive cantilever-based approach.

organized cardiomyocytes by utilizing a flexible, transparent, and biocompatible microcantilever array. Their technique for seeding cells on the cantilever array ensures a damage-free cell structure.

Understanding the mechanobiology kinetics and kinematics: mathematical modeling

The majority of scholars in the field of cantilever-based probing contractile forces employ the discrete model of Stoney's Eq. ¹⁷⁹, in which the cantilever's deflection is correlated to mechanical stresses. However, such a discrete model requires the knowledge of the modulus of elasticity (E), as well as Poisson's ratio (ν) of the investigated

biological model, whose values are most often missing experimentally. This forces biologists to make rough assumptions on such values, which would question the reliability of their obtained contractile force findings.

In this paper, and as a new contribution in mathematically expressing the contractile force of a cell on a microcantilever-beam structure (Fig. 23), a Heaviside step function $H(s)$ ¹⁸⁰, as well as pin-force model¹⁸¹ are utilized in formulating a mathematical term representing the contractile force of a cell.

Beam's theory describes a relationship between the deflection of the cantilever and applied load, where stiffness factor (EI) is mainly considered constant^{180,182,183}. As illustrated in Fig. 23, a living cell is defined by two coordinates with respect to the clamped end of the cantilever: s_1 (starting coordinate), and s_2 (ending coordinate of the cell). The beam is assumed to be an inextensible isotropic beam. The thickness of the beam is denoted as t_b , whereas the thickness of the cell (height) is denoted as t_c . The transverse deflection of the beam is expressed as $\hat{\eta}(s, t)$. Living cell's cytoskeletal forces generate surface compression on the functional surface of the cantilever. The resultant force of the rear and front of the cell yields a net force pushing the cell forward, leading to a transverse deflection of the beam upward. The equation of motion describing the system is given by^{180,182,183}

$$\rho A \ddot{\eta} + EI \eta^{iv} = q(s, t) \quad (37)$$

where, $q(s, t)$, is the total resultant distributed load on the beam, and since the load is the moment; thus,

$$q(s, t) = \frac{\partial^2 M}{\partial s^2} \quad (38)$$

where M defines the uniformly distributed bending moment acting on the beam, and it is expressed as in^{180–183}

$$M = \frac{F(t_b + t_c)}{2} [H(s - s_1) - H(s - s_2)] \quad (39)$$

The associated geometrical, as well as dynamic force boundary conditions of the system, are defined in¹⁸⁰

$$\begin{aligned} \eta &= 0 \quad \text{and} \quad \eta' = 0 \quad \text{at } s = 0 \\ \eta'' &= 0 \quad \text{and} \quad \eta''' = 0 \quad \text{at } s = L \end{aligned} \quad (40)$$

Generating a reduced-order model of the system by expressing the beam's deflection, η , in terms of Galerkin expansion, yields

$$\eta = \sum w(s) u(t) \quad (41)$$

where, $u(t)$ are generalized temporal coordinates and $w(s)$ represent orthonormal mode shapes of the cantilever beam, defined as in^{180,182,183}

$$w(s) = \sum_1^n A \cos(r_n s) + B \sin(r_n s) + C \cosh(r_n s) + D \sinh(r_n s) \quad (42)$$

By substituting the boundary conditions, Eq. (40), and considering only the first mode shape, the deflection term can be simplified as,

$$w(s) = C[\cosh(r_n s) - \cos(r_n s) - \sigma(\sinh(r_n s) - \sin(r_n s))] \quad (43)$$

The frequency, r_n , is obtained by the characteristic Eq. (44), whereas σ is defined by Eq. (45), and C is obtained by normalizing the mode shapes through Eq. (46)¹⁸⁰.

$$1 + \cosh(r_n s) \cos(r_n s) = 0 \quad (44)$$

$$\sigma = \frac{\cosh(r_n L) + \cos(r_n L)}{\sinh(r_n L) + \sin(r_n L)} \quad (45)$$

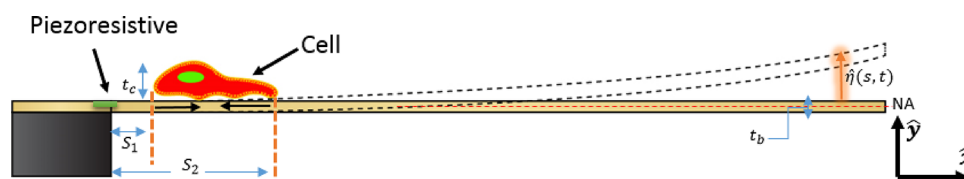


Fig. 23. Schematic illustration of a deflected beam due to exerted contractile force (compressive surface stresses) of a living cell experiencing motility.

$$\int_0^L w(s)^2 ds = 1 \quad (46)$$

By substituting Eqs. (41) and (46) into the equation of motion (37), multiplying by mode shape $w(s)$, integrating over the entire domain length of the beam and utilizing the orthonormal properties of the linear mode shapes, the following term is obtained,

$$\begin{aligned} EI r_n^4 u &= \frac{F(t_b + t_c)}{2} [w'(s_1) - w'(s_2)] \\ u &= \frac{F(t_b + t_c)}{2EI r_n^4} [w'(s_1) - w'(s_2)] \end{aligned} \quad (47)$$

where ‘ u ’ is the normalized deflection of the system, and by applying Eq. (48), defining the dimensional experimental deflection of the beam, $\hat{\eta}$, as per the obtained output voltage signals from the Piezoresistive elements, u is then obtained. It has been found that the registered data of output voltage signals from the Wheatstone bridge are correlated to the cantilever’s static deflection by the following Eq. 184–187:

$$V_{out} = V_{in} \frac{\Delta R}{R} = V_{in} \sigma \pi = V_{in} \frac{3Et}{2L^2} \eta \quad (48)$$

where, V_{in} is the supply potential to the Wheatstone bridge (1 V), V_{out} is the output voltage signal of the bridge, ΔR is the strain gauge (Piezoresistive change) of the Wheatstone bridge, σ stress component, π is Piezoresistive coefficient ($70 \times 10^{-11} \frac{m^2}{N}$), E is the modulus of elasticity, t is thickness, L is the total length of the cantilever, and η is the beam’s deflection.

$$\hat{\eta} = uw(L) \quad (49)$$

The deflection at length L of the beam is defined by $w(L)$. Obtaining the experimental reading of the deflection of the beam due to cellular motility would give the contractile force, F , experienced by the beam (Eq. (47)); hence, the effective contractile force of the cell, F_C , is obtained by,

$$F_C = \frac{2F\pi(\frac{d_C}{2})^2}{b(s_2 - s_1)} \quad (50)$$

where, d_C and b , respectively, represent the cellular diameter and width of the beam. A numerical algorithm is developed in Maple (Maplesoft, Ontario, Canada) to solve for F_C with respect to the experimentally obtained deflections of the beam.

The μ -cantilever based bio-mechatronic platform

Microfabrication of the cantilever-based biomechatronic sensor: mechanical structure

The microfabrication processes are carried out to construct a biomechatronic platform with a cantilever base that captures cellular mechanobiology, such as contractile force. As shown in Fig. 24, the proposed miniaturized mechanical structure consists of a μ -cantilever, μ -fluidic domain, a gold electrode patterned on a glass substrate, a mechanical seal, and copper connection arms, the Cu arms of which are later shown in Fig. 28.

The copper spring arms transmit DC potential to the patterned gold electrode, creating electrostatic force with the μ -cantilever. The gold electrode is intentionally patterned symmetrically on the glass substrate to accommodate the two copper springs, thus ensuring a faithful and smooth transition of charges in case of any fabrication default that might have yielded a partially developed electrode pattern on the glass substrate.

The microfabrication processes were started by Piranha cleaning (3:1 = H_2SO_4 : H_2O_2) for 30 min, which was performed on glass substrates. This was followed by backside protection through spin coating, adding ~ 2 μm photoresist film as a post-process to deicing. Photoresist/polymer layers protect surfaces from dicing dust (Silicon Oxide particles); if such dust particles touch the glass surface, they form van der Waals’ force, and they can’t be removed easily. Then, a die saw was utilized to cut the two-glass upper and lower steps: 10×20 mm and 17×20 mm, respectively. The die-sawed-glass substrates are then cleaned by isopropyl alcohol (IPA) and acetone. The development of the patterned gold electrode is carried out through a standard lift-off process via optical photolithography.

A positive photoresist, AZ 1518 (Microresist, Berlin, Germany), had been utilized to coat the glass substrate; then it was spun at 3000 rpm (forming a layer of $1.8 \mu m$ thick); this was proceeded by a prebake process on a hotplate for 1 min at $115^\circ C$. A dosage of 60 mJ high-resolution exposure, together with a patterned mask, was performed. Finally, the glass substrates were developed using a resist developer AZ 400 K 1:4 in a beaker for 6 min, where no post-bake process was carried out. The metallization process was performed by Argon sputtering, where an adhesive layer of 5 nm Ti and 300 nm of the functional layer of Au were deposited on the AZ1518 resist structure. A 4-h lift-off process was performed at $80^\circ C$ using dimethyl sulfoxide (DMSO). This was followed by a cleaning process using IPA and acetone.

The die-sawed glass substrates were spin-coated using AZ1518 photoresist structure as an adhesive layer. The 20×10 mm glass substrates, on which the Au/Ti electrode is patterned, and two microscopic glass slides of 2×1 mm in size, were both aligned and then all were bonded to the 17×20 mm glass substrate through a polymer on

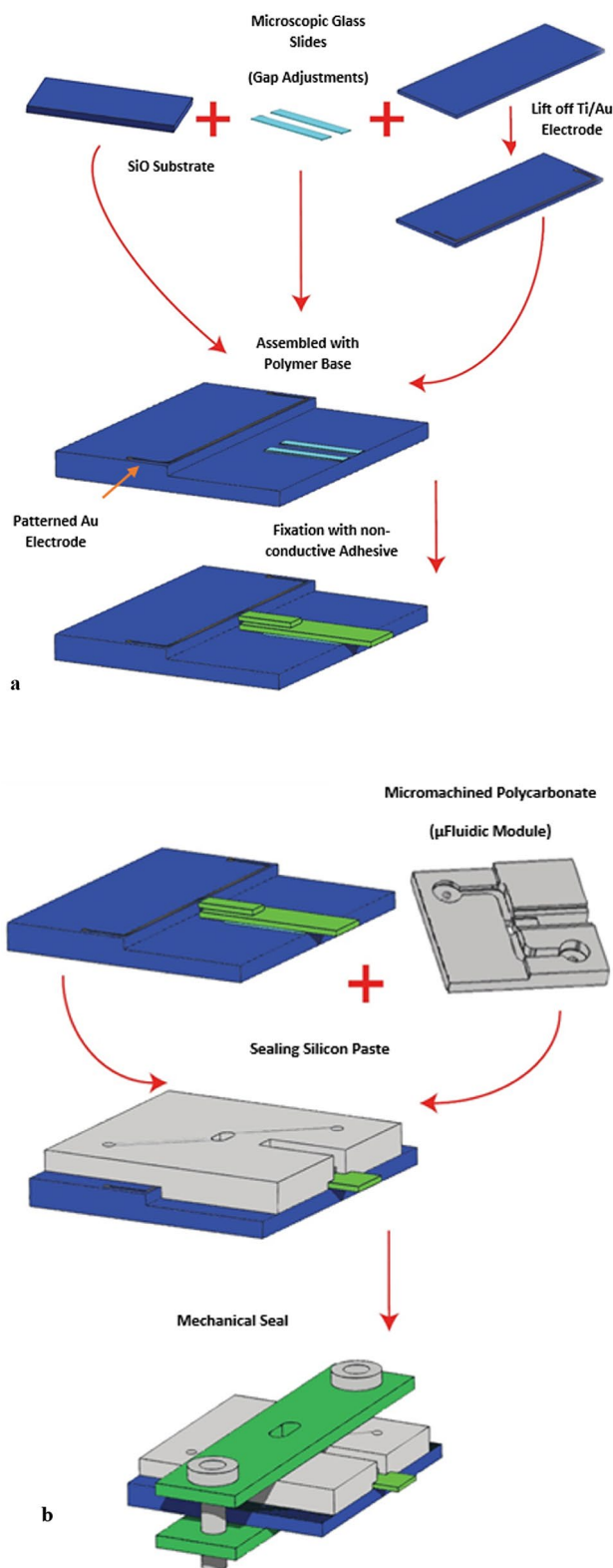


Fig. 24. 3D drawings of the proposed miniaturized mechanical structure of the cantilever-based mechatronic platform consisting of (a) The mechanical assembly of the patterned gold electrode on a glass substrate, microcantilever, microscopic glass slides, and the diced glass steps. (b) The polycarbonate (PC) microfluidic domain is assembled with the mechanically assembled components in (a).

a hot plate, for 1 min at a temperature of 115 °C. The two microscopic glass slides were used to ensure alignment, equally spaced gap, and leveling of the microcantilever structure when it is finally bonded to the overall structure through a non-conductive adhesive substance (Henkel, Düsseldorf, Germany).

The Wheatstone Piezoresistive microcantilever was fabricated through a process of wet etching and double side polished of n-type <100> silicon wafer, with ground doping n-type, following the process described in detail in^{188,189}. A wafer oxidation and silicon-oxide-dot-patterning method, together with dry plasma etching and thermal oxidation, were all utilized to define the sharp features of the microcantilever. This was followed by optical lithography and phosphorus implementation to form the electrical shielding lines that efficiently eliminated electrical crosstalk between actuation and sensing elements. The Piezoresistive set of the Wheatstone bridge was fabricated by ion and post-annealing process for 30 min, at a temperature of 850 °C^{188,189}.

Plasma-enhanced chemical vapor deposition (PECVD) was utilized to deposit silicon nitrides as an insulating protection film, followed by a standard metallization process. Notably, the microcantilever was insulated (electric passivation) by depositing low-stress PECVD silicon nitride, empowering the microcantilever to perform in different environments, experiencing various conductive buffered media^{188,189}.

An optimized annealing process with controlled doping conditions was carried out to produce highly sensitive Piezoresistive elements^{184,188,189}. The Wheatstone piezoresistors were insulated with silicon nitrides; hence, the microelectronic components would be protected from any fluid contact, and it would diminish electrical noises attributable to crosstalk among electronic components. Moreover, the Piezoresistive elements were formed at the microbeam (root) support anchor, where thermal stability was achieved and sensitivity was enhanced. The Piezoresistive elements of the Wheatstone bridge are located in the longitudinal direction of the beam, and it is of full symmetrical bridge configuration, resulting in four orders of magnitude higher signal than a single piezoresistor configuration (more thermal stability and controllability over offset compensation)¹⁸⁴.

A functionalized circular gold (Au) pad layer was deposited within the cantilever rigid body portion. This would ensure the biological–chemical interaction of the loaded cell with the cantilever active surface, achieving an affinity of molecular-level interaction between the targeted analyte (biological specimen) and the thin layer of the gold pad. Finally, gas plasma and wet etching released the microcantilever mechanical structure.

Due to its robustness in micromachining and extensive use as a biocompatible material, polycarbonate (PC)^{190,191} was micromachined to form the microfluidic reservoirs and channels. The two connecting adaptors, shown later in Fig. 28, were adhered to the clean upper surface of the polycarbonate substrate through the ultraviolet adhesion process. An opening window was made through the polycarbonate structure for cell loading via a micropipette.

The miniaturized mechanical components were assembled and mechanically sealed. The assembled components were examined under the microscope to verify design specifications, investigate any microfabrication deficiencies, and analyze the overlap of the tip of the microcantilever with the patterned gold electrode on the glass substrate, as shown in Fig. 25. The integrated Aluminum bimorph¹⁸⁵ is allowing the extension of this research study to encounter a second driving excitation, which is beyond the scope of this work. Thus, the microcantilever is awarded an additional feature, next to being a self-registering (sensing) mechanism, and that is a self-actuating microprobe for future extension of this work.

Microfabrication of the cantilever-based biomechatronic sensor: microelectronic architecture

The system architecture of the miniaturized-biomechatronic-cantilever-based platform, Fig. 26, consists of a DC-Microbalance-ADC module and High Voltage Amplifier (Microsystems Ltd., Varna, Bulgaria), as well as a multifunction data acquisition card (National Instruments, Berkshire, UK), together with a transition printed circuit board (PCB) module, accommodating the microfabricated mechanical device. The DC-Microbalance-ADC module comprises a high precision, low-noise preamplifier and a supply of DC potential to the Wheatstone

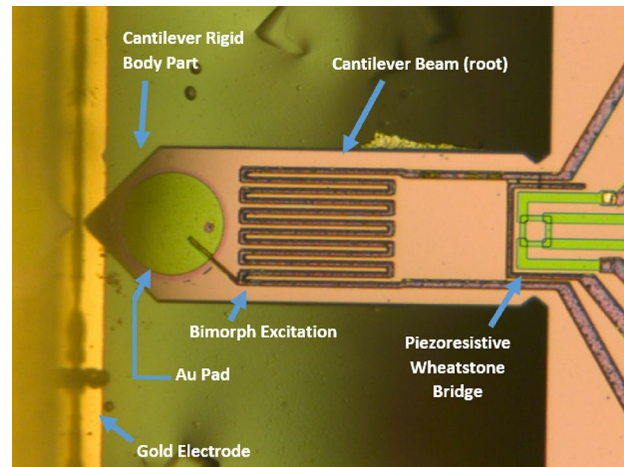


Fig. 25. A microscopic image of the miniaturized mechanical component of the biomechatronic platform featuring the microcantilever (root and rigid body), patterned gold electrode, Piezoresistive Wheatstone bridge, and bimorph excitation element for future extension of this research study.

bridge (1 V, 2 V, 4 V, and 4.5 V). It can operate in two channels, allowing two experiments to be conducted simultaneously.

In order to reduce electronic components within the voltage supplier source (design simplicity), as well as to eliminate the additional sources of electronic noises, the bridge supply of DC potential is set manually by a jumper, implying that the two channels would have the same feeding DC potential to the Wheatstone bridge piezoresistors. Moreover, two biomechatronic platforms can be connected directly, or via HDMI cables, to the DC-Microbalance-ADC module, where the former approach eliminates electronic noises experienced with long cable connections. The transition PCB design, housing the miniaturized biomechatronic platform, is in agreement with a prerequisite of the anticipated *in vitro* experiments, provisionally having a transparent space beneath the microfluidic chamber, allowing visual inspection under the microscope.

The high precision, low-noise preamplifier, with a fixed effective gain of 102, amplifies the output Wheatstone bridge voltage signal. The system bandwidth of 5 Hz allows obtaining up to 5 samples per second. The driving software allows collected data to be exported in a comma-separated-value (CSV) format, which eventually allows further data import to be widely processed by other software programs, e.g., Excel, MATLAB, etc., and subsequent averaging can be carried out. The built-in ADC signal module within the Microbalance unit allows further signal amplification and low-pass filtering. The signal processing is digitized through 24-bit resolutions for precise DC measurements.

The DC-Microbalance-ADC module has a bipolar input detection range that allows allocating high and low registered signals: $\pm 98 \mu\text{V}$, $\pm 196 \mu\text{V}$, $\pm 392 \mu\text{V}$, and $\pm 784 \mu\text{V}$. Furthermore, the module has a maximum effective resolution of $0.5 \mu\text{V}$ and a full-scale error of $\pm 0.01\%$. It has two digitally controlled offset compensation potentiometers (256 rough/fine steps for offset compensation); such a feature provides the voltage offset compensation due to the microfabrication tolerances experienced within the Wheatstone bridge piezoresistors. The digitized output from the built-in ADC is fed to the NI-DAQ card using a virtual serial peripheral interface (SPI) and then processed to the host PC.

On the other hand, the high voltage (HV) module receives a signal from NI-DAQ card, up to 1V, which is programmable from the PC software; then such signal is amplified via HV module to a maximum output of 75 V; therefore, this module will induce DC potential to the patterned gold electrode on the glass substrate via fabricated copper arms (spring probes), generating the electrostatic potential – investigating the static pull-in phenomenon to achieve high sensitivity in measurements^[92], which shall be an extension work beyond this paper's scope of work in measuring cellular mass (awarding the proposed bio-mechatronic platform versatility features). Figure 27 depicts the microelectronic setup in probing deflection(s) of a microcantilever due to an induced DC potential to the stationary gold electrode patterned on a glass substrate via an HV Amplifier module.

Microfabrication of the cantilever-based biomechatronic sensor: operating software

A DOE-oriented program, operating within two channels, has been customized and coded in DELPHI application programming language; it operates under Microsoft Windows and consists of three tabs: control panel (assigning experimental parameters), experiment execution tab, and data registry tab. The developed driving software allows the collection of data from two different experimental setups (two bio-mechatronic platforms operating in parallel). The software is connected to a NI-DAQ card, which controls two hardware modules: a DC-Microbalance-ADC module and a high voltage (HV) amplifier. First, the feeding potential value to the Wheatstone bridge has to be assigned in agreement with the manually set value in the DC-Microbalance-ADC module.

Both channels, having the same bridge supply of potential, can differ in terms of the imposed DC potential range that feeds the stationary gold electrode patterned on the glass substrate. Hence, having two channels running simultaneously, as shown in Fig. 28, shall provide flexibility to perform two different experiments in parallel, under two different conditions: analyzing two different biological phenomena at once; furthermore,

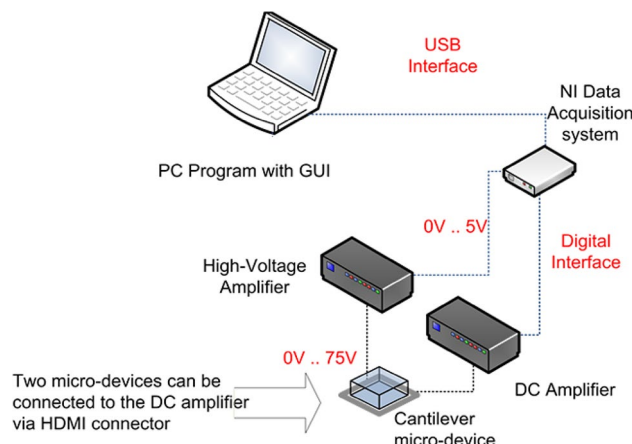


Fig. 26. Microelectronic hardware architecture of the microcantilever-based biomechatronic platform connected to a DC-Microbalance-ADC module and high voltage (HV) Amplifier. The system is connected to a PC to collect and analyze experimental data through an NI card.

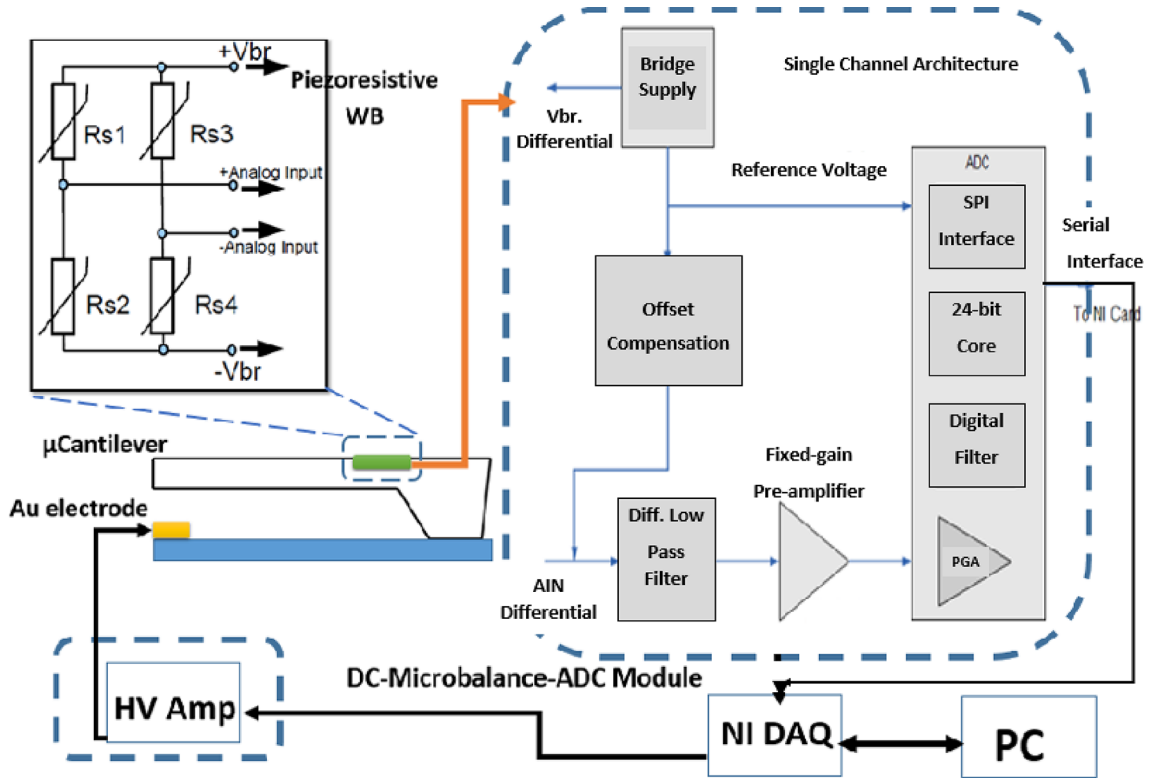


Fig. 27. Microelectronic setup in probing deflection(s) of a microcantilever due to an induced DC potential to the stationary gold electrode patterned on a glass substrate via an HV Amplifier module. The exploded view illustrates the Piezoresistive Wheatstone bridge (sensor scheme), where V_{br} is the manually selected voltage bridge. The DC-Microbalance-ADC module consists of an input differential filter, fixed-gain preamplifier, ADC with integrated programmable gain amplifier (PGA), bridge supply module, and offset compensation block.

having two experiments running at the same conditions in both channels shall investigate repeatability in the obtained results, shorten lead time, and enhance productivity in performing a number of experiments in one trial. Also, such a configuration can have one experimental setup through one channel running as a reference with respect to the other. The customized software also provides a wide variety of detection input ranges, allowing readings of minute changes experienced within the microcantilever kinematics throughout the *in vitro* experiments.

A crucial factor in microfabricating cantilevers is tolerance, where Wheatstone bridge resistors experience offset. Thus, the software is empowered with a feature to fine-tune the offset, alleviating tolerances to the vicinity of zero tolerance. Figure 29 illustrates a sample of registered data from one of the conducted trials.

In vitro experiments: materials and methods

As extensively addressed in Alqabandi¹⁴⁵ in terms of the merits associated with LoC and maintaining efficiency of the miniaturized device performance, the microfluidic chamber was first filled with DI water to remove any resultant debris within the miniaturized mechanical structure in an air-bubble-free environment, followed by a sterilization process carried out with ethanol for both microfluidic and cantilever; finally, a PBS wash was performed to enhance biocompatibility of the structure, and then system was left to dry.

As thoroughly described in Section “Cell culturing protocol and growth inhibition”, all cells were cultured as per the ATCC protocols. Cells were examined in Moxi z (ORFLO Technologies, WA, USA), a mini-automated-cell counter utilized to investigate the cell’s viability, volume, and size, as well as the cell’s concentration within a given fluid medium. The cantilever-based biomechatronic platform was filled with DI water to eliminate any resultant biological or microfabrication-related debris from the system. A sterilization process was performed with ethanol for the entire microdevice. At last, a PBS wash was carried out to improve the system’s biocompatibility, and then the platform was left to dry.

Two channels were operating throughout the *in vitro* experiments, where one channel with no-loaded mass was left as a reference. A number of trials have shown that the static potential, where the cantilever breaks, is within the 15-V range. More precisely, since the developed software source code is programmed such that the initialized command to the HV Amplifier module has a resolution increment of 1 V, the experimental static potential could be in the range exceeding 14 V but less than or equal to 15 V ($14V < V_{DC-breakage} \leq 15V$).

Keyence VHX-2000ES digital microscope (Keyence, Milton Keynes, UK) was employed to investigate the topography and heights of each cell line via the built-in change-of-focus mechanism featured in the Keyence

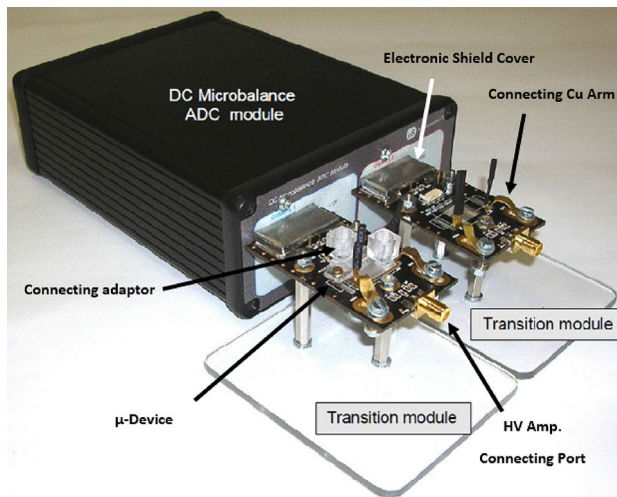


Fig. 28. DC-Microbalance-ADC module 2-channel configurations, showing two platforms (active and reference) with HV amplifier feeding port, microdevice, transition PCB module, and 2 connecting copper arms.

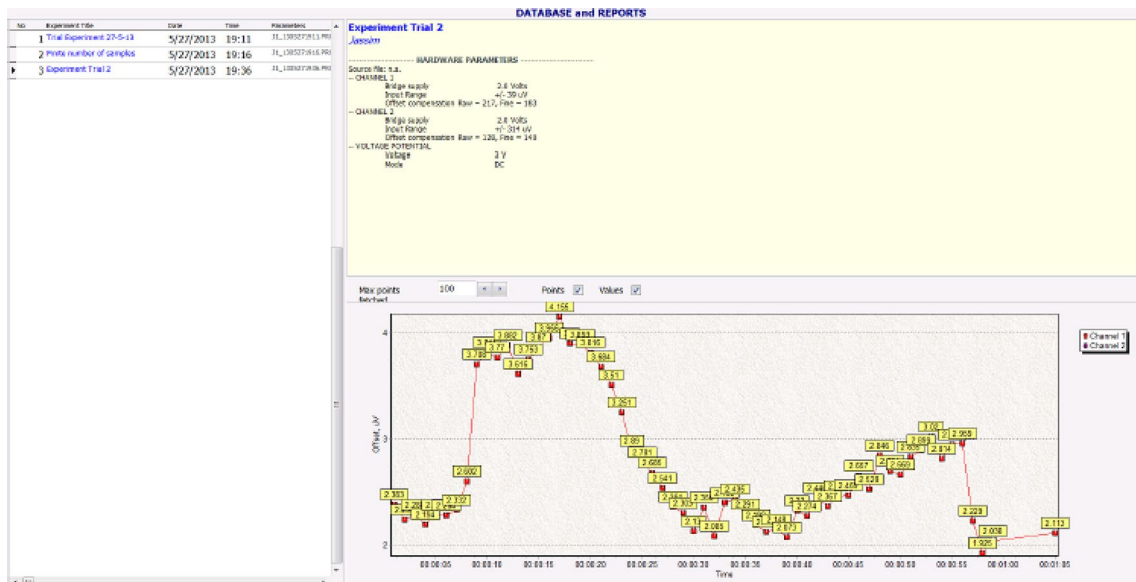


Fig. 29. Registered report of an in vitro trial experiment of the cantilever-based sensor.

microscope. A serial dilution approach was carried out as described in Section “[The biological model: the rationale behind the selection of the melanoma cell lines for the in vitro experiment](#)”, where the digital microscope was used to register the coordinate location of each viable cell within a culturing well, allowing flexibility in extracting a single cell via a micropipette. A trypan blue dye marker was applied to investigate the cell’s viability. The Keyence VHX-2000ES was employed through its change of focus mechanism to investigate the deflection of the tip of the beam and compare the results with the obtained deflections from the Wheatstone bridge reading. The results were in good agreement (~2%), which added confidence to the microfabricated cantilevers’ Piezoresistive elements in registering the deflection of the beam.

Scanning Electron Microscopy (SEM) was performed in a low vacuum chamber (avoiding cellular burst), where cells were fixed in 6% (w/v) paraformaldehyde (Sigma) for 25 min and washed in phosphate-buffered medium, whereas the typical protocol of dehydration, fixation, and gold sputtering was eliminated^[74]. SEM images of cells were obtained to investigate their morphology in terms of their heights and maximum contact surface area with a flat substrate.

The in vitro experiments were carried out under clean room conditions. Electromagnetic wave interferences were measured via an EMF meter and were found negligible (10^{-13} Tesla). The cell’s viability, concentration within a medium volume, diameter, and cellular volume were extracted via the Moxi Z device (ORFLO Technologies, WA, USA). The PCB connecting pads of the biomechatronic cantilever-based platform and

Wheatstone bridge piezoresistors were all examined via a multifunction multi-meter (MASTECH, Guangdong, China); investigating whether all transition lines were faithfully transferring signals, and the piezoresistors were damaged free. Furthermore, the copper arms were checked against a received signal initialized by the HV amplifier as pre-set in the customized software.

A single cell is extracted via a serial dilution process, as discussed in Section “[The biological model: the rationale behind the selection of the melanoma cell lines for the in vitro experiment](#)”, with registered locations via the VHX 2000 Keyence microscope coordinate control positioning registry algorithm (Keyence, Milton Keynes, UK). Furthermore, through the Keyence change focus lens mechanism, the air gap displacement between the tip portion of the microcantilever system (rigid body) and the patterned gold electrode on the glass substrate was found to be $\sim 4 \mu\text{m}$. Accordingly, the microcantilever is characterized to have a total length of $350 \mu\text{m}$, a width of $120 \mu\text{m}$, and a thickness of $\sim 3 \mu\text{m}$. The cantilever structure is mainly composed of silicon ($3 \mu\text{m}$) and $300 \text{ nm } SiO_2$, with a density of $2330 \frac{\text{kg}}{\text{m}^3}$, and modulus of elasticity (E) of 160 GPa ^{184–188}.

All microelectronic hardware was first connected, then the driving software was initialized. The software potentiometer capability was first utilized to account for the drift in the Piezoresistive tolerance. The experiments were conducted under clean room conditions. The entire experimental setup was placed on an anti-vibration table to avoid any vibrational noise entrances to the system, as shown in Fig. 30. The cantilever was housed inside a microfluidic module, which would eliminate any optical intervention to bend the miniaturized beam mechanical structure. Furthermore, a shield cover is used to insulate the microelectronic noises from entering the cantilever-based domain and to protect the underlying circuitry (e.g., wires, pads, etc.) from any electromagnetic emissions.

A single cell was extracted via serial dilution and re-examined for viability through a trypan blue dye marker. Then, it was loaded to the cantilever functionalized surface through the opening window on top of the microfluidic domain. The in vitro experiments were performed at the reference stage, where the cantilever was first in a non-deformed equilibrium configuration, followed by a loading cell stage. The cell would adhere to the functional gold pad near the tip of the cantilever. Finally, at the termination of the experiment stage, trypsin was utilized to detach cells from the cantilever functionalized surface, followed by DI water filling, sterilization, and PBS wash for miniaturized device reusability.

Two channels operated throughout the in vitro experiments, with one channel with no loaded mass left as a reference. All signals of the electronic connections were re-examined via a multimeter device. The experiments were performed on an anti-vibration table to eliminate any source of vibrational noises that might be induced in the measurement domain.

The measurements were recorded at various stages: biomechatronic platform without media and cell (stage 1), biomechatronic platform with media only (stage 2), and biomechatronic platform with media and cell (stage 3). This process allowed the arrival of distinctive cellular motility signals; furthermore, such methodology eliminated noises, and by using a triangle smoothing algorithm, the obtained voltage signals were easily read. A culturing and growth medium was added to the microfluidic chamber culturing reservoir inlet. A viable cell extracted from the serially diluted process was then loaded to the functional layer of the microcantilever via the opening window on top of the microfluidic domain. When a cell was loaded on the functional layer of the microcantilever, the cell got attached, and then adhered to the functional surface of the cantilever, and finally initiated motility signals at different time intervals were recorded, which varied from one cell line to the other.

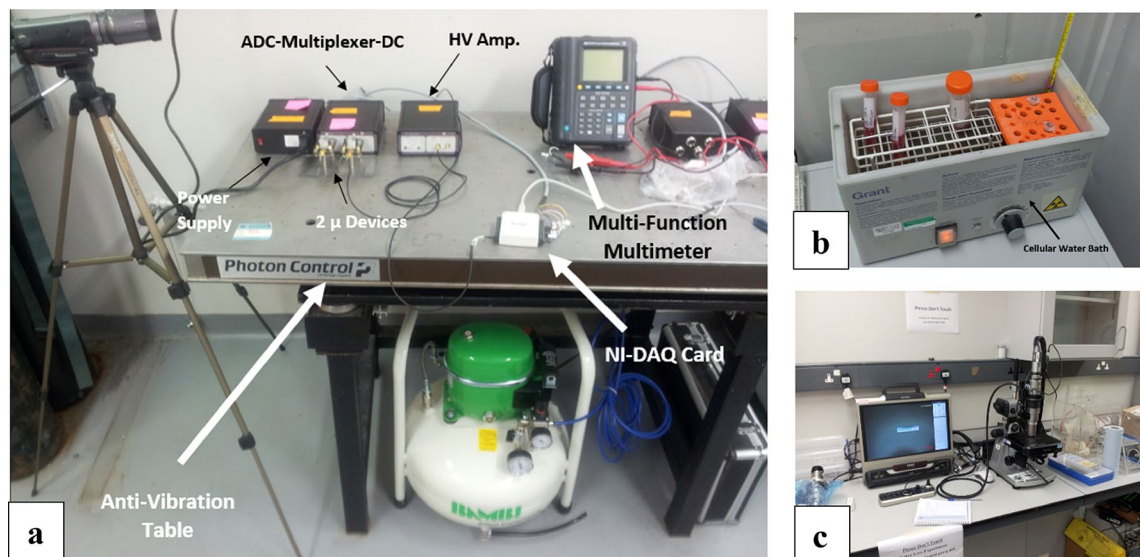


Fig. 30. Extracting cellular contractile force—in vitro experimental setup consisting of (a) an anti-vibration table, NI data acquisition card, ADC-Multiplexer-DC, HV Amplifier, power supply, and multi-function multimeter. (b) Cellular water bath to maintain a temperature of 37°C for cultured cells. (c) VHX-2000ES Keyence Digital Microscope.

Some cell lines within the microdevice were kept in incubators for one full day. At a final stage, trypsin was injected into the system to detach the cell from the cantilever functionalized surface, followed by DI water filling, sterilization, and PBS wash for miniaturized device reusability.

Extraction of contractile force in vitro experiments: results and discussions

Well-established-eight-melanoma cancer cell-line models of unique genetic complexities and genomic mutations have been investigated in terms of their morphologies, as well as their cellular contractile forces: SK-MEL-1, A-375, G-361, WM-115, NM-2C5, M-4A4, M4A4 LM3-4 CL16 GFP (CL 16), and M4A4 LM3-2 GFP (LM3). In addition, a well-documented breast cancer adenocarcinoma, MDA-MBA-231 (late metastasis), has been utilized as a calibration model when extracting the cellular contractile force, as a resultant correlation with the deflection of a microcantilever beam.

As the cell is loaded on the functional surface of the miniaturized cantilever, an ECM is developed between the cell and the cantilever's functional surface substrate. After that, the cell is adhered to, and then active polymerization and cellular AF-myosin motor (actomyosin) interaction contribute to the cell's motility. The experimental setup analyses in terms of the cantilever's bending due to electrostatic force have contributed significantly to allocating signals that correspond to a negative slope (bending downward), as opposed to signals associated with a positive slope due to cellular compressive surface stresses imposed on the cantilever functional surface (upward transverse deflection).

Before discussing the findings on cellular contractile forces at different stages of melanoma, morphology analyses were carried out using SEM and Keyence microscope. Cellular morphology has been evaluated in terms of steepness, which is in terms of height (thickness) and contact surface area. As in¹⁹³, it has been demonstrated experimentally that having a considerable contact surface area, where the cell is spreading over, shall advocate the cell's viability, growth, and motility. In contrast, a smaller area would lead to the cell's apoptosis. This is also in agreement with the premise of Alqabandi's work¹⁴⁵ – (LoC) ensures the exchange of oxygen and nutrients for cells and disposes of carbon dioxide from the system within a sufficient space to maintain cell viability. Figure 31 illustrates the depth compositions and 3D pattern configurations generated by the Keyence microscope, as well as SEM images of melanoma cells.

The morphology analyses aim to investigate cellular contact surface areas with flat substrates and cell heights; they also aim to examine the status of these two geometrical factors as cells differ in their heterogeneities (advancement in the stage of metastasis) in investigating the raised hypothesis.

The metastasis heterogeneity of the eight melanoma cell lines and breast adenocarcinoma cells (MDA-MB-231) have been thoroughly discussed in sections “[Cancer electrophysiology](#)” and “[Miniaturized-versatile-bioechatronic platform: quantifying the cell-membrane potential](#)”. Through SEM, microscopic depth composition analyses, and results obtained from Moxi Z, cell-line models have been characterized in terms of their average diameters, thicknesses (heights), and contact surface areas with the flat substrate. It has been noticed that cells' morphologies get steeper and steeper as the level of metastasis increases – cells spread more as they are at an advanced stage than if they were at an early one. The average cell's diameter gets comparatively larger and larger as cells advance from a non-metastatic stage toward a highly metastatic phase. On the contrary, the cells' average thickness (height) decreases as they progress in the metastatic stages. Accordingly, the cellular contact surface area with a flat substrate increases as cells progress throughout non-metastatic, early, intermediate, late, and highly metastatic stages. Table 9 summarizes the morphology characteristics of the different stages of melanoma cellular metastasis obtained in this work.

The obtained findings of cellular morphology confirm the viscoelastic characteristics of cells. As shown in Fig. 32, the morphology varies from stage to stage, as cells mostly experience a smooth round shape at the early stages of the metastasis, and then they elongate at late stages. Yin et al.¹⁹⁴ have developed high throughput imaging and computational methods in analyzing cells' morphologies, and they have investigated the role of subset genes in cellular configurations; they were successful in allocating a subset of genes, among them tumor suppressor gene PTEN, within human metastatic melanoma cells, which would provide a better understanding of the role of genes on defining cellular shape. They have categorized various cellular configurations: regular rounded, elongated, bipolar, spindle-shaped, small tear-drop shapes, large with smooth edges, and substantial flat cells of irregular/non-uniform edges.

Analyzing a cell's configurations, in conjunction with its associated contractile force, would significantly assist in understanding the metastatic aspect of the cancer disease pathogenesis, contributing to the cell's motilities and penetrations through other tissues and organs. Equations (47–50) are utilized to obtain the contractile force of a cell based on the voltage signals obtained from the Piezoresistive elements of the Wheatstone bridge. The numerical algorithm developed in Maple 16 (Maplesoft, Ontario, Canada) provides a solution for the compressive force generated in the cantilever with respect to the normalized deflection.

The contractile force of the well-documented cell-line model in literature, MDA-MB-231, is first measured and found to be $-3.29 \pm 1.57 \mu\text{N}$ (Mean \pm SD, $n=19$), which is within the range of magnitude of the published finding of the contractile force for this cell line in literature ($5 \mu\text{N}$)¹⁶⁶. The MDA-MB-231 cell-line model has been used as a calibration model, testing the reliability of the proposed microcantilever-based biomechatronic system. The discrepancy could be attributable to the constant changes in the viscoelastic form of the cell with time and the different mathematical approaches that had been pursued in arriving at the contractile force by considering the surface stress loading on the cantilever surface¹⁶⁶. However, the surface stress loading experienced by the beam accounts for all the compressive surface stresses exerted at the entire width and effective length of the beam. Therefore, in this study, the cellular contractile force is measured as per the area that the cell occupies, where the effective cellular compressive surface stresses are applied. This is achieved by utilizing the Heaviside step function¹⁸⁰.

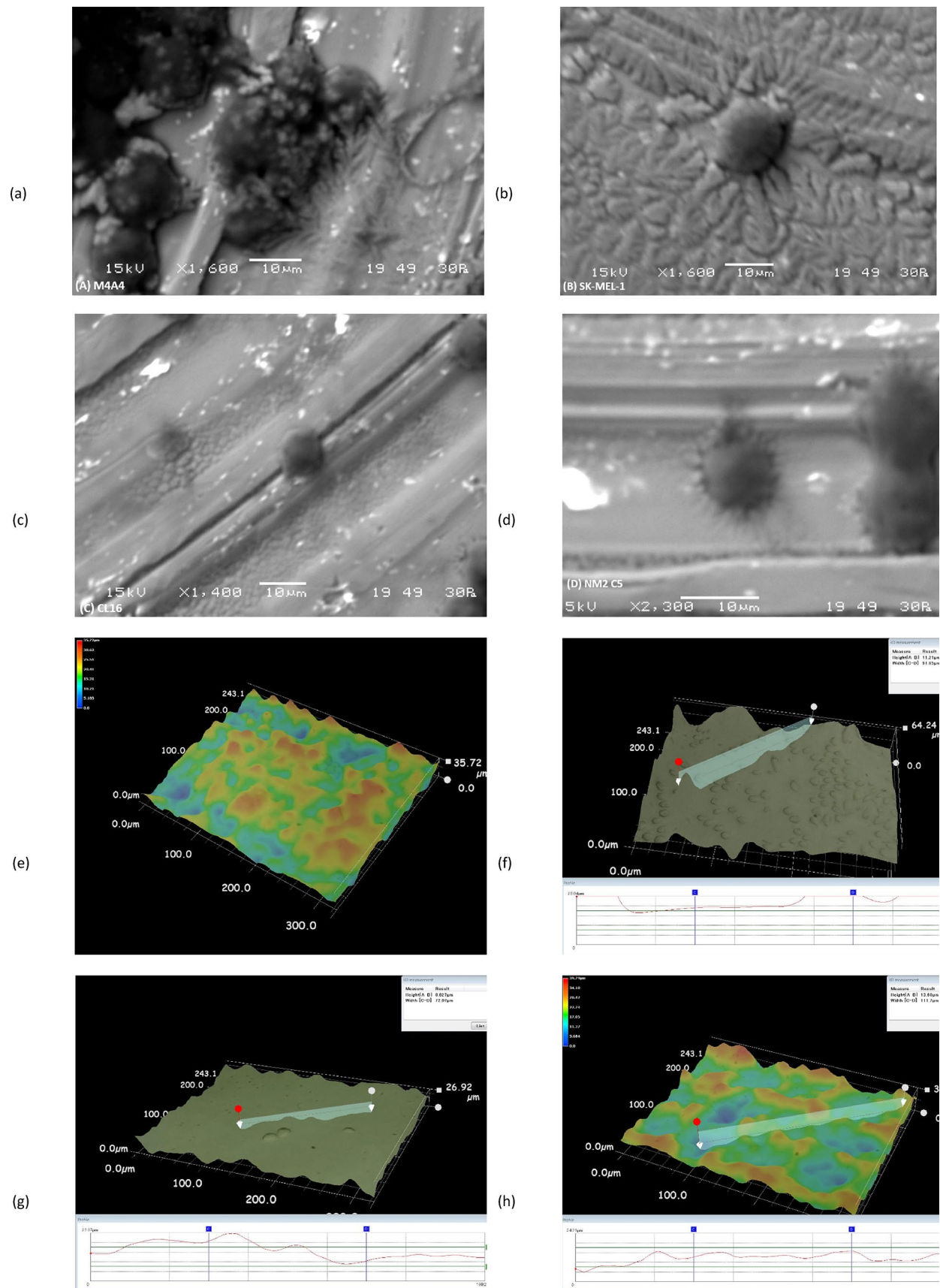
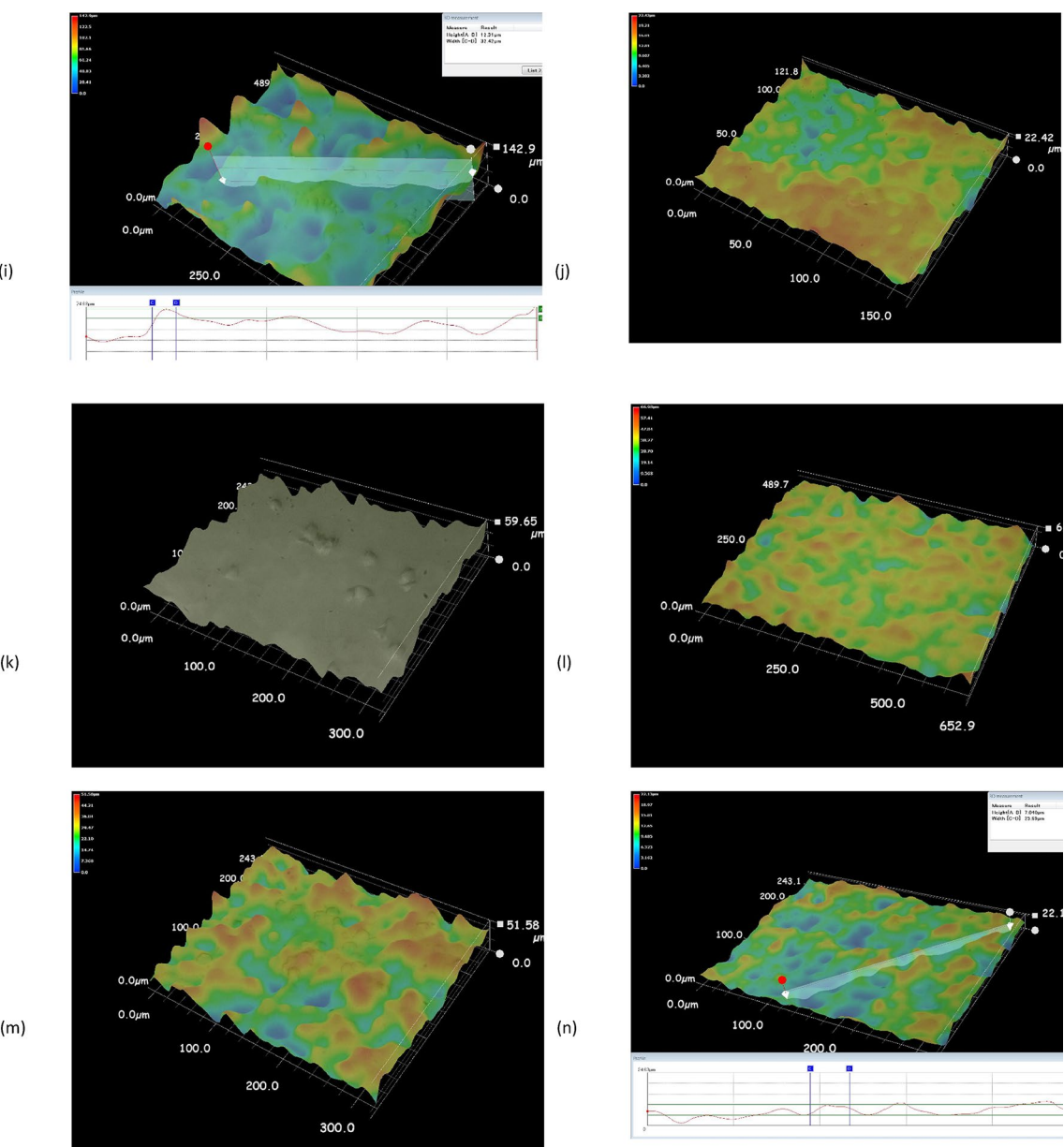


Fig. 31. SEM images of (a) M-4A4, (b) SK-MEL-1, (c) CL16, and (d) NM-2C5, as well as depth compositions and 3D pattern, generated microscopic images of (e) LM3, (f) A-375, (g) MDA-MB-231, (h) CL16, (I) NM-2C5, (j) MCF-7, (k) WM-115, (l) SK-MEL-1, (m) G-361, and (n) M-4A4.

**Figure 31.** (continued)

					Morph.
Non-Metastatic	Early Stage Metastasis	Intermediate Metastasis	Late Metastasis	Highly Metastasis	Stage
13.400 μm	17.2 μm	17.7 μm	19.80 μm	20.25 μm	d_{avg}
18.200 μm	16.4 μm	14.2 μm	11.21 μm	7.308 μm	t_c
0.141 nm^2	0.232 nm^2	0.246 nm^2	0.308 nm^2	0.322 nm^2	A_{avg}

Table 9. Based on this work's conducted in vitro experiments, different stages of melanoma metastasis and the two calibrating cancer cell line models were characterized based on their morphology image analyses using a Keyence VHX-2000ES digital microscope (Keyence, Milton Keynes, UK).

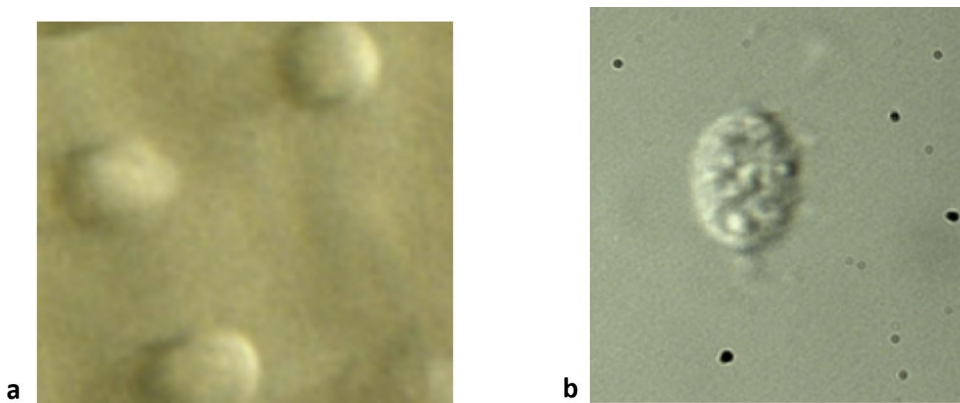


Fig. 32. SEM images of (a) Non-metastatic NM-2C5 smooth rounded morphology. (b) Elongated late invasive malignant melanoma, A-375.

Cell-line model	Level of metastasis	V_m (mV) (mean \pm SD)	n	F_C (μ N) (mean \pm SD)	n
MCF-7	Poorly invasive human breast adenocarcinoma	-43.96 ± 0.43	18	-0.266 ± 0.02	18
MDA-MB-231	Invasive-metastasis breast cancer	-25.78 ± 0.17	19	-3.290 ± 1.57	19
NM-2C5	Non-metastatic melanoma	-48.27 ± 3.08	26	-0.283 ± 0.03	26
M-4A4	Early-stage (weakly metastatic melanoma)	-42.50 ± 2.56	21	-0.362 ± 0.02	21
WM-115	Low-metastasis melanoma	-37.29 ± 2.11	19	-0.364 ± 0.02	19
G-361	Primary metastasis melanoma	-31.88 ± 1.67	20	-0.368 ± 0.02	20
SK-MEL-1	Primary metastasis melanoma	-27.84 ± 2.66	22	-0.371 ± 0.03	22
M4A4LM3-2GFP	Intermediate (moderately metastatic melanoma)	-27.28 ± 2.89	24	-0.454 ± 0.02	24
A-375	Late invasive malignant melanoma	-12.69 ± 2.79	23	-2.820 ± 0.24	23
M4A4LM3-4CL16 GFP	Highly Invasive metastasis melanoma	-4.324 ± 2.98	26	-4.833 ± 0.07	26

Table 10. Contractile force and respective cell-membrane potential of different stages of cancer-line models.

The obtained results of the contractile force of MDA-MB-231 have added confidence in the methodology pursued and the performance of the developed biomechatronic system. The contractile forces of the eight-melanoma-cancer-cell lines of different genomic mutations have been characterized and summarized in Table 10. It has been demonstrated that the higher the diameter of the cell, the higher the contractile force exerted on the cantilever surface. The negative sign of the obtained contractile force indicates the compressive force characteristic experienced by the cell during its migration, upon which cellular motility is invariant in time from one cell to the other. After cell attachment and reaching a steady state, the output voltage signal from the Piezoresistive elements of the Wheatstone bridge confirms that the beam has experienced a positive transverse deflection due to cell migration. It has been noted that the output voltage signal has increased considerably for the late and highly metastatic melanoma cell lines. However, it has been illustrated that there is a slight change between the early stage and intermediate in terms of contractile force magnitude.

As demonstrated in Table 10, the cellular contractile force of a cell increases as the cell advances in the metastatic stage—the cell is becoming more aggressive and invasive. Furthermore, in correlation with the obtained results of Section “The biological model: the rationale behind the selection of the melanoma cell lines for the *in vitro* experiment”, the increase of the contractile force accompanies a decrease in the magnitude of the associated cell-membrane potential. From the morphological analyses that flourished in this section, a cell becomes steeper; its contact surface area increases, and its thickness decreases if it is at a very late metastasis stage compared to an early one. Therefore, these experimental findings have investigated the raised hypothesis, demonstrating that as cells progress in the metastasis stages, they become more aggressive/invasive. Their motility and, eventually, their contractile forces increase. This would yield, on the other hand, a decrease in the cell-membrane potential magnitude. Furthermore, such an approach in extracting the cellular contractile force has successfully differentiated the degree of metastasis severity between the closely related G-361 and SK-MEL-1 primary metastasis cell lines.

As per the analyses carried out in Section “Discussion of the empirical results”, as cells ascend in the proliferation stage, their depolarized activities increase, resulting in excess of cytoplasm positivity of a cell, which is also interlinked to the increased activities of Na^+ ion channels^{43,45,47–49,130,136}. This could justify the highly active polymerization process experienced within advanced-stage cancerous cells as opposed to healthy ones that would yield cellular motility. However, this requires in-depth analyses of the oncogene mutation of these cell-line models, which would be the target of future extension of this work.

A theorem in carcinogenesis

The in-depth analyses of the obtained in vitro experimental findings have investigated and tested the raised hypothesis, which yields an approved theorem: "Jassim Al-Qabandi" Theorem—JQ Theorem. As manifested in Fig. 33, the in vitro experimental results are consistently repeatable with the same finding. The proposed theorem states that "as tumorigenesis progresses, which is an indication of an accumulated progression of genetic mutations within a cell, the magnitude of a cell-membrane potential drops, whereas the associated cellular contractile force ascents in magnitude, and the cellular morphogenesis becomes steeper. The contractile force is a resultant and dependent function of the electrophysiology of a cell variable that can be expressed as a polynomial, where the analytic function of contractile force yields a power series that starts with a first-order polynomial of cellular membrane potential, representing a non-metastatic stage and rises to the sixth-order polynomial, illustrating a highly invasive metastasis stage":

$$F_c(V_m) = \begin{cases} C_1 V_m + C_2 & \text{Non - Metastatic Stage} \\ C_1 V_m^2 + C_2 V_m + C_3 & \text{Early - Stage Melanoma} \\ C_1 V_m^3 + C_2 V_m + C_3 & \text{Low - Metastasis Melanoma} \\ C_1 V_m^3 + C_2 V_m^2 + C_3 V_m + C_4 & \text{Primary Metastasis Melanoma} \\ C_1 V_m^4 + C_2 V_m^3 + C_3 V_m^2 + C_4 V_m + C_5 & \text{Intermediate Metastasis Melanoma} \\ C_1 V_m^5 + C_2 V_m^4 + C_3 V_m^3 + C_4 V_m^2 + C_5 V_m + C_6 & \text{Late Invasive Malignant Melanoma} \\ C_1 V_m^6 + C_2 V_m^5 + C_3 V_m^4 + C_4 V_m^3 + C_5 V_m^2 + C_6 V_m + C_7 & \text{Highly Invasive Metastasis Melanoma} \end{cases} \quad (51)$$

where C_1, C_2, \dots, C_7 are constants, F_c is the contractile force, and V_m is the cell-membrane potential.

$$F_c(V_m) = \sum_{n=0}^5 C_{(n+1)} V_m^{(n+1)} + C_{(n+2)} \quad (52)$$

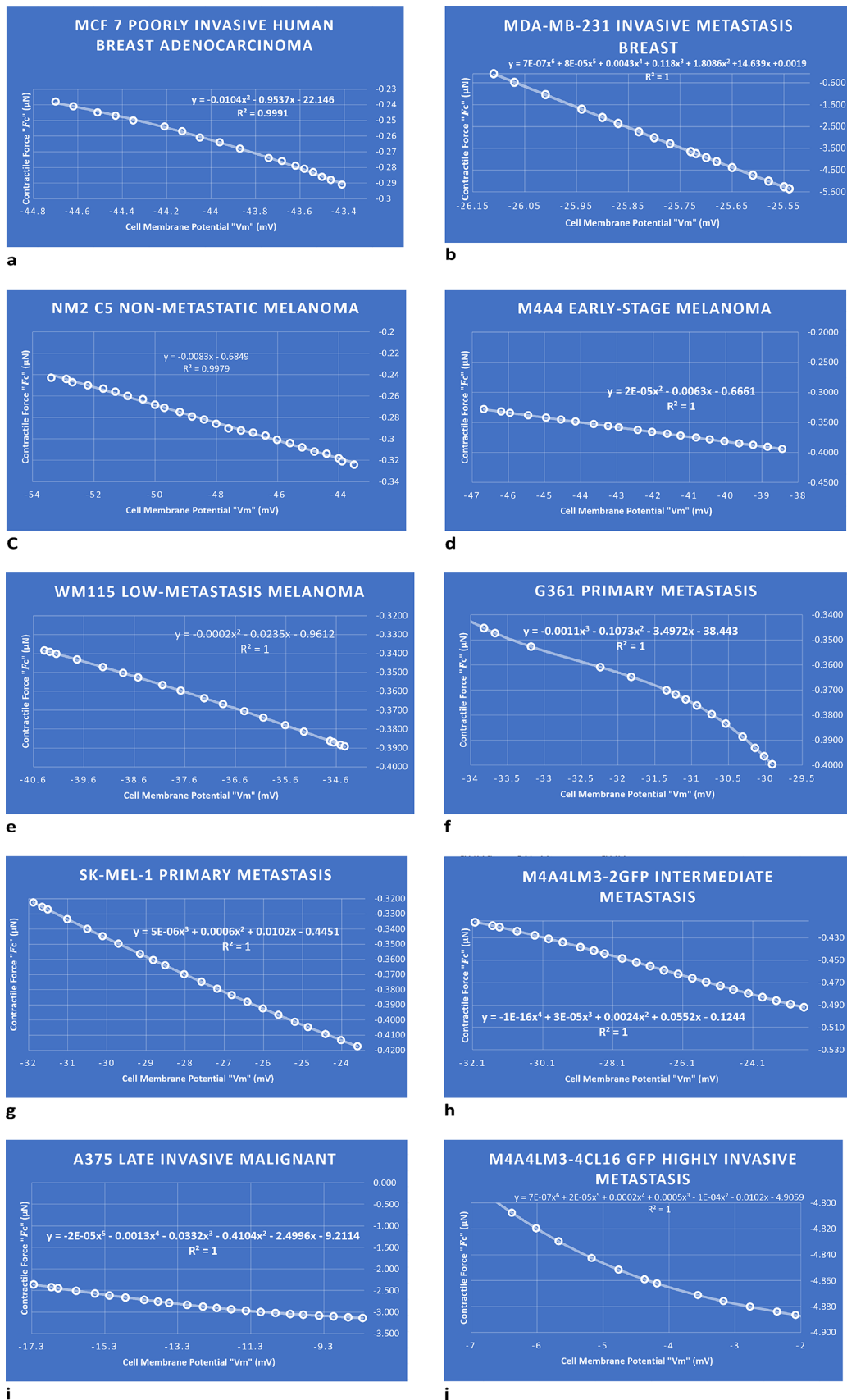
As clearly illustrated in Fig. 33, the in vitro experimental findings prove that the contractile force (F_c) is a function of the cell membrane potential (V_m) that can be depicted by a polynomial equation with a coefficient of determination (R^2) approaches unity; this suggests that the measurement of the proportion of variation in the dependent variable (F_c) is attributed to the independent variable (V_m). Furthermore, having a resultant coefficient of determination (R^2) equal to unity implies a perfective correlation in examining how differences in one variable (cell-membrane potential " V_m "), can be explained by the differences in a second variable (contractile force " F_c "), when predicting the outcome of extracting cells via biopsy from a patient. In other words, an oncologist can predict the progression of the disease stage based on the cell-membrane potential and statistically predict the associated contractile force without the need to experimentally extract the contractile force of the collected cells from a patient.

It's also found from the conducted experiments that early and low-metastasis stages are closely related and depicted by a second-order polynomial equation between cellular contractile force and its associated cell membrane potential. Furthermore, by examining the peer-reviewed calibrating cell-line model of MDA-MB-231 (invasive metastasis breast cancer) in terms of its contractile force and associated cell membrane potential, it is found to be depicted by a sixth-order polynomial, as in the invasive metastasis melanoma cancer type. Similarly, by comparing the poorly invasive human breast adenocarcinoma with low-metastasis and early-stage (weakly metastatic melanoma), they are depicted by a second-order polynomial. This suggests that the JQ theorem could be valid for different cell-line types, as distinctive cancer cell types shall be targeted for future extension of this work.

The proven theorem within this work can be further extended, given the high versatility of the two-customized biomechatronic platforms introduced in this paper, in measuring and analyzing another mechanobiology factor (cellular mass) in correlation with metastasis stage, as well as cell manipulation via the biophysics of cells for future works. Furthermore, this proposed theorem with the resulting mathematical equation can be coupled with other theorems, e.g., the Poisson theorem¹²³, Nernst–Plank equation^{120–122,124}, and/or the Hodgkin–Huxley cable model^{125–128}, to extend its applicability. Moreover, the microfabricated components of the iLoC (μ Fluidic module and MEAs) are based on a detailed investigation carried out by Alqabandi¹⁴⁵, such that the customized microfabricated devices introduced in this paper, mimicking, to some extent, in vivo environment in maintaining biocompatibility, cell's viability, and integrity throughout the conducted experiments.

The findings of the proposed JQ theorem based on the experimentally tested hypothesis in relating the biophysics of cancerous cells to the cellular contractile force and cell morphogenesis of different melanoma metastasis stages agree with the contributed analytical findings that flourished within this work. The steepness of cellular morphogenesis suggests a decrease in the cell's thickness and an increase in the cell's diameter as identified under the microscope (Figs. 31 and 32), eventually an increase in contact surface area, leading to invasive cellular motility to other tissues and organs (high contractile force). From a cellular mechanophenotyping perspective, metastatic cancer cells are identified to possess a smaller cell stiffness than healthy cells, enabling them to pass through ECM during the commencement of the metastatic process²⁷.

As depicted in the resultant empirical solution (Fig. 14), the drop in cell-membrane potential magnitude is a manifestation of depolarization that could be attributable to a reduction in the intracellular activities of K^+ ion, and/or an increase in the intracellular activities of Na^+ , when a cell ascends to the stage of tumorigenesis and its permeability increases, the rise in proliferation stage suggests an increase in the cellular depolarized activities, resulting in excess of cytoplasm positivity of a cell (a drop of the cell-membrane potential), which is also interlinked to increase activities of Na^+ ion channels. This confirms the highly active polymerization process experienced by advanced-stage cancerous cells as opposed to healthy ones, which yields cellular



motility—affirming, as per the conducted *in vitro* experiments, that the cellular contractile force is a function of cellular electrophysiology.

Fig. 33. Plots of the conducted in vitro experiments extracting cell membrane potential “Vm” in (mV) versus Cellular Contractile Force “Fc” in (μN) of various cell-line models at different stages: (a) Poorly Invasive Human Breast Adenocarcinoma, MCF-7. (b) Invasive-Metastasis Breast Cancer, MDA-MB-231. (c) Non-Metastatic Melanoma, NM-2C5. (d) Early-Stage (Weakly Metastatic), M-4A4. (e) Low-Metastasis Melanoma, WM-115. (f) Primary Metastasis Melanoma, G-361. (g) Primary Metastasis Melanoma, SK-MEL-1. (h) Intermediate (Moderately Metastatic), M4A4LM3-2GFP. (i) Late Invasive Malignant Melanoma, A-375. (j) Highly Invasive Metastasis Melanoma, M4A4LM3-4CL16 GFP.

Conclusions and future directions

Cancer is a very complex and ubiquitous life-threatening disease that requires multi-disciplinary efforts to characterize it well. This justifies the multidisciplinary research backgrounds of the authors in advancing cellular medicine by bridging the gap between experimental biology and the engineering field. Thus, this paper aimed to explicitly address all overlapped topics to the novice readers by presenting the detailed derivations of the analytical and empirical solutions of cellular biophysics and mechanobiology, flourishing detailed nano/microfabrication processes of the biomechatronic platforms, illustrating the dedicated software development and microelectronics, presenting an overview of cancer biology powered by movie presentations and animated movies, as well as cell culturing and flourishing the steps in conducting the in vitro experiments.

In this work, two novel, highly versatile biomechatronic platforms have been designed, modeled, and further developed to characterize the electrophysiology and mechanobiology of cells. Dedicated microelectronics and customized software have been attained to functionalize and empower the two biomechatronic systems. Furthermore, detailed microfabrication processes are illustrated to construct the miniaturized mechanical components of the biomechatronic platforms. A number of in vitro experiments were conducted to extract the cell-membrane potential and cellular contractile force. The first biomechatronic platform consists of a microfluidic and MEAs module to characterize the biophysics of cells. On the other hand, the second platform of a microcantilever base with an embedded Piezoresistive Wheatstone bridge and microfluidic module is utilized to quantify the contractile forces of cells.

Various well-characterized melanoma cancer cell lines, with varying degrees of genetic complexities, have been utilized: SK-MEL-1 (primary malignant metastatic melanoma), A-375 (late invasive malignant melanoma), G-361 (primary malignant melanoma), WM-115 (low metastasis melanoma), NM-2C5 (weakly/virtually non-metastatic melanoma), M-4A4 (early stage metastatic), M4A4 LM3-2 GFP (intermediate stage second lung metastasis), and M4A4 LM3-4 CL16 GFP (highly metastatic third generation lung metastasis). In addition, well-documented cell models within the literature, breast cancer adenocarcinoma human (*homo sapiens* MDA-MB-231), and early-stage breast cancer (MCF-7) have been used as calibration-cell models for the microfabricated biomechatronic platforms based on extracted cell-membrane potential and contractile force.

Contractile force is mainly responsible for cell motility and is initiated by cell signaling, where cell-membrane potential plays a dominant role in instructing cells to mobilize via electrochemical signals. This study concluded that the cell contractile force increases as cancer cells progress to ascending metastatic stages (healthy to late metastasis). At the same time, its associated cell-membrane potential decreases in magnitude, and its morphology gets steeper (higher surface contact area and lower cellular height).

The raised hypothesis has been thoroughly tested and yielded a proven theorem in carcinogenesis by interrelating cellular contractile force, membrane potential, and cellular morphology via the utilization of novel miniaturized and highly versatile biomechatronic platforms for early detection and characterization of melanoma cancer cells. The novelties flourished within this work are manifested in (1) developing a mathematical model that utilizes a Heaviside step function, as well as a pin-force model to compute the contractile force of a living cell, (2) deriving an expression of cell-membrane potential based on Laplace and Fourier Transform and their Inverse Transform functions by encountering Warburg diffusion impedance factor, (3) microfabricating novel biomechatronic platforms with associated microelectronics and customized software that extract cellular physics and mechanics, (4) developing a label-free biomarker, (5) to the first time in literature, and to the best of the authors’ knowledge, discriminating different stages and morphology of cancer cell melanoma based on their cell-membrane potentials, and associated contractile forces.

Such versatile bio-mechatronic platforms could be utilized in various fields, such as cardiology, immunotherapy, astrobiology, and biophysics. Accordingly, in addition to the investigated applications of the developed biomechatronic platforms within this paper, the fabricated miniaturized devices are designed and developed to be highly versatile; therefore, this could easily extend the work within this research to perform cell manipulation, facilitate in vitro stem-cell proliferation, identify cell signal propagation, and examine cell-cell communication via electrical means through MEAs patterned on glass substrate. Furthermore, the microfluidic chamber will be enhanced to provide an optimal environment for cell incubation throughout the experiment based on the requirements of cell’s viability illustrated in Alqabandi¹⁴⁵. Furthermore, the effective functional layer of the microcantilever will be coated to analyze the antibody/antigen binding mechanism and correlate the mechanical deflection of the beam to the identification of a vaccine based on such binding that would be of great asset within the immunology field. Finally, driven by the work of Nayfeh et al.¹⁹⁵, the claimed enhancement of the sensitivity of the miniaturized deflection of the beam by injecting harmonic AC potential superimposed to a static DC voltage will be investigated experimentally to obtain a highly sensitive bio-mass sensor.

To comprehensively conclude the findings of this research in drawing the correlations among electrophysiology, morphology, and contractile forces of cells, this research study will be extended to investigate and discuss the interrelation of oncogenes’ mutations within each stage of melanoma cells experiencing different metastases,

which are mainly responsible about melanoma cells' motilities. Two oncogenes are of great interest to examine: JAK and STAT3^{75,196–198}.

The Janus Kinase (JAK) family of non-receptor tyrosine kinases (NRTKs) is responsible for actomyosin contractility force for cell migration¹⁹⁶. STAT3 is a downstream signal transduction resulting from the activation of JAK^{196,197}. STAT3 is part of the signal transducer and activator transcription 3 family, and it plays a significant role in cell motility, immune response, anti-apoptosis, and proliferation¹⁹⁸. It is also believed that JAK/STAT preserves tumorigenesis and, at some events, stimulates tumor angiogenesis⁷⁵. Thus, inhabitation of the JAK/STAT signal pathway could arrest cellular mitosis and thus prevent cancer from invading tissues and other organs.

An immune assay approach shall be utilized to investigate the role of JAK/STAT on the proposed 8 melanoma-cell lines' motilities by measuring their activities, functions, inhibitions, and knockdowns. A proposed ELISA assay (eBioscience, SD, USA) will be utilized in future extensions of this work to capture the phosphorylated human STAT3 within cell lysates. The STAT3 activity will be correlated to the extracted electrophysiology of the melanoma cell and its associated contractile force measurement.

Another extension of this work is to utilize the constructed bio-mechatronic platforms proposed in this paper to mimic nervous system-cancer interactions within in vitro microenvironments. This pioneering field of cancer neuroscience investigates the role of electrochemical signaling of the nervous system in cancer formation, which will significantly impact modern oncology pursuing a targeted immunotherapy approach. This work provides a robust platform for immunotherapy practitioners in extending the study of cellular biophysics in stalling neural-cancer interactions, of which the FDA-approved chimeric antigen receptor (CAR)-T cell therapies can be enhanced (genetically engineered) in a lab by improving its receptors to capture cancer antigens^{199,200}. It has been found that CAR-T cell therapy is associated with complications and a negative impact on the nervous system that can lead to nausea, fatigue, seizures, tremors, and so forth^{201,202}. This amplifies the importance of studying neurotransmitters and electrochemical signaling molecules in shaping the immune T-cell function and its effectiveness in arresting cancer proliferation rate^{203–205}.

Data availability

The datasets used and/or analysed during the current study available from the corresponding author on reasonable request.

Received: 14 February 2024; Accepted: 6 November 2024

Published online: 03 December 2024

References

- Mancusi, R. & Monje, M. The neuroscience of cancer. *Nature* **618**, 467–481 (2023).
- Alqabandi, J., Abdul Mottal, U. & Youcef-Toumi, K. Extracting cancer cell line electrochemical parameters at the single cell level using a microfabricated device. *Biotechnol. J.* **4**, 216–223 (2009).
- Choi, Y. E., Kwak, J. W. & Park, J. W. Nanotechnology for early cancer detection. *Sensors* **10**, 428–455 (2010).
- Ferrari, M. Cancer Nanotechnology: Opportunities and challenges. *Nat. Rev.* **5**, 161–171 (2005).
- Datar, R. et al. Cantilever sensors: nanomechanical tools for diagnostics. *MRS Bull.* **34**, 449–454 (2009).
- Kim, S. K. et al. Assessment of lymph node metastases using 18F-FDG PET in patients with advanced gastric cancer. *Eur. J. Nucl. Med. Mol. Imaging* **33**, 148–155 (2006).
- Trojan, J. et al. Fluorine-18 FDG positron emission tomography for imaging of hepatocellular carcinoma. *Off. J. Am. Coll. Gastroenterol.* **94**, 3314–3319 (1999).
- Kitajima, K. et al. Accuracy of 18F-FDG PET/CT in detecting pelvic and paraaortic lymph node metastasis in patients with endometrial cancer. *Am. J. Roentgenol.* **190**, 1652–1658 (2008).
- Kinkel, K., Lu, Y., Both, M., Warren, R. S. & Thoeni, R. F. Detection of hepatic metastases from cancers of the gastrointestinal tract by using noninvasive imaging methods (US, CT, MR Imaging, PET): a meta-analysis. *Radiology* **224**, 748–756 (2002).
- Bonomo, L., Ciccotosto, C., Guidotti, A. & Storto, M. L. Lung cancer staging: The role of computed tomography and magnetic resonance imaging. *Eur. J. Radiol.* **23**, 35–45 (1996).
- Pisano, E. D. et al. Diagnostic performance of digital versus film mammography for breast-cancer screening. *N. Engl. J. Med.* **353**, 1773–1783 (2005).
- Deguchi, T. et al. Detection of micrometastatic prostate cancer cells in the bone marrow of patients with prostate cancer. *Br. J. Cancer* **75**, 634–638 (1997).
- Salomon, G. et al. Evaluation of prostate cancer detection with ultrasound real-time elastography: A comparison with step section pathological analysis after radical prostatectomy. *Eur. Urol.* **54**, 1354–1362 (2008).
- Hamaoka, T., Madewell, J. E., Podoloff, D. A., Hortobagyi, G. N. & Ueno, N. T. Bone imaging in metastatic breast cancer. *J. Clin. Oncol.* **22**, 2942–2953 (2004).
- Robbins, E. Radiation risks from imaging studies in children with cancer. *Pediatr. Blood Cancer* **51**, 453–457 (2008).
- Gimbel, J. R. & Kanal, E. Can patients with implantable pacemakers safely undergo magnetic resonance imaging? *J. Am. Coll. Cardiol. Found.* **43**, 1325–1327 (2004).
- Teissl, C., Kremsner, C., Hochmair-Desoyer, I. J. Magnetic resonance imaging and cochlear implants: Compatibility and safety aspects. *J. Magn. Reson. Imaging Off. J. Int. Soc. Magn. Reson. Med.* **9**, 26–38 (1999).
- Lotan, Y. & Roehrborn, C. G. Sensitivity and specificity of commonly available bladder tumor markers versus cytology: Results of a comprehensive literature review and meta-analyses. *Urology* **61**, 109–118 (2003).
- Suresh, S. Biomechanics and biophysics of cancer cells. *Acta Biomater.* **3**, 413–438 (2007).
- Zhou, Y. et al. Label-free detection of p53 antibody using a microcantilever biosensor with piezoresistive readout. In *SENSORS* IEEE 819–822 (2009).
- Graeber, T. G. et al. Hypoxia-mediated selection of cells with diminished apoptotic potential in solid tumors. *Nature* **379**, 88–91 (1996).
- Pellman, D. Cell biology: Aneuploidy and cancer. *Nature* **446**, 38–39 (2007).
- Laird, D. W. The gap junction proteome and its relationship to disease. *Trends Cell Biol.* **20**, 92–101 (2010).
- Lodish, H. et al. Photosynthetic stages and light-absorbing pigments. In *Molecular Cell Biology* 4th edn (ed. Lodish, H. F.) (WH Freeman, 2000).
- Sims, C. E. & Allbritton, N. L. Analysis of single mammalian cells on-chip. *Lab Chip* **7**, 423–440 (2007).

26. Kraus, T. et al. Characterization of a microfluidic dispensing system for localised stimulation of cellular networks. *Lab Chip* **6**, 218–229 (2006).
27. Nakamura, M., Ono, D. & Sugita, S. Mechanophenotyping of B16 melanoma cell variants for the assessment of the efficacy of (-)-epigallocatechin gallate treatment using a tapered microfluidic device. *Micromachines* **10**, 207 (2019).
28. Huang, X. et al. Effect of dacarbazine on CD44 in live melanoma cells as measured by atomic force microscopy-based nanoscopy. *Int. J. Nanomed.* **12**, 8867–8886 (2017).
29. Ashmore, J. F. A fast motile response in guinea-pig outer hair cells: The cellular basis of the cochlear amplifier. *J. Physiol.* **388**, 323–347 (1987).
30. Yang, D., Welm, A. & Bishop, J. M. Cell division and cell survival in the absence of surviving. *Proc. Natl. Acad. Sci.* **101**, 15100–15105 (2004).
31. Kim, H. S. et al. Metastasis of hepatocellular carcinoma to the small bowel manifested by intussusception. *World J. Gastroenterol.* **WJG** **12**, 1969–1971 (2006).
32. Mihaljevic, A. L., Michalski, C. W., Friess, H. & Kleeff, J. Molecular mechanism of pancreatic cancer—Understanding proliferation, invasion, and metastasis. *Langenbeck's Arch. Surg.* **395**, 295–308 (2010).
33. Zarghooni, M. et al. Whole-genome profiling of pediatric diffuse intrinsic pontine gliomas highlights platelet-derived growth factor receptor α and poly (ADP-ribose) polymerase as potential therapeutic targets. *J. Clin. Oncol.* **28**, 1337–1344 (2010).
34. Meyvantsson, I. & Beebe, D. J. Cell culture models in microfluidic systems. *Annu. Rev. Anal. Chem.* **1**, 423–449 (2008).
35. Turner, N. & Grose, R. Fibroblast growth factor signalling: from development to cancer. *Nat. Rev. Cancer* **10**, 116–129 (2010).
36. Feldmann, G. et al. Inhibiting the cyclin-dependent kinase CDK5 blocks pancreatic cancer formation and progression through the suppression of Ras-Ral signaling. *Cancer Res.* **70**, 4460–4469 (2010).
37. Mezzanica, D., Canevari, S., Cecco, L. D. & Bagnoli, M. miRNA control of apoptotic programs: Focus on ovarian cancer. *Expert Rev. Mol. Diagn.* **11**, 277–286 (2011).
38. Fragoso, A. et al. Integrated microfluidic platform for the electrochemical detection of breast cancer markers in patient serum samples. *Lab Chip* **11**, 625–631 (2011).
39. Sundelacruz, S., Levin, M. & Kaplan, D. L. Role of membrane potential in the regulation of cell proliferation and differentiation. *Stem Cell Rev. Rep.* **5**, 231–246 (2009).
40. Cross, J. D. & Craighead, H. G. Micro-and nanofluidics for biological separations. In *CMOS Biotechnology* (eds Lee, H. et al.) 31–75 (Springer, 2007).
41. Brown, G. C. *The Energy of Life: The Science of What Makes Our Minds and Bodies Work* (Free Press, 1999).
42. Reilly, J. P. *Applied Bioelectricity: From Electrical Stimulation to Electropathology* (Springer Science & Business Media, 1998).
43. Marmo, A. A., Morris, D. M., Schwalke, M. A., Iliev, I. G. & Rogers, S. Electrical potential measurements in human breast cancer and benign lesions. *Tumor Biol.* **15**, 147–152 (1994).
44. Dorland, W. *Dorland's Medical Dictionary for Health Consumers* (Saunders, an imprint of Elsevier, 2007).
45. Cone, C. D. Jr & Tongier, M. Jr. Control of somatic cell mitosis by simulated changes in the transmembrane potential level. *Oncology* **25**, 168–182 (1971).
46. Schaefer, A. E., Hempling, H. G., Handler, E. E. & Handler, E. S. Measurement of the electrical potential difference and the distribution of ions in the Shay chloroleukemic tumor cell. *Cancer Res.* **32**, 1170–1176 (1972).
47. Marino, A. A. et al. Association between cell membrane potential and breast cancer. *Tumor Biol.* **15**, 82–89 (1994).
48. Sun, D. et al. Increasing cell membrane potential and GABAergic activity inhibits malignant hepatocyte growth. *Am. J. Physiol. Gastrointest. Liver Physiol.* **285**, 12–19 (2003).
49. Pancrazio, J. J., Viglione, M. P., Tabbara, I. A. & Kim, Y. I. Voltage-dependent ion channels in small-cell lung cancer cells. *Cancer Res.* **49**, 5901–5906 (1989).
50. Ashcroft, F. M. *Ion Channels and Disease* (Academic Press, 2000).
51. Nordenström, B. E. *Biologically Closed Electric Circuits: Clinical, Experimental and Theoretical Evidence for an Additional Circulatory System* (Nordic Medical Publications, 1983).
52. Pekar, R. & Ruzicka, F. *Percutaneous Bio-Electrotherapy of Cancerous Tumours: A Documentation of basic Principles and Experiences with Bio-Electrotherapy* (Wilhelm Maudrich, 1997).
53. Chou, C. K. et al. Development of electrochemical treatment at the city of hope. In *Electricity and Magnetism in Biology and Medicine* (ed. Bersani, F.) 927–930 (Springer, Berlin, 1997).
54. O'Clock, G. D. Evidence and necessity for biologically closed electric circuits (BCEC) in healing, regulation and oncology. *Dtsch. Z. Onkol.* **33**, 77–84. <https://doi.org/10.1055/s-2001-19444> (2001).
55. Li, K. H. et al. Effects of direct current on dog liver: Possible mechanisms for tumor electrochemical treatment. *Bioelectromagnetics J. Bioelectromagn. Soc. Soc. Phys. Regul. Biol. Med. Eur. Bioelectromagn. Assoc.* **18**, 2–7 (1997).
56. Hope, T. A. & Iles, S. E. Technology review: The use of electrical impedance scanning in the detection of breast cancer. *Breast Cancer Res.* **6**, 1–6 (2004).
57. Han, A., Yang, L. & Frazier, A. B. Quantification of the heterogeneity in breast cancer cell lines using whole-cell impedance spectroscopy. *Clin. Cancer Res.* **13**, 139–143 (2007).
58. Yun, Y., Dong, Z., Shanov, V. N. & Schulz, M. J. Electrochemical impedance measurement of prostate cancer cells using carbon nanotube array electrodes in a microfluidic channel. *Nanotechnology* **18**, 465505 (2007).
59. Qiao, G., Duan, W., Chatwin, C., Sinclair, A. & Wang, W. Electrical properties of breast cancer cells from impedance measurement of cell suspensions. In *Journal of Physics: Conference series*, Vol. **224** 012081 (2010).
60. Surowiec, A. J., Stuchly, S. S., Barr, J. R. & Swarup, A. A. S. A. Dielectric properties of breast carcinoma and the surrounding tissues. *IEEE Trans. Biomed. Eng.* **35**, 257–263 (1988).
61. Morimoto, T. et al. Measurement of the electrical bio-impedance of breast tumors. *Eur. Surg. Res.* **22**, 86–92 (1990).
62. Chauveau, N. et al. Ex vivo discrimination between normal and pathological tissues in human breast surgical biopsies using bioimpedance spectroscopy. *Ann. N. Y. Acad. Sci.* **873**, 42–50 (1999).
63. Ananthakrishnan, R. & Ehrlicher, A. The forces behind cell movement. *Int. J. Biol. Sci.* **3**, 303–317 (2007).
64. Bao, G. & Suresh, S. Cell and molecular mechanics of biological materials. *Nat. Mater.* **2**, 715–725 (2003).
65. Quill, T. A., Wang, D. & Garbers, D. L. Insights into sperm cell motility signaling through sNHE and the CatSpers. *Mol. Cell. Endocrinol.* **250**, 84–92 (2006).
66. Olson, M. F. & Sahai, E. The actin cytoskeleton in cancer cell motility. *Clin. Exp. Metastasis* **26**, 273–287 (2009).
67. Turner, L., Ryu, W. S. & Berg, H. C. Real-time imaging of fluorescent flagellar filaments. *J. Bacteriol.* **182**, 2793–2801 (2000).
68. Eyckmans, J., Boudou, T., Yu, X. & Chen, C. S. A hitchhiker's guide to mechanobiology. *Dev. Cell* **21**, 35–47 (2011).
69. Van Zijl, F., Krupitza, G. & Miklits, W. Initial steps of metastasis: cell invasion and endothelial transmigration. *Mutat. Res. Rev. Mutat. Res.* **728**, 23–34 (2011).
70. Sibley, L. D., Häkansson, S. & Carruthers, V. B. Gliding motility: An efficient mechanism for cell penetration. *Curr. Biol.* **8**, R12–R14 (1998).
71. Alberts, B. et al. *Molecular Biology of the Cell* (Garland Science Press, 2002).
72. Li, W. et al. Extracellular heat shock protein-90 α : Linking hypoxia to skin cell motility and wound healing. *EMBO J.* **26**, 1221–1233 (2007).
73. Fung, Y. C. *Biomechanics: Mechanical Properties of Living Tissues* (Springer Science & Business Media, 2013).

74. Park, J. et al. Real-time measurement of the contractile forces of self-organized cardiomyocytes on hybrid biopolymer microcantilevers **77**, 6571–6580 (2005).
75. Chen, M. H., Kerkelä, R. & Force, T. Mechanisms of cardiac dysfunction associated with tyrosine kinase inhibitor cancer therapeutics. *Circulation* **118**, 84–95 (2008).
76. Wilhelm, I., Molnár, J., Fazakas, C., Haskó, J. & Krizbai, I. A. Role of the blood-brain barrier in the formation of brain metastases. *Int. J. Mol. Sci.* **14**, 1383–1411 (2013).
77. Mierke, C. T., Rösel, D., Fabry, B. & Brábek, J. Contractile forces in tumor cell migration. *Eur. J. Cell Biol.* **87**, 669–676 (2008).
78. Sahai, E. Mechanisms of cancer cell invasion. *Curr. Opin. Genet. Dev.* **15**, 87–96 (2005).
79. Euteneuer, U. & Schliwa, M. The function of microtubules in directional cell movement. *Ann. N. Y. Acad. Sci.* **466**, 867–886 (1986).
80. American Cancer Society. *Cancer Facts & Figures* (American Cancer Society, 2010).
81. Wright, C. J. E. Prognosis in cutaneous and ocular malignant melanoma: A study of 222 cases. *J. Pathol. Bacteriol.* **61**, 507–525 (1949).
82. Kioi, M. et al. Inhibition of vasculogenesis, but not angiogenesis, prevents the recurrence of glioblastoma after irradiation in mice. *J. Clin. Investig.* **120**, 694–705 (2010).
83. Wang, B. et al. E-cadherin expression is regulated by miR-192/215 by a mechanism that is independent of the profibrotic effects of transforming growth factor-β. *Diabetes* **59**, 1794–1802 (2010).
84. Folkman, J. The vascularization of tumors. *Sci. Am.* **234**, 58–64 (1976).
85. American Cancer Society. *Cancer Facts & Figures* (American Cancer Society, 2023).
86. Li, H., Han, Y., Guo, Q., Zhang, M. & Cao, X. Cancer-expanded myeloid-derived suppressor cells induce anergy of NK cells through membrane-bound TGF-β1. *J. Immunol.* **182**, 240–249 (2009).
87. Schatton, T. et al. Identification of cells initiating human melanomas. *Nature* **451**, 345–349 (2008).
88. Naik, P. P. Cutaneous malignant melanoma: A review of early diagnosis and management. *World J. Oncol.* **12**, 7–19 (2021).
89. Darmawan, C. C. et al. Early detection of acral melanoma: A review of clinical, dermoscopic, histopathologic, and molecular characteristics. *J. Am. Acad. Dermatol.* **81**, 805–812 (2019).
90. Psaty, E. L., Scope, A., Halpern, A. C. & Marghoob, A. A. Defining the patient at high risk for melanoma. *Int. J. Dermatol.* **49**, 362–376 (2010).
91. Petrie, T., Samatham, R., Witkowski, A. M., Esteva, A. & Leachman, S. A. Melanoma early detection: Big data, bigger picture. *J. Investig. Dermatol.* **139**, 25–30 (2019).
92. Nascimento, J. C. & Marques, J. S. Improved gradient vector flow for robust shape estimation in medical imaging. In *2010 Annual International Conference of the IEEE Engineering in Medicine and Biology* 4809–4812 (2010).
93. Sreelatha, T., Subramanyam, M. V. & Prasad, M. G. Early detection of skin cancer using melanoma segmentation technique. *J. Med. Syst.* **43**, 1–7 (2019).
94. Khoja, L., Lorigan, P., Dive, C., Keilholz, U. & Fusi, A. Circulating tumour cells as tumour biomarkers in melanoma: Detection methods and clinical relevance. *Ann. Oncol.* **26**, 33–39 (2015).
95. Zakria, D., Brownstone, N., Fritz, K., Salavastru, C. & Rigel, D. Utilizing data from electrical impedance spectroscopy significantly improves the decision to biopsy pigmented skin lesions beyond clinical evaluation and dermoscopy. *SKIN J. Cutan. Med.* **8**, 1515–1520 (2024).
96. Ferris, L. K. & Harris, R. J. New diagnostic aids for melanoma. *Dermatol. Clin.* **30**, 535–545 (2012).
97. Wachsmann, W. et al. Noninvasive genomic detection of melanoma. *Br. J. Dermatol.* **164**, 797–806 (2011).
98. Marsavela, G., Aya-Bonilla, C. A., Warkiani, M. E., Gray, E. S. & Ziman, M. Melanoma circulating tumor cells: Benefits and challenges required for clinical application. *Cancer Lett.* **424**, 1–8 (2018).
99. Aya-Bonilla, C. A. et al. Detection and prognostic role of heterogeneous populations of melanoma circulating tumour cells. **122**, 1059–1067 (2020).
100. Kurma, K. & Alix-Panabières, C. Mechanobiology and survival strategies of circulating tumor cells: A process towards the invasive and metastatic phenotype. *Front. Cell Dev. Biol.* **11**, 1188499 (2023).
101. Regmi, S., Fu, A. & Luo, K. Q. High shear stresses under exercise condition destroy circulating tumor cells in a microfluidic system. *Sci. Rep.* **7**, 39975 (2017).
102. Perea Paizal, J., Au, S. H. & Bakal, C. Squeezing through the microcirculation: Survival adaptations of circulating tumour cells to seed metastasis. *Br. J. Cancer* **124**, 58–65 (2021).
103. Lee, H. J. et al. Fluid shear stress activates YAP1 to promote cancer cell motility. *Nat. Commun.* **8**, 14122 (2017).
104. Tigli, O., Bivona, L., Berg, P. & Zaghoul, M. E. Fabrication and characterization of a surface-acoustic-wave biosensor in CMOS technology for cancer biomarker detection. *IEEE Trans. Biomed. Circuits Syst.* **4**, 62–73 (2010).
105. Tigli, O. & Zaghoul, M. E. A novel SAW device in CMOS: design, modeling, and fabrication. *IEEE Sens. J.* **7**, 219–227 (2007).
106. Sharma, P. & Sreenivas, K. Highly sensitive ultraviolet detector based on ZnO/LiNbO₃ hybrid surface acoustic wave filter. *Appl. Phys. Lett.* **83**, 3617–3619 (2003).
107. Ho, C. K., Lindgren, E. R., Rawlinson, K. S., McGrath, L. K. & Wright, J. L. Development of a surface acoustic wave sensor for in-situ monitoring of volatile organic compounds. *Sensors* **3**, 236–247 (2003).
108. Clorennec, D. & Royer, D. Analysis of surface acoustic wave propagation on a cylinder using laser ultrasonics. *Appl. Phys. Lett.* **82**, 4608–4610 (2003).
109. Yeo, L. Y. & Friend, J. R. Ultrafast microfluidics using surface acoustic waves. *Biomicrofluidics* **3**, 12002 (2009).
110. Vellekoop, M. J. Acoustic wave sensors and their technology. *Ultrasonics* **36**, 7–14 (1998).
111. Wang, X., Ellis, J. S., Kan, C. D., Li, R. K. & Thompson, M. Surface immobilisation and properties of smooth muscle cells monitored by on-line acoustic wave detector. *Analyst* **133**, 85–92 (2008).
112. Chin, W. W. et al. In-vivo optical detection of cancer using chlorin e6-polyvinylpyrrolidone induced fluorescence imaging and spectroscopy. *BMC Med. Imaging* **9**, 1–13 (2009).
113. Pierce, M. C. & Richards-Kortum, R. Low-cost, portable optical imaging systems for cancer diagnosis. In *2010 Annual International Conference of the IEEE Engineering in Medicine and Biology* 1093–1096 (2010).
114. Pais, A., Banerjee, A., Klotzkin, D. & Papautsky, I. High-sensitivity, disposable lab-on-a-chip with thin-film organic electronics for fluorescence detection. *Lab Chip* **8**, 794–800 (2008).
115. Gronewold, T. M. Surface acoustic wave sensors in the bioanalytical field: Recent trends and challenges. *Anal. Chim. Acta* **603**, 119–128 (2007).
116. Shin, K. S. et al. Amplification of fluorescence with packed beads to enhance the sensitivity of miniaturized detection in microfluidic chip. *Biosens. Bioelectron.* **22**, 2261–2267 (2007).
117. Defelice, L. J. *Electrical Properties of Cells: Patch Clamp for Biologists* 49–121 (Springer Science & Business Media, 2013).
118. Stuart, G. J. & Palmer, L. M. Imaging membrane potential in dendrites and axons of single neurons. *Pflügers Arch.* **453**, 403–410 (2006).
119. Ashrafuzzaman, M. & Tuszyński, J. A. *Membrane Biophysics* (Springer Science & Business Media, 2012).
120. Buck, R. P. Kinetics of bulk and interfacial ionic motion: microscopic bases and limits for the Nernst–Planck equation applied to membrane systems. *J. Membr. Sci.* **17**, 1–62 (1984).
121. Neumcke, B. & Läuger, P. Nonlinear electrical effects in lipid bilayer membranes: II. Integration of the generalized Nernst–Planck equations. *Biophys. J.* **9**, 1160–1170 (1969).

122. Gillespie, D., Nonner, W. & Eisenberg, R. S. Coupling Poisson–Nernst–Planck and density functional theory to calculate ion flux. *J. Phys. Condens. Matter* **14**, 12129–12145 (2002).
123. Sokalski, T. & Lewenstam, A. Application of Nernst–Planck and Poisson equations for interpretation of liquid-junction and membrane potentials in real-time and space domains. *Electrochim. Commun.* **3**, 107–112 (2001).
124. Brumleve, T. R. & Buck, R. P. Numerical solution of the Nernst–Planck and Poisson equation system with applications to membrane electrochemistry and solid state physics. *J. Electroanal. Chem. Interfacial Electrochem.* **90**, 1–31 (1978).
125. Rinzel, J. Discussion: Electrical excitability of cells, theory and experiment: Review of the Hodgkin–Huxley foundation and an update. *Bull. Math. Biol.* **52**, 5–23 (1990).
126. Kistler, W. M., Gerstner, W. & Hemmen, J. L. V. Reduction of the Hodgkin–Huxley equations to a single-variable threshold model. *Neural Comput.* **9**, 1015–1045 (1997).
127. Izhikevich, E. M. Simple model of spiking neurons. *IEEE Trans. Neural Netw.* **14**, 1569–1572 (2003).
128. Roth, B. J. & Basser, P. J. A model of the stimulation of a nerve fiber by electromagnetic induction. *IEEE Trans. Biomed. Eng.* **37**, 588–597 (1990).
129. Fain, G. J. Action potentials: The Hodgkin–Huxley experiments. In *Molecular and Cellular Physiology of Neurons* (ed. Edel, C. N.) 255–307 (Harvard University Press, 1999).
130. Bennett, M. R., Farnell, L. & Gibson, W. G. Cable analysis of a motor-nerve terminal branch in a volume conductor. *Bull. Math. Biol.* **61**, 1–17 (1999).
131. Scholz, F. Electroanalytical methods: Guide to Experiments and applications. In *Electroanalytical Methods* Vol. 1 (ed. Scholz, F.) (Springer, 2010).
132. Baker, S. G. & Kramer, B. S. Systems biology and cancer: promises and perils. *Prog. Biophys. Mol. Biol.* **106**, 410–413 (2011).
133. Clayton, R. H. Computational models of normal and abnormal action potential propagation in cardiac tissue: Linking experimental and clinical cardiology. *Physiol. Measurement* **22**, R15–R34 (2001).
134. Sheean, G. L., Murray, N. M., Rothwell, J. C., Miller, D. H. & Thompson, A. J. An open-labelled clinical and electrophysiological study of 3, 4 diaminopyridine in the treatment of fatigue in multiple sclerosis. *Brain J. Neurol.* **121**, 967–975 (1998).
135. Cone, C. D. Jr. Unified theory on the basic mechanism of normal mitotic control and oncogenesis. *J. Theor. Biol.* **30**, 151–181 (1971).
136. Binggeli, R. & Weinstein, R. C. Membrane potentials and sodium channels: hypotheses for growth regulation and cancer formation based on changes in sodium channels and gap junctions. *J. Theor. Biol.* **123**, 377–401 (1986).
137. Hoyle, N. P. et al. Circadian actin dynamics drive rhythmic fibroblast mobilization during wound healing. *Sci. Transl. Med.* **9**, eaal2774 (2017).
138. Eming, S. A., Martin, P. & Tomic-Canic, M. Wound repair and regeneration: Mechanisms, signaling, and translation. *Sci. Transl. Med.* **6**, 265sr6 (2014).
139. Krause, M. & Gautreau, A. Steering cell migration: Lamellipodium dynamics and the regulation of directional persistence. *Nat. Rev. Mol. Cell Biol.* **15**, 577–590 (2014).
140. Dan, B. B. & Fritz, H. (eds) *Obituary: David Elliot Rogers*, Vol. 273 1469–1469 (JAMA, 1995).
141. Richards, D. M. & Endres, R. G. The mechanism of phagocytosis: two stages of engulfment. *Biophys. J.* **107**, 1542–1553 (2014).
142. Zhu, Z. X. et al. Hedgehog signaling contributes to basic fibroblast growth fact. *355*, 83–94 (2017).
143. Butler, M. G. et al. Subset of individuals with autism spectrum disorders and extreme macrocephaly associated with germline PTEN tumour suppressor gene mutations. *J. Med. Genetics* **42**, 318–321 (2005).
144. Clements, C. M., McNally, R. S., Conti, B. J., Mak, T. W. & Ting, J. P. Y. DJ-1, a cancer-and Parkinson's disease-associated protein, stabilizes the antioxidant transcriptional master regulator Nrf2. *Proc. Natl. Acad. Sci.* **103**, 15091–15096 (2006).
145. Alqabandi, J. Design syntheses and analyses of a lab on a chip (LoC) module based on biological cell requirements in nature. *Int. J. Des. Nat. Ecodynamics* **10**, 70–86 (2015).
146. Marcus, J. S. *Single Mammalian Cell Gene Expression Analysis Using Microfluidics*. Doctoral dissertation (California Institute of Technology, 2006).
147. Rodriguez, J. et al. Effects of several flavonoids on the growth of B16F10 and SK-MEL-1 melanoma cell lines: Relationship between structure and activity. *Melanoma Res.* **12**, 99–107 (2002).
148. Sheridan, C., Brumatti, G. & Martin, S. J. Oncogenic B-RafV600E inhibits apoptosis and promotes ERK-dependent inactivation of Bad and Bim. *J. Biol. Chem.* **283**, 22128–22135 (2008).
149. Giard, D. J. et al. In vitro cultivation of human tumors: Establishment of cell lines derived from a series of solid tumors. *J. Natl. Cancer Inst.* **51**, 1417–1423 (1973).
150. Dejana, E. et al. Interleukin 1 promotes tumor cell adhesion to cultured human endothelial cells. *J. Clin. Investig.* **82**, 1466–1470 (1988).
151. Wieland, B. M. et al. Is there a human homologue to the murine proteolysis-inducing factor?. *Clin. Cancer Res.* **13**, 4984–4992 (2007).
152. Shepard, H. M. & Lewis, G. D. Resistance of tumor cells to tumor necrosis factor. *J. Clin. Immunol.* **8**, 333–341 (1988).
153. Blesch, A. et al. Cloning of a novel malignant melanoma-derived growth-regulatory protein, MIA. *Cancer Res.* **54**, 5695–5701 (1994).
154. MacDougall, J. R., Bani, M. R., Lin, Y., Muschel, R. J. & Kerbel, R. S. Proteolytic switching': Opposite patterns of regulation of gelatinase B and its inhibitor TIMP-1 during human melanoma progression and consequences of gelatinase B overexpression. *Br. J. Cancer* **80**, 504–512 (1999).
155. Terp, M. G., Lund, R. R., Jensen, O. N., Leth-Larsen, R. & Ditzel, H. J. Identification of markers associated with highly aggressive metastatic phenotypes using quantitative comparative proteomics. *Cancer Genom. Proteom.* **9**, 265–273 (2012).
156. Ross, D. T. et al. Systematic variation in gene expression patterns in human cancer cell lines. *Nat. Genet.* **24**, 227–235 (2000).
157. Ellison, G. et al. Further evidence to support the melanocytic origin of MDA-MB-435. *Mol. Pathol.* **55**, 294–299 (2002).
158. Garraway, L. A. et al. Integrative genomic analyses identify MITF as a lineage survival oncogene amplified in malignant melanoma. *Nature* **436**, 117–122 (2005).
159. Wu, C.-C. et al. Pristimerin induces caspase-dependent apoptosis in MDA-MB-231 cells via direct effects on mitochondria. *Mol. Cancer Ther.* **4**, 1277–1285 (2005).
160. Roger, S., Besson, P. & Le Guennec, J. Y. Involvement of a novel fast inward sodium current in the invasion capacity of a breast cancer cell line. *Biochim. Biophys. Acta (BBA) Biomembr.* **1616**, 107–111 (2003).
161. Kirschmann, D. A., Seftor, E. A., Nieva, D. R., Mariano, E. A. & Hendrix, M. J. Differentially expressed genes associated with the metastatic phenotype in breast cancer. *Breast Cancer Res. Treat.* **55**, 127–136 (1999).
162. Hung, P. J. et al. A novel high aspect ratio microfluidic design to provide a stable and uniform microenvironment for cell growth in a high throughput mammalian cell culture array. *Lab Chip* **5**, 44–48 (2005).
163. Kim, C. et al. 3-Dimensional cell culture for on-chip differentiation of stem cells in embryoid body. *Lab Chip* **11**, 874–882 (2011).
164. Leclerc, E., Sakai, Y. & Fujii, T. Cell culture in 3-dimensional microfluidic structure of PDMS (polydimethylsiloxane). *Biomed. Microdevices* **5**, 109–114 (2003).
165. Jalali, S. et al. Integrin-mediated mechanotransduction requires its dynamic interaction with specific extracellular matrix (ECM) ligands. *Proc. Natl. Acad. Sci.* **98**, 1042–1046 (2001).
166. Yin, T. I. et al. Development of a microfluidic device with microcantilever sensor array for probing single cancer cells mechanics. In *2011 16th International Solid-State Sensors, Actuators and Microsystems Conference*, Vol. 11 1216–1219 (2011).

167. Usami, S., Chen, H. H., Zhao, Y., Chien, S. & Skalak, R. Design and construction of a linear shear stress flow chamber. *Ann. Biomed. Eng.* **21**, 77–83 (1993).
168. Chaudhuri, O., Parekh, S. H., Lam, W. A. & Fletcher, D. A. Combined atomic force microscopy and side-view optical imaging for mechanical studies of cells. *Nat. Methods* **6**, 383–388 (2009).
169. Lim, C. T., Zhou, E. H. & Quck, S. T. Mechanical models for living cells—A review. *J. Biomech.* **39**, 195–216 (2006).
170. Sun, Y. & Nelson, B. J. MEMS for cellular force measurements and molecular detection. *Int. J. Inf. Acquis.* **1**, 23–32 (2004).
171. Lee, G. Y. & Lim, C. T. Biomechanics approaches to studying human diseases. *Trends Biotechnol.* **25**, 111–118 (2007).
172. Berry, C. C., Campbell, G., Spadiccino, A., Robertson, M. & Curtis, A. S. The influence of microscale topography on fibroblast attachment and motility. *Biomaterials* **25**, 5781–5788 (2004).
173. Ghibaudo, M., Di Meglio, J. M., Hersen, P. & Ladoux, B. Mechanics of cell spreading within 3D-micropatterned environments. *Lab Chip* **11**, 805–812 (2011).
174. Mierke, C. T., Bretz, N. & Altevogt, P. Contractile forces contribute to increased glycosylphosphatidylinositol-anchored receptor CD24-facilitated cancer cell invasion. *J. Biol. Chem.* **286**, 34858–34871 (2001).
175. Yang, S. M. & Yin, T. I. Design and analysis of piezoresistive microcantilever for surface stress measurement in biochemical sensor. *Sens. Actuators B Chem.* **120**, 736–744 (2007).
176. Goericke, F. T. & King, W. P. Modeling piezoresistive microcantilever sensor response to surface stress for biochemical sensors. *IEEE Sens. J.* **8**, 1404–1410 (2008).
177. Raorane, D. A., Lim, M. D., Chen, F. F., Craik, C. S. & Majumdar, A. Quantitative and label-free technique for measuring protease activity and inhibition using a microfluidic cantilever array. *Nano Lett.* **8**, 2968–2974 (2008).
178. Ricciardi, C. et al. Integration of microfluidic and cantilever technology for biosensing application in liquid environment. *Biosens. Bioelectron.* **26**, 1565–1570 (2010).
179. Lin, G., Pister, K. S. & Roos, K. P. Surface micromachined polysilicon heart cell force transducer. *J. Microelectromechanical Syst.* **9**, 9–17 (2000).
180. Alhazza, K. A., Masoud, Z. N. & Alajmi, M. Nonlinear free vibration control of beams using acceleration delayed-feedback control. *Smart Mater. Struct.* **17**, 015002 (2008).
181. Wang, B. T. & Rogers, C. A. Modeling of finite-length spatially-distributed induced strain actuators for laminate beams and plates. *J. Intell. Mater. Syst. Struct.* **2**, 38–58 (1991).
182. Alhazza, K. A., Nayfeh, A. H. & Daqaq, M. F. On utilizing delayed feedback for active-multimode vibration control of cantilever beams. *J. Sound Vib.* **319**, 735–752 (2009).
183. Daqaq, M. F., Alhazza, K. A. & Arafat, H. N. Non-linear vibrations of cantilever beams with feedback delays. *Int. J. Non Linear Mech.* **43**, 962–978 (2008).
184. Gotszalk, T., Grabcic, P. & Rangelow, I. W. Piezoresistive sensors for scanning probe microscopy. *Ultramicroscopy* **82**, 39–48 (2000).
185. Ivanov, T. *Piezoresistive Cantilevers with an Integrated Bimorph Actuator*. Doctoral dissertation (University of Kassel, 2004).
186. Woszczyyna, M. et al. Quantitative force and mass measurements using the cantilever with integrated actuator and deflection detector. *Microelectron. Eng.* **86**, 1043–1045 (2009).
187. Filenko, D. et al. Experimental setup for characterization of self-actuated microcantilevers with piezoresistive readout for chemical recognition of volatile substances. *Rev. Sci. Instrum.* **79**, 094101 (2008).
188. Michels, T., Gulyev, E., Klukowski, M. & Rangelow, I. W. Micromachined self-actuated piezoresistive cantilever for high speed SPM. *Microelectron. Eng.* **97**, 265–268 (2012).
189. Ivanov, T., Gotszalk, T., Grabcic, P., Tomerov, E. & Rangelow, I. W. Thermally driven micromechanical beam with piezoresistive deflection readout. *Microelectron. Eng.* **67**, 550–556 (2003).
190. Han, M. et al. A novel fabrication process for out-of-plane microneedle sheets of biocompatible polymer. *J. Micromech. Microeng.* **17**, 1184–1191 (2007).
191. Wang, G. J., Chen, C. L., Hsu, S. H. & Chiang, Y. L. Bio-MEMS fabricated artificial capillaries for tissue engineering. *Microsyst. Technol.* **12**, 120–127 (2005).
192. Wang, Y. G. & Lin, W. H. Pull-in voltage analysis for an electrostatically actuated extensional microbeam with large deflection. *ZAMM J. Appl. Math. Mech. Z. Angew. Math. Mech. Appl. Math. Mech.* **90**, 211–218 (2010).
193. El-Ali, J., Sorger, P. K. & Jensen, K. F. Cells on chips. *Nature* **442**, 403–411 (2006).
194. Yin, Z. et al. A screen for morphological complexity identifies regulators of switch-like transitions between discrete cell shapes. *Nat. Cell Biol.* **15**, 860–871 (2013).
195. Nayfeh, A. H., Ouakad, H. M., Najar, F., Choura, S. & Abdel-Rahman, E. M. Nonlinear dynamics of a resonant gas sensor. *Nonlinear Dyn.* **59**, 607–618 (2010).
196. Sanz-Moreno, V. et al. ROCK and JAK1 signaling cooperate to control actomyosin contractility in tumor cells and stroma. *Cancer cell* **20**, 229–245 (2011).
197. Gui, Y. et al. Cytokine-generated contractility drives tumor cell migration. *Cancer Discov.* **1**, 284. <https://doi.org/10.1158/2159-8290.CD-RW083111-18> (2011).
198. Teng, T. S., Lin, B., Manser, E., Ng, D. C. H. & Cao, X. Stat3 promotes directional cell migration by regulating Rac1 activity via its activator β PIX. *J. Cell Sci.* **122**, 4150–4159 (2009).
199. Iqbal, M. et al. Efficacy of CD19 directed therapies in patients with relapsed or refractory large b-cell lymphoma relapsing after CD19 directed chimeric antigen receptor T-cell therapy. *Bone Marrow Transplant.* **59**, 211–216 (2023).
200. Chester, J. et al. Correction: Corrigendum: Tumor antigen—Specific induction of transcriptionally targeted retroviral vectors from chimeric immune receptor—modified T cells. *Nat. Biotechnol.* **24**, 1293–1293 (2006).
201. An, F. et al. Influence of patient characteristics on chimeric antigen receptor T cell therapy in B-cell acute lymphoblastic leukemia. *Nat. Commun.* **11**, 5928 (2020).
202. Li, L. et al. Treatment response, survival, safety, and predictive factors to chimeric antigen receptor T cell therapy in Chinese relapsed or refractory B cell acute lymphoblast leukemia patients. *Cell Death Dis.* **11**, 207 (2020).
203. Dagher, O. K. & Posey, A. D. Jr. Forks in the road for CAR T and CAR NK cell cancer therapies. *Nat. Immunol.* **24**, 1994–2007 (2023).
204. Bhatia, V. et al. Targeting advanced prostate cancer with STEAP1 chimeric antigen receptor T cell and tumor-localized IL-12 immunotherapy. *Nat. Commun.* **14**, 2041 (2023).
205. Zhang, C., Hu, Y., Xiao, W. & Tian, Z. Chimeric antigen receptor-and natural killer cell receptor-engineered innate killer cells in cancer immunotherapy. *Cell. Mol. Immunol.* **18**, 2083–2100 (2021).

Acknowledgements

We would like to express our highest appreciation to Emeritus Prof. Nigel Gooderham from the Department of Metabolism, Digestion and Reproduction at Imperial College London, Faculty of Medicine, for his helpful comments, kind review, and feedback. His received comments significantly strengthened the overall manuscript.

Author contributions

J.A.A contributed mainly to this work under the other authors' review, guidance, and supervision. R.D., U.M.A., and R.O.E assisted J.A.A in culturing cells and conducting in vitro experiments, whereas K.Y.T. reviewed the analytical and empirical findings as well as supervised the micro/nanofabrication and construction of the mechatronic platforms. J.A.A. wrote the manuscript, edited multiple versions of the manuscript, and contributed to revisions.

Declarations

Competing interests

J.A.A. is a holder of two provisional patent applications (US 63/641,641 and US 63/641,724) for the process carried out by the constructed two miniaturized biomechatronic platforms in detecting and/or characterizing cellular mechanobiology and electrophysiology signaling. The remaining authors declare that the research was conducted in the absence of any commercial or financial relationships that could be construed as a potential conflict of interest.

Additional information

Correspondence and requests for materials should be addressed to J.A.A. or R.O.E.

Reprints and permissions information is available at www.nature.com/reprints.

Publisher's note Springer Nature remains neutral with regard to jurisdictional claims in published maps and institutional affiliations.

Open Access This article is licensed under a Creative Commons Attribution-NonCommercial-NoDerivatives 4.0 International License, which permits any non-commercial use, sharing, distribution and reproduction in any medium or format, as long as you give appropriate credit to the original author(s) and the source, provide a link to the Creative Commons licence, and indicate if you modified the licensed material. You do not have permission under this licence to share adapted material derived from this article or parts of it. The images or other third party material in this article are included in the article's Creative Commons licence, unless indicated otherwise in a credit line to the material. If material is not included in the article's Creative Commons licence and your intended use is not permitted by statutory regulation or exceeds the permitted use, you will need to obtain permission directly from the copyright holder. To view a copy of this licence, visit <http://creativecommons.org/licenses/by-nc-nd/4.0/>.

© The Author(s) 2024